



University
of Glasgow

Hu, Zhixiong (2012) *Development of an integrated microspectrometer using arrayed waveguide grating (AWG)*.

PhD thesis

<http://theses.gla.ac.uk/3439/>

Copyright and moral rights for this thesis are retained by the author

A copy can be downloaded for personal non-commercial research or study, without prior permission or charge

This thesis cannot be reproduced or quoted extensively from without first obtaining permission in writing from the Author

The content must not be changed in any way or sold commercially in any format or medium without the formal permission of the Author

When referring to this work, full bibliographic details including the author, title, awarding institution and date of the thesis must be given



UNIVERSITY
of
GLASGOW

Development of an integrated microspectrometer using arrayed waveguide grating (AWG)

Zhixiong Hu

A thesis submitted to School of Engineering
College of Science and Engineering
University of Glasgow

In fulfilment of the requirements for the degree of Doctor of Philosophy
(Ph.D.)

©Zhixiong Hu, April 2012

All Right Reserved

To my beloved girl friend (Shupeng Song) who always asks me:
'when will you finish your PhD?'

献给我的女朋友宋淑鹏

Abstract

With non-invasive properties and high sensitivities, portable optical biosensors are extremely desirable for point-of-care (POC) applications. Lab-on-a-chip technology such as microfluidics has been treated as an ideal approach to integrate complex sample processing and analysis units with optical detection elements. Spectroscopic sensing (such as fluorescence, Raman and absorption spectroscopy) remains the most highly developed, widely applied, optical technique. However, conventional spectroscopic sensing systems still rely on bulky and expensive dispersive components such as spectrophotometers in a well established laboratory. The work in this thesis is to develop an integrated dispersive component in combination with a microfluidic chip, providing a portable and inexpensive platform for on-chip spectroscopic sensing.

In this study, an arrayed waveguide grating (AWG) design developed for telecommunication is re-engineered and utilized to realise a compact, dispersive optical component operating in the visible spectral region. The AWG devices operating in the visible region ($\lambda_c=680$ nm) are designed and fabricated with flame hydrolysis deposited (FHD) silica waveguide material. The micro-spectrometer in this proof of concept study has a small (1 cm x 1 cm) footprint and 8 output channels centred on different wavelengths. A series of fabrication issues and challenges are investigated and discussed for the specific AWG device. Subsequently, a sample cuvette is formed by using lithographic technique and dry etching process. Following this, a PDMS chip with microfluidic channels is bonded with the AWG device, leading to an integrated AWG-microfluidic platform. To the best of the author's knowledge, this is the first work to integrate a visible AWG device and a microfluidic chip towards spectroscopic sensing.

The monolithic integrated AWG microspectrometer–microfluidic platform is demonstrated for fluorescence spectroscopic analysis. Signals from the output channels detected on a camera chip can be used to re-create the complete fluorescence spectrum of an analyte. By making fluorescence measurements of (i) mixed quantum dot solutions, (ii) an organic fluorophore (Cy5) and (iii) the propidium iodide (PI)-DNA assay, the results obtained illustrate the unique advantages of the AWG platform for simultaneous, quantitative multiplex detection and its capability to detect small spectroscopic shifts. Although the current system is designed for fluorescence spectroscopic analysis, in principle, it can be implemented for other types of analysis, such as Raman spectroscopy. Fabricated using established semiconductor industry methods, this miniturised platform holds great potential to create a handheld, low cost biosensor with versatile detection capability.

Also, the AWG device design is modified with focusing properties that enable localised spectroscopic measurements. Micro-beads based, multiplexed fluorescence detection is performed with the AWG + CCD system and the results have demonstrated capabilities of using the adapted AWG device for localised, multiplexed fluorescence detections, opening up potential applications in the field of cell sorting and single cell analysis. Furthermore, the AWG-microfluidic device is investigated for absorption spectroscopy measurement. As a test system, the pH dependence of the absorption spectra of bromophenol blue is measured to illustrate how an AWG device could be used as a colorimetric pH sensor. Overall, it is believed that the AWG technology holds great potential to realise a compact, integrated spectroscopic biosensor for point-of-care applications.

Publications

Journals

Zhixiong Hu, Andrew Glidle, Charles Ironside, Marc Sorel, Michael Strain, Jonathan M Cooper and Huabing Yin, “Integrated microspectrometer for fluorescence based analysis in a microfluidic format”, ‘Lab on a Chip’, Accepted, 2012. DOI: 10.1039/C2LC40169J

Conference

Zhixiong Hu, Andrew Glidle, Charles Ironside, Marc Sorel, Michael Strain, Jonathan M Cooper and Huabing Yin, “A compact optical sensor for biological assay using spectral multiplexing”, The 6th International Conference on Bioinformatics and Biomedical Engineering (iCBBE 2012), Accepted. May 17-20, 2012, Shanghai, China.

Zhixiong Hu, Andrew Glidle, Charles Ironside, Marc Sorel, Michael Strain and Huabing Yin, “On-chip micro-spectrometer for fluorescence biosensing” , CLEO/Europe-EQEC, Munich, Paper ISIV2.2, 2011.

Zhixiong Hu, Andrew Glidle, Charles Ironside, Marc Sorel, Michael Strain, Jonathan M Cooper and Huabing Yin, “Spectrometer-on-chip for fluorescence bio-sensing” 6th IEEE EMBS UK & Republic of Ireland Postgraduate Conference on Biomedical Engineering and Medical Physic. Glasgow, 14th-16th August 2011.

Zhixiong Hu, Andrew Glidle, Charles Ironside, Marc Sorel, Michael Strain, Jonathan M Cooper and Huabing Yin, “Changing the World – a conference for early career researchers” University of Glasgow, 7th November 2011.

Zhixiong Hu, Andrew Glidle, Charles Ironside, Marc Sorel, Michael Strain, Jonathan M Cooper and Huabing Yin, “Integrated optical spectroscopic sensor – Arrayed Waveguide Grating (AWGs) for Biophotonics” 1st Academic Conference for Chinese government funded researchers, Tianjin University, Tianjin, P. R. China, 27th December 2009.

Acknowledgements

I would like to thank my supervisors, Dr. Huabing Yin and Prof. Charles N. Ironside for the guidance and support over the course of this work. Without Huabing, I would not have the opportunity to carry out this research in University of Glasgow. Thanks for your continuous inspiration on my research as well as considerate assistance to my personal life.

Many thanks to Dr. Andrew Glidle, who is a walking encyclopedia. Without Andrew, this PhD would not have been possible.

Thanks also go to Dr. Marc Sorel, Dr. Michael Strain and Prof. Jonathan M Cooper for their helpful discussion and advice on this project.

Thanks to Mike Jubber and Henk Bulthuis from Gemfire Europe Ltd (Scotland) with the assistance of AWG work.

I would like to acknowledge the financial support from Chinese Scholarship Council and the University of Glasgow for my scholarship and access to the JWNC fabrication facilities.

Special thanks go to my girl friend (Shupeng Song) for her support, encouragement and patience throughout my PhD study. Last but not least I would like to give my thanks to my family and friends for their support although they didn't really understand what I was doing.

Author's declaration

The work presented in this thesis was conducted by the author and has not previously been submitted for a degree or diploma at this university or any other institution.

Abstract	3
Publications	5
Acknowledgements	6
Author’s declaration	7
List of Figures	12
List of Tables.....	20
Chapter 1-Introduction.....	21
1.1 Portable optical biosensor.....	21
1.2 Approaches of integrated optical components.....	22
1.3 Lab-on-chip with microfluidic technology	24
1.4 Aims of the work.....	24
1.5 Fluorescence measurement.....	25
1.5.1 Basic physics of fluorescence	25
1.5.2 Cy5 fluorophore	28
1.5.3 Propidium iodide.....	29
1.5.4 Inorganic fluorophore – Quantum dots	30
1.5.5 Instrumentation for fluorescence measurements.....	32
1.5.6 Fluorescence spectroscopy measurement	34
1.6 Flow cytometry	35
1.6.1 Microfabricated fluorescence activated flow cytometer	36
1.6.2 Microfluidics for micro-fabricated cell sorter.....	37
1.6.3 Integrated optical detection system.....	37
1.6.4 Important trends of flow cytometry	38
1.7 Absorption spectroscopic measurement.....	39
1.7.1 On-chip approaches for absorption spectroscopy	40
1.7.2 Absorbance measurement with an on-chip spectrometer.....	41
1.7 Thesis outline	43

Chapter 2-AWG theory, design and simulation	45
Abstract	45
2.1 Introduction	45
2.2 Material consideration for visible AWG	46
2.3 AWG configuration and working principle	50
2.3.1 AWG structure	50
2.3.2 AWG equation	52
2.3.3 Dispersion	53
2.3.4 Free Spectral Range (FSR).....	54
2.4 AWG design strategy and simulation	55
2.5 Summary	59
Chapter 3-Fabrication of AWG device and microfluidics.....	60
Abstract	60
3.1 Overview of the process flow	61
3.2 Fabrication issues and challenges	63
3.3 Optimisation of the AWG device fabrication	63
3.3.1 Feature patterning via photolithography	63
3.3.2 Optimisation of electron beam lithography process.....	66
3.3.3 Dry etching process.....	71
3.4 Overview of AWG structure definition	78
3.5 Formation of cladding layer	79
3.6 Patterning of sample cuvette	80
3.7 Integration with PDMS microfluidic chip.....	82
3.7.1 Fabrication of a silicon mould.....	83
3.7.2 Preparation of a PDMS chip	84
3.7.3 Bonding of PDMS chip and AWG device	85
3.8 Summary	87

Chapter 4-Optical characterisation and fluorescence measurement	88
Abstract	88
4.1 Validation of the optical performance of the AWG device in the visible region	89
4.1.1 Characterization using a white light source and a spectrophotometer	89
4.1.2 Characterisation of AWG-Microfluidic device with a monochromatic light source and a CCD camera	91
4.2 Evaluation of fluorescence measurements	96
4.2.1 Multiplexing fluorescence measurements with quantum dots	96
4.2.2 Cy5 spectroscopic fluorescence measurements	100
4.2.3 Assay based on spectroscopic analysis	105
4.3 Summary	109
Chapter 5-Localised spectroscopic measurements.....	110
Abstract	110
5.1 Introduction	110
5.2 Results and Discussion	111
5.2.1 Adapted AWG devices for localised detection	111
5.2.2 Localised fluorescence detection	116
5.3 Experimental section	122
5.3.1 Immobilisation of quantum dots in the sample cuvette	122
5.3.2 Micro-beads immobilisation and bioconjugation reactions	125
5.5 Summary	130
Chapter 6-Absorption spectroscopic measurements.....	132
Abstract	132
6.1 Introduction	132
6.2 Results and discussion.....	133
6.2.1 Absorbance measurements with conventional spectrophotometer	133
6.2.2 Absorbance measurements with AWG-microfluidic device and CCD.....	133
6.3. Experimental section	137

6.3.1 AWG-microfluidic device and experimental setup.....	137
6.4 Summary	139
Chapter 7-Conclusions and future work.....	140
7.1 Conclusions	140
7.1.1 Design and fabrication of AWG-microfluidic device.....	141
7.1.2 Optical characterisation of AWG system.....	143
7.1.3 Use of AWG-microfluidic device for simultaneous, multiplex fluorescence measurements.....	143
7.1.4 Quantitative fluorescence spectroscopic measurements with an AWG device	144
7.1.5 Shaping the beam profile in the AWG device cuvette for voxel-like measurements.....	145
7.1.6 Absorbance measurements with an AWG device.....	146
7.2 Future work	146
7.2.1 AWG device loss characterization and reduction.....	146
7.2.2 Increasing light collecting efficiency of AWG input waveguide.....	148
7.2.3 Polymer AWG device	149
7.2.4 Applications	149
References	151

List of Figures

Figure 1.1 General structure of an integrated optical biosensor	22
Figure 1.2 Modified Jablonski (electronic transitions) diagram. Adapted from Jablonski. A (1935) [118]. The diagram illustrates the electronic levels of common organic fluorescent molecules and the process of absorption, fluorescence and phosphorescence.	26
Figure 1.3 Normalized theoretical absorption and emission spectra for Cy2 TM , Cy3 TM and Cy5 TM dyes (Amersham Biosciences). Adapted from M.Lopez. (2003). <i>Proteomics</i> , 3, 1109-1116 [120].....	27
Figure 1.4 Chemical structure of generic Cyanine dye and Cy5.	29
Figure 1.5 Spectrum of Cy5 emission and 632.8 nm excitation line.	29
Figure 1.6 Chemical structure of propidium iodide (PI).....	30
Figure 1.7 Absorption and emission spectra of different Quantum dots. Adapted from Quantum dots brochure of Invitrogen Inc.	31
Figure 1.8 Schematic of the overall structure of a functionalized quantum dot. Adapted from Quantum dots brochure of Invitrogen Inc.	32
Figure 1.9 Schematic setup of multiplexing fluorescence measurement. Adapted from S. Hohng et al. (2004) <i>Biophysical</i> , 87, 1328-1337 [123]. The confocal setup was made on an inverted microscope (Olympus, IX50). A solid-state laser excites a sample at 532 nm through a $\times 100$ oil-immersion objective. Emission from the multiple dyes is collected by the same objective and separated by dichroic mirrors and filtered out by bandpass filters. D1, D2, D3: dichroic filters; F1, F2, F3: bandpass filters; M: mirror; L: lens; P: pinhole; PBS: polarizing beam splitter; $\lambda/2$: half-wave plate; and APD: avalanche photo diode.	33
Figure 1.10 A typical spectrometer and its inside optical configuration. Adapted from Brochure of TRIAX Series spectrometer form Jobin Yvon Inc. Left: TRIAX series spectrometer equipped with array detectors. Right: optical diagram of TRIAX series spectrometer.	34
Figure 1.11 Schematic diagram of a typical fluorescence-activated flow cytometer. It consists of four units: (a) flow cell; (b) detection system; (c) electronic module and (d) sorting mechanism. The flow cell utilises the surrounding sheath fluid to obtain hydrodynamic focusing of the sample solution, thereby the cells or particles could pass the interrogation point one by one. A laser excitation beam is focused on the interrogation point and produces scattered and fluorescent light from the illuminated cell or particle. With the aid of collecting lens, beam splitters and various optical filters, both the scattering light and fluorescence signals are measured with proper photodetectors such as photo multiplier tube (PMT). For each cell or particle detected, output pulses from the scattering and fluorescence detectors are amplified and processed with a specified electronic module which will then send a feedback signal to the sorting mechanism. After receiving the feedback signal, the sorting mechanism will perform corresponding operation to ensure different types of cells or particles travel forward to specific collectors through deflecting their trajectories.....	36

Figure 1.12 Schematic of double beam absorption measurement. The combination of white light source and monochromator provides a tunable monochromatic light which are divided into two beams by a splitter. The two separate light beams pass through the sample cuvette and reference cuvette respectively and the transmitted light signals are received by the detectors.	40
Figure 1.13 Schematic of the AWG-microfluidic platform with CCD detection.....	43
Figure 2.1 The spectrum of water absorption. Adapted from [175].	46
Figure 2.2 AWG configuration	50
Figure 2.3 Equivalent optical system of AWG	51
Figure 2.4 Rowland circle configuration of AWG.....	51
Figure 2.5 General design procedure of AWG	55
Figure 2.6 Schematic illustration of the cross section profile of the waveguide. The values of refractive indexes given correspond to those at a wavelength of 632.8 nm. BPSG: Boron-Phosphor-Silica-Glass.....	56
Figure 2.7 Single mode condition of waveguide at $\lambda_c=680$ nm.	57
Figure 2.8 Minimum bending radius ($Min(R)$) of waveguide	57
Figure 2.9 AWG design layout	58
Figure 2.10 Simulation result of AWG device.....	59
Figure 3.1 Schematic of the process steps for integrated AWG sensor chip. Either photolithography or electron beam lithography (EBL) can be used to define AWG structures. Process with Photolithography is more simple and accessible while E-beam lithography provides design with a high flexibility.	62
Figure 3.2 Schematics and SEM images of joint area of 1 st slab region and arrayed waveguides. (a) without gap between arrayed waveguides; (b) 2 μm gap between arrayed waveguides.....	64
Figure 3.3 Microscopic images after lift-off (a) without developer soaking; (b) with 60 seconds developer soaking before UV exposure.	65
Figure 3.4 AWG structure with SU-8 e-beam lithography after resist development and the applied dose was 2.5 $\mu\text{C}/\text{cm}^2$	67
Figure 3.5 AWG structure with SU-8 e-beam lithography after resist development and the applied doses were (a) 1.3 $\mu\text{C}/\text{cm}^2$ and (b) 3.3 $\mu\text{C}/\text{cm}^2$. Wavy and discontinuous arrayed waveguides could be found in (a) because of lower dose used. Inversely, the right image (b) reveals higher dose effect which causes SU-8 resist between arrayed waveguides to be polymerised in the area inside the red dashed ellipse.	68
Figure 3.6 Proximity effect of AWG structure with SU-8 e-beam lithography after resist development. Inside red dashed area, the gaps between arrayed waveguides are not clear but filled with polymerised SU-8 residue.	69

Figure 3.7 Microscopic dark field image of AWG structure with UVIII e-beam lithography after resist development and the applied dose is $55 \mu\text{C}/\text{cm}^2$	70
Figure 3.8 Microscopic dark field image of AWG structure with UVIII e-beam lithography after resist development. (a) under-exposed, dose= $34.5 \mu\text{C}/\text{cm}^2$; (b) dose= $49 \mu\text{C}/\text{cm}^2$; (c) dose= $62 \mu\text{C}/\text{cm}^2$. No observable difference was found of AWG structures when doses of range 49 to $62 \mu\text{C}/\text{cm}^2$ were applied.	70
Figure 3.9 Typical configuration of a RIE system. (picture adapted from Oxford Instruments website)	71
Figure 3.10 SEM image of FHD silica etching profile with CHF_3/Ar RIE using UVIII mask.	74
Figure 3.11 Illustration of the sidewall profile of CHF_3/Ar plasma etching using UVIII mask.	74
Figure 3.12 SEM image of the junction of AWG slab region and arrayed waveguides after dry etching with CHF_3/Ar RIE using UVIII mask.	74
Figure 3.13 Waveguide profile of CHF_3/Ar plasma etching using NiCr mask.	76
Figure 3.14 Waveguide profile of CHF_3/O_2 plasma etching using NiCr mask.	77
Figure 3.15 Waveguide sidewall of CHF_3/O_2 plasma etching using NiCr mask.....	77
Figure 3.16 Comparison of etching processes with CHF_3/Ar and CHF_3/O_2 . (a) Dirty surface after etch using CHF_3/Ar ; (b) The addition of O_2 to the standard CHF_3 etch process improved the surface roughness significantly.	77
Figure 3.17 Illustration of different regions from a fabricated AWG device.	78
Figure 3.18 SEM profile of waveguide cross section.	79
Figure 3.19 Schematic of the AWG device with a sample cuvette.....	80
Figure 3.20 Illustration of sample cuvette fabrication. (a), after S1818 resist development. The right end of the horizontal waveguide is connected to the AWG device while the left part is used to introduce a broad band light source for AWG device characterization. The perpendicular waveguide is designed to deliver the excitation light for fluorescence measurement and the sample cuvette of $20\mu\text{m} \times 20 \mu\text{m}$ is located in the central junctions. (b), after the first 30 minute dry etch with bi-layer mask of S1818 and NiCr. (c), after whole process of dry etching. The sample surface became dirty possibly due to non-uniform consumption of resist layer and poor chamber condition caused by large covering area of NiCr metal mask. (d), after mask material removal.....	82
Figure 3.21 Illustration of fabrication steps to make the silicon mould. (a), photoresist was spun on the surface of silicon wafer; (b), photolithography step to expose the resist and finish the development; (c), Reactive ion etching (RIE) of silicon; (d), remove the resist residue and obtain the silicon mould.....	84
Figure 3.22 Schematic of PDMS replica moulding. (a), silicon mould was cleaned in an ultrasonic bath and the surface was treated with fluorinated silanes. (b), a liquid PDMS prepolymer (a 10:1 mixture of prepolymer and its curing agent) was poured onto the	

silicon mould. (c), the PDMS was cured in an oven at 70 °C. Then the PDMS was peeled off to obtain a free standing microfluidic chip.....	85
Figure 3.23 3D illustration of AWG device bonded with PDMS microfluidic chip	86
Figure 3.24 Real AWG device after bonding with PDMS chip. Inlet and outlet of the microfluidic channel were connected to polymer tubings through tip-flattened syringe needles.....	87
Figure 4.1 Experiment diagram to characterise the AWG device with a white light source and a spectrometer.....	89
Figure 4.2 Experimental setup for characterising the AWG device with a white light source and a spectrophotometer. (a) Photo of the experiment platform. The white light source and spectrophotometer are fibre connected and not shown in this picture. (b) A close view of the fibre micropositioners and sample stage. (c) A close view of the AWG device and dispositioned fibres.	90
Figure 4.3 Microscopic images of (a) input coupling and (b) output coupling with lensed fibres. (c) A picture of an 8 output channel AWG chip compared to one British penny.....	90
Figure 4.4 Experimental transmission spectrum of the AWG device. Intensities scaled so that the maximum transmission equals 100 arbitrary units. Different colours indicate signals from each output channel.....	91
Figure 4.5 Experiment diagram to characterise the AWG device with a monochromatic light source and a CCD camera.....	92
Figure 4.6 Spectrum of monochromator output with centre wavelength at 680nm.	92
Figure 4.7 Intensity profile of monochromator output from 650 nm to 720 nm.	93
Figure 4.8 Illustration of CCD-based characterisation method for the AWG-microfluidic system. A monochromator was used to provide mechanically tuned light of narrow-band wavelength. A 45° mirror and a ×4 objective lens were used to reflect AWG output signals onto a vertically mounted CCD camera.	93
Figure 4.9 Characterisation results of AWG-microfluidic system using the CCD-based method. On the left side: CCD images of output signals from 8 output channels corresponding to narrow-band light of different centre wavelengths. On the right side: plots of the intensity profile along a horizontal line that connects the light spots of the output channels in the CCD images.	95
Figure 4.10 Experiment diagram for quantum dot measurements. Two different quantum dots (QD655 and QD705) were excited by a single light source and their emission light were collected and processed by the AWG device. Emissions from the two different quantum dots separate and exit from their corresponding output channels.	96
Figure 4.11 Illustration of quantum dot experiment setup. The experiment was performed by mounting the AWG device on a modified upright microscope stage. There was a fabricated sample cuvette (100 µm wide, 100 µm long and 2 µm deep) across the AWG input waveguide. The quantum dot solution filled in the sample cuvette was excited by a ×50 focused blue light source which was realised by allowing the mercury lamp light to pass through an appropriate filter set. Light from the AWG output channels were coupled	

into a conventional spectrometer (TRIA320) for characterisation. Inset image indicated by the dashed arrow: illustration of the sample cuvette.....	97
Figure 4.12 Multiplexed measurement of quantum dots using the AWG device. Spectra of quantum dots in red and blue were obtained from the representative AWG output channel (1 and 6) while those in black were the corresponding references obtained via off chip measurement. Three solutions were used: (a) QD655 only, (b) QD705 only and (c) a mixture of QD655 and QD705.....	98
Figure 4.13 Illustration of Cy5 fluorescence measurement with the AWG-microfluidic platform and a conventional spectrometer. Cy5 solution was flowing in the microfluidic channel and the fluorophore passing cuvette area was excited by 632.8 nm laser light coming from the 45° intercepted waveguide (E-WG). The optical signals from each AWG output channel were fibre coupled into a conventional spectrometer (TRIA320) for wavelength and intensity investigation.	100
Figure 4.14 Cy5 fluorescence measurement result with the AWG-microfluidic platform and a conventional spectrometer. The comparison between different wavelength peaks (colour lines) from the 8 output channels (indicated by the digit numbers) and the reference Cy5 emission spectrum (the black line) is shown.....	101
Figure 4.15 (a) Spectroscopic signals from AWG output Channel 3 (670 nm) with different concentrations of Cy5 solution. (b) the relationship between Ch3 peak intensity and Cy5 solution concentration. Four different concentrations (1 μM, 10 μM, 20 μM and 85 μM) were tested comparing with deionized (DI) water.	101
Figure 4.16 Illustration of Cy5 fluorescence measurement with the AWG-microfluidic platform and a CCD detector. (a) Schematic illustration of integration of AWG device with microfluidics and CCD. A 45° mirror and a ×4 objective lens were used to reflect AWG output signals onto a vertically mounted CCD detector. (b) A close up view of the monolithic integrated AWG-PDMS microfluidic chip, where the sampling cuvette is located in the middle of the microfluidic channel. The red flare starting in the cuvette area and going diagonally towards the top left of the microfluidic channel shows the path of light emanating from the excitation waveguide. C-WG: white light characterisation waveguide. E-WG: excitation waveguide. I-AWG: AWG input waveguide.	102
Figure 4.17 Pictures of real experiment setup for Cy5 fluorescence measurement. (a) Picture of the complete experiment setup. (b) A close view of the modified microscope stage. (c) A close view of the AWG-microfluidic platform. The whole experiment setup was using an upright Nikon microscope (Microphot SA) by modifying its stage. The AWG-microfluidic platform was mounted on a sample holder which was positioned in the centre of the modified microscope stage. External light sources, including broad band white light and narrow band excitation laser, were fibre coupled into the AWG device. Two V-groove fibre holders were attached respectively to two different 3-axis micropositioners (Line Tool Company) which were fixed on the modified microscope stage. A CCD camera (Andor 885 iXon) was mounted vertically onto the microscope. A 45° mirror (made by depositing 75 nm NiCr on silicon wafer) and a ×4 objective lens were used to reflect AWG output signals onto the CCD detector. Sample solutions were delivered into the microfluidic channel of the PDMS chip by using PTFE tubings, a plastic syringe and a pumping unit. Various flow rates could be obtained by adjust the pump control.	103

Figure 4.18 Result of Cy5 fluorescence measurement with the AWG-microfluidic platform and a CCD detector. (i) CCD image of the output from Cy5 emission, channels from left to right are channel 1 to channel 8. (ii) top-down bright field image of the output waveguides. (iii) The intensities of the CCD images from the output in comparison to a Cy5 emission spectrum. A 633 nm notch filter and a 650 nm long pass filter were used to remove all the excitation light from the signal.104

Figure 4.19 Graph of output channel 3 signal intensity with error bars and regression line for measuring different concentrations of Cy5 solution with AWG-microfluidic platform and CCD detector. Output channel 3 was selected as the example channel since it corresponded to the maximum wavelength (670 nm) of Cy5 emission spectrum. 3 or 4 measurements were performed for each concentration (0.1 μ M, 0.2 μ M, 0.5 μ M, 1.0 μ M, 2.0 μ M, 5.0 μ M and 10 μ M). The error bars were made by using maximum, average and minimum values for each group of the measurement results and the deviations were within the range of $\pm 6\%$105

Figure 4.20 Fluorescence spectra of PI solutions with and without DNA (obtained off chip).106

Figure 4.21 Normalized transmission spectral response of the AWG device for two different diffraction orders. (a) $m = 8$; (b) $m = 7$107

Figure 4.22 PI-DNA fluorescence measurement result with AWG-microfluidic-CCD system. (a) The intensity profile of the 8 outputs taken from the CCD images from for the PI solutions with and without DNA. (b) fluorescence intensity versus DNA concentrations plots comparing off chip spectrometer measurement (data taken from Figure 4.20 at 570 nm) and on chip measurement with a CCD detector (data taken from channel 1). The images were acquired for 5 minutes. Error bars indicate +/- one standard deviation.108

Figure 5.1 Schematic diagrams of optical detection system with conventional free-standing and integrated optics. (a) conventional optical detection system with the aid of lens. A laser excitation beam is focused by a lens onto the interrogation point and another lens is utilised to collect signals such as fluorescence onto the detector. A filter set needs to be employed if fluorescence detection is used. (b) optical detection system from the AWG design consisting of integrated waveguides with (i) flat end, or (ii) lens curvature. C-WG: white light characterisation waveguide; E-WG: excitation waveguide; I-AWG: input waveguide of the AWG device. The lenses at the end of integrated waveguides could enable a focusing excitation and localised collection while flat-end integrated waveguide would experience divergent light paths.112

Figure 5.2 Schematic of microfluidic incorporation onto the AWG device with focusing waveguides. The sampling cuvette is located in the middle of the microfluidic channel. And the end faces are designed with lens curvature for the three integrated waveguides which are intercepted by the cuvette. C-WG: white light characterisation waveguide, E-WG: excitation waveguide.113

Figure 5.3 Fluorescence microscopic images of the optical detection system with focusing integrated waveguides. A fluorescent dye solution (Cy5) was delivered into the microfluidic channel and a laser excitation light (632.8 nm laser) was introduced into different integrated waveguides: (a) C_WG; (b) E_WG; (c) AWG input waveguide. By filtering the excitation light, the fluorescence microscopic images of the cuvette area were acquired respectively and (d) is their composite image by using different colors for each light path. Differing from inherent divergent property of flat-end integrated waveguides,

the lens-aided scheme offered focusing light paths which are consistent with the theoretical design. The arrows in figure (a) to (c) indicate the direction of laser excitation. In figure (d), the intersection area of the three light paths is highlighted with a pink dashed circle.114

Figure 5.4 Fluorescence images of the optical detection system with flat-end waveguides. Compared to Figure 5.3, flat end faces instead of lens curvature were designed for the three intercepted waveguides. Likewise, three fluorescence images were acquired under the same experimental condition. Using the method, the composite image of the initial three is shown in (d). Without lensing, the inherent divergent light paths were shown clearly. The arrows in figure (a) to (c) indicate the direction of laser excitation. In figure (d), the intersection area of the three light paths is highlighted with a pink dashed circle.115

Figure 5.5 Fluorescence image of the localised quantum dot pattern. The sampling cuvette area is illuminated by above excitation light which is from the mercury lamp of the fluorescence microscope. The fluorescence image reveals the localised quantum dot pattern. The unexpected bright image outside the cuvette comes from non-specific bonded quantum dots and there is an accumulation of quantum dots at the end of the three integrated waveguides.116

Figure 5.6 Experimental setup for blue-violet laser excitation. A blue-violet laser diode (DL-4146-101S from Sanyo, see top left inset image) is mounted onto a printed circuit board (PCB) which is connected with a driven circuit (bottom right inset image). The laser light is coupled by a $\times 20$ objective lens into a bare single mode optical fibre.117

Figure 5.7 Fluorescence image of the localised quantum dot pattern with side blue-violet laser excitation. The blue-violet laser excitation light is introduced into the cuvette through the planar excitation waveguide (E-WG). The bright spot at the end of E-WG reveals an accumulation of quantum dots there. The red dashed circle indicates the localised quantum dots pattern while the outside grey dashed circle represents the cuvette border. Due to lower topography of the cuvette, only the nearby edge of inside quantum dots pattern is strongly illuminated by the excitation light.118

Figure 5.8 Experimental schematic and fluorescence image of the adsorbed micro beads. (a) Experiment setup for fluorescence measurement of the adsorbed micro beads. The laser excitation was introduced through the planar excitation waveguide (E-WG). The fluorescence signal was collected by the above objective lens ($\times 50$) and detected by a CCD camera after an emission filter. (b) the acquired fluorescence image of the adsorbed micro beads. The borders of the sampling cuvette and the three integrated waveguides were marked with grey dashed lines.119

Figure 5.9 Experimental schematic of micro beads-based multiplexing fluorescence assay. A laser light beam was fibre coupled into the planar excitation waveguide (E-WG). A 45° mirror and a $\times 4$ objective lens were used to reflect AWG output signals onto a vertically mounted CCD camera or a photon detector. Prior to measurement with the CCD camera, fluorescence signal from the sampling cuvette was collected by an above $\times 50$ objective lens and then fibre connected to a conventional spectrometer (inside the blue dashed area). The acquired fluorescence spectra were used to verify the CCD detection results.120

Figure 5.10 Fluorescence spectra and corresponding AWG+CCD detection results of the spectral multiplexing assay. (a) Flash red fluorescence micro beads. (b) After adding biotin conjugated quantum dots (605 nm). (c) After adding streptavidin conjugated quantum dots (655 nm). On the left are the pre-acquired fluorescence spectra while the right provides the

CCD images of specific output channels and their histograms of light intensity maximum.	121
Figure 5.11 Process scheme of localising quantum dots in the centre of the sampling cuvette. (a) The surface of FHD silica based AWG device is cleaned with organic solvent and piranha solution. (b) The front surface is coated with aminosilane. (c) Photolithography is used to define the localised pattern outside which the surface is blocked by the undeveloped photoresist. (d) The exposed amine-reactive layer is linked with NHS-Biotin. (e) The undeveloped photoresist is removed by washing with DMSO. (f) Immobilisation of the streptavidin conjugated quantum dots through specific avidin-biotin binding.	123
Figure 5.12 Process flow diagram of micro beads-based fluorescence assay. (a) The surface of FHD silica based AWG device is cleaned with organic solvent and piranha solution. (b) Deposition of gold layer. (c) Pattern definition with photolithography. (d) Gold wet etch and photoresist removal. (e) Aminothiols binding on the gold surface. (f) NHS-Biotin linking. (g) Adsorption of streptavidin conjugated micro beads. (h) Immobilisation of biotin conjugated quantum dots (605 nm). (i) Immobilisation of streptavidin conjugated quantum dots (655 nm).	126
Figure 5.13 Gold disk pattern ($D=40\mu\text{m}$) in the centre of the sampling cuvette	128
Figure 5.14 Sample test results of bead adsorption after different lengths of time. (a) 30 minutes. (b) 60 minutes.....	130
Figure 6.1 Bromophenol blue solutions with different pH. The color changes from yellow to blue when the pH increases.....	132
Figure 6.2 Absorption spectra of various bromophenol blue at different pH.	133
Figure 6.3 Schematic of absorption measurement with AWG-microfluidic device and CCD camera. A PDMS microfluidic chip was bonded with the AWG device and the square sampling cuvette ($50\mu\text{m}$ wide and $2\mu\text{m}$ deep) is located in the middle of the microfluidic channel. A broad band light source was fibre coupled into characterization waveguide (C- WG) and travelled through the sample solution in the cuvette. The transmitted light is then collected by the AWG device for wavelength separation. A 45° mirror and a $\times 4$ objective lens were used to reflect AWG output signals onto a vertically mounted CCD camera. Due to the relatively narrow band periodical property of AWG transmission spectrum in this prototype device, a combination of a long-pass filter (550LP) and a short-pass filter (650SP) was used to restrain the wavelength range to be investigated.....	134
Figure 6.4 Absorption spectra of various bromophenol blue at different pH taken with (a) AWG-microfluidic device and (b) Hitachi U-2000 spectrophotometer. Error bars indicate \pm one standard deviation.....	135
Figure 6.5 AWG-microfluidic device and the sampling cuvette. (a) AWG device bonded with a PDMS microfluidic chip. The microfluidic channel is indicated with yellow dashed lines. (b) microscope image of the sampling cuvette in the middle of the microfluidic channel.	137
Figure 6.6 Experiment setup for the absorption measurement with AWG-microfluidic device and CCD camera. (a) Full view of the experiment setup. (b) A closer view of sample position stage and the mirror positioner. (c) The home made mirror.....	138

Figure 7.1 Microscope image showing the microcracks of HSQ after the hard baking148

Figure 7.2 3T3 cell immobilisation in the centre of the sample cuvette using different AWG devices: (a) conventional design; (b) with focusing waveguides. C-WG: waveguide for characterization; E-WG: excitation waveguide; I-AWG: input of the AWG device...150

List of Tables

Table 2.1 Properties of different waveguide materials [189, 190].....46

Table 2.2 Experimental properties of visible AWG devices.....48

Table 2.3 Variables used in AWG structure52

1. Chapter 1 Introduction

1.1 Portable optical biosensor

A biosensor is an analytical device for the detection of an analyte that combines a biological component with a physicochemical detector. There are many potential applications of biosensors of various types, including chemical analysis, bio-analysis, and clinical diagnostics and so on. The best known, representative and successful commercial biosensor is the blood glucose sensor which was first introduced by Clark and Lyons in 1962 [1].

Apart from electrochemical detections that work well for certain applications, there are a variety of transducer methods available to realize biosensors of different types and better suited for various applications. Among these methods, optical detection is preferred where it is necessary for the sensing probe to avoid physical contact, have high sensitivity, isolation from electromagnetic interference, and a high-throughput capability. The most common optical sensing methods are based on absorption spectrometry, emission detection (luminescence, fluorescence and Raman signals), or refractive index related measurement (surface Plasmon resonance, interferometer, grating, and photonic crystal etc) [2-5].

However, conventional optical detection systems are usually bulky and expensive because they need various light sources, lenses, mirrors, filters, detectors and spectroscopic components. Thus, although they can be well established in laboratory environment, these large systems are not suitable for point-of-care (POC) applications which include personalized healthcare, environmental monitoring, forensic analysis, global health, and so on [6-12]. In developments aimed at miniaturisation of systems, although fibre optics allow convenient light delivery and collection [13, 14], planar waveguide technology is often preferable due to the compatibility of its planar geometry with a range of advanced microfabrication techniques. Additionally, integrated planar configurations are much more robust in the context of optical alignment compared to optical fibre-based sensors when employed outside the laboratory environment [10, 15-20].

1.2 Approaches of integrated optical components

An integrated optical biosensor normally consists of four components as shown in Figure 1.1.



Figure 1.1 General structure of an integrated optical biosensor

The light source provides basic illumination or excitation of sample target while a detector is used to collect optical signal from the analyte and convert it to electronic format. The optical transducer is employed to identify specific chemical or biological interaction which is correlated with changes of light properties. It is worth noting that most optical signals need to be processed before reaching final photon detectors. However, unlike comprehensive and complicated signal processing in opto-telecommunication field, most on-chip optical biosensors require additional fundamental components such as mirrors [21-23], lenses [24-29], filters [30-32], gratings [33-36] and other diffractive elements [37-41].

Thanks to advances of micro-engineering and optoelectronics, efficient and inexpensive laser diodes (LD) and light emitting diodes (LED) are available to be integrated into a portable optical biosensor [42-44]. Miniaturization of optical components such as CCD and CMOS detectors has also made the ‘on-chip approach’ very promising [45-49]. Furthermore, planar integrated waveguides have not only been used to deliver or collect light but also employed as a range of transduction components including interferometers [50-52], surface plasmon resonance (SPR) elements [53-55], gratings [56-58], microring resonators [59-61] and photonic crystals [62-65].

To establish an entire on-chip optical platform, 2D and 3D microlenses were designed and integrated not only for focusing and collimating light but also for illumination and imaging purposes [24-27, 29]. Micromirrors were also incorporated into planar systems where the light path needs to be altered or lengthened [21-23]. No matter whether emission detection is employed or a refractive index related measurement is involved, most optical methods of transduction still require a filtering or spectroscopic component to process or detect optical

signal in frequency (wavelength) domain. Developing such a component using arrayed waveguide grating (AWG) technology is the principle subject of this thesis.

Different approaches have been used to integrate optical filters with a compact sensing platform [30]. Thin-film interference filters with brilliant tailorable spectral profiles were combined with portable biosensors to detect fluorescence [46, 66, 67]. However, the applications employing these interference based filters suffer from requiring complicated fabrication of multi-layer deposition and a remarkable degradation of performance when the fluorescence light is incident at oblique angles. For absorption methods, absorptive filters prepared by various methods have also been tested on-chip by several groups [68-71]. Although absorptive filters are cheap and easy to fabricate in an on-chip system, the magnitude of the sample's optical density is restricted by optical path length which is normally very small. Finally, some other integrated technologies such as spectrally selective detectors [72-75] and polarization filtering [49, 76] have been implemented to address specific sensing requirements. Considering each technology has its own advantages and limitations, combination of different methods have also been tried to offset the disadvantages of single filter [31, 32, 77].

Miniaturized spectroscopic components play an important role in portable detection systems that employ spectroscopy. With advances of optical microelectromechanical system (MEMS), integrated spectroscopic systems have been realized with grating [78, 79] or interferometer [80-85] based components. However, the trend is ultimately towards fully integrated optical microsystem such as single-chip spectrometer. Various approaches have been demonstrated to implement an on-chip microspectrometer [86-91]. Recently, on-chip spectrometers based on micro-ring resonator [92, 93], superprism-based photonic crystal (PC) [94-97], digital planar hologram (DPH) [98-101] and porous silicon [102] were proposed. However, these devices are still in their infancy and need to be further refined beyond the proof-of-concept. A planar waveguide grating is commonly employed to disperse the light into different wavelengths. A first attempt presented by Goldman et al. in 1990 used two buried gratings for both light coupling and dispersion [103]. Optical fibre technology can be integrated through fibre coupling methods with planar waveguides made of different materials on a microfabricated substrate to yield robust integrated systems with better performance as a consequence of efficient transfer of optical signals (light) to/from

off-chip light sources and detectors [104, 105]. An alternative approach is to use an arrayed waveguide grating (AWG) [106, 107] which is similar in functionality to a transmission grating. The use of an AWG circumvents restrictions on reflecting efficiency associated with planar grating facets and the resolution of an AWG system can be easily enhanced by increasing number of arrayed waveguides and output channels. Furthermore, the size of AWG device can be made very compact while keeping a high performance and the means of light input and output is compatible with fibre technology.

1.3 Lab-on-chip with microfluidic technology

Microfluidics which was developed with micro-manufacturing techniques has become a 'hot spot' research area during last 20 years [108-110]. Researches into miniaturization are primarily driven by the need to cut down costs by reducing the consumption of expensive reagents and by increasing throughput and automation. By means of microfluidics, it not only makes analysis faster and less expensive but also creates some completely new types of measurements that are impossible with large-scale instruments. In recent years, both active and passive microfluidic components such as pumps, mixers, and valves have allowed the development from simple platforms to systems of lab-on-a-chip [111-113]. There are a wide range of materials, including silicon, glass, and different polymers, which can be used to make microfluidic chips. Combination of microfluidic channels with planar optical waveguides provides highly compact and integrated devices which could target at point-of-care biosensing [10, 15-17, 19].

1.4 Aims of the work

The purpose of this work was to develop a spectroscopic element suitable for an integrated optical biosensor used in point-of-care diagnoses. Specifically, the main research was focused on using arrayed waveguide grating (AWG) as the core component. An arrayed waveguide grating (AWG) is a type of planar waveguide technology used for wavelength de/multiplexing in opto-telecommunication field. Due to an AWG using light dispersion as the means of signal processing, the research carried out here investigated the feasibility of using an AWG in a portable optical biosensor.

For this investigation, the optical biosensor system was targeted at working in UV and visible light range i.e. that which is most commonly used for optical detections, especially in aqueous environments. Hence, the AWG technology needed to be transferred and adjusted from the base designs established for conventional infrared (IR) AWG devices.

Monolithic integration of sample manipulation and photonic devices is a highly potential and advantageous solution to a point-of-care optical biosensor. This work brings together strengths from clean room fabrication facilities and emerging microfluidic technology. Combination with compact light source and CCD sensor were also demonstrated. Based on this platform, a series of measurements including absorption, fluorescence emission and multi-color detection were performed and evaluated.

1.5 Fluorescence measurement

1.5.1 Basic physics of fluorescence

Since the majority of bio-sensing targeted analytes are present in minute quantities and often with a complex matrix, high selectivity, sensitivity and accuracy are of paramount importance for a detection method. In this context, fluorescence based approaches are amongst the most highly developed, widely applied optical techniques due to their selectivity, excellent sensitivity and versatility [114-116]. With advances of modern instruments, the fluorescence techniques have been proven to offer nanometer-scale resolution and sensitivity down to single-molecule level [117].

Fluorescence is emission of light by a molecule which absorbs light photons of higher energy (i.e. shorter wavelength), known as the excitation light source. The process responsible for the fluorescence is illustrated by the modified Jablonski diagram (electronic-state diagram) shown in Figure 1.2. In a molecular system, there are different electronic states for the electrons. The state with lowest energy is called ground state (G) while states with higher energy are excited states (e.g. S1, S2, S3). In the process of fluorescence, a molecule needs firstly to be excited into a higher energy state (e.g. S2) by

absorbing an excitation light. Since the excited states are very unstable, the electrons will relax back into lower levels which are non-radiative processes including heat dissipation and other ways of energy loss. The fluorescence occurs when electrons finally transit into the energetically favourable ground state. Clearly, the fluorescence light emitted has photons with a lower energy than those in the excitation light (i.e. the emission wavelength is longer than that from excitation). The energy difference (or wavelength shift) between the higher excited state S2 and the lower excited state S1 (i.e. absorption and emission light) is termed as ‘Stokes shift’. It is worth noting that fluorescence is not the only one possible relaxation mechanism during the electronic transition processes. There are possible non-radiative transitions of the electrons into triplet states (T), which will then give rise to a phenomenon called phosphorescence.

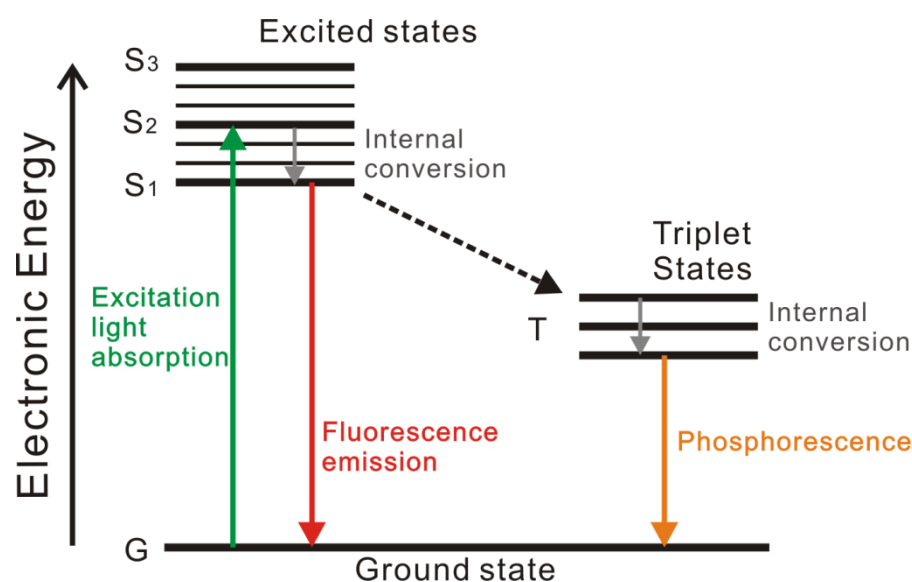


Figure 1.2 Modified Jablonski (electronic transitions) diagram. Adapted from Jablonski, A (1935) [118]. The diagram illustrates the electronic levels of common organic fluorescent molecules and the process of absorption, fluorescence and phosphorescence.

Organic fluorophore molecules are well established as fluorescent labels for in vitro and in vivo bio-sensing. There are a wide range of functionalized dyes which are commercially available for various specific applications. Fundamentally, fluorescent molecules have characteristic absorption and emission spectra. The Stokes shifts are normally below 50 nm and the emission spectra are asymmetric, often tailing to long-wavelength side [119]. It is a remarkable fact that the absorption and emission spectra are unique to each fluorescent molecule, which can be easily seen in Figure 1.3.

Intensity detection is one of the most commonly used methodologies for fluorescence based measurements. A typical instrumental set up comprises an excitation light source, an optical filter and a photodetector. Often, laser induced fluorescence (LIF) detection is preferred because of its more intense illumination for enhanced fluorescence signal and extremely narrow bandwidth of the excitation source (the laser) which simplifies the use of optical filters. However, in practice, the limited number of laser lines available in commercial sources and their expense restrict the fluorophores that are used in LIF based studies.

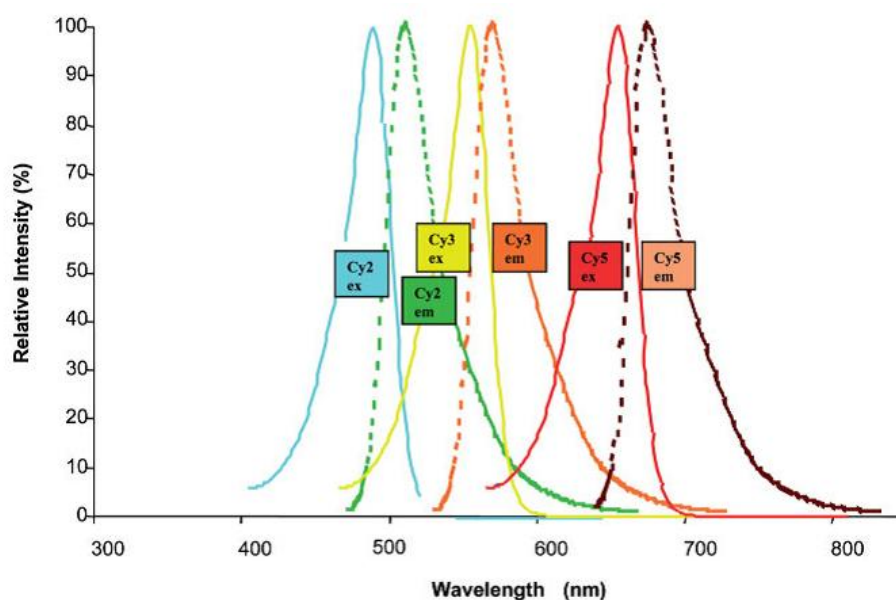


Figure 1.3 Normalized theoretical absorption and emission spectra for Cy2™, Cy3™ and Cy5™ dyes (Amersham Biosciences). Adapted from M.Lopez. (2003). *Proteomics*, **3**, 1109-1116 [120].

Fluorescence resonance energy transfer (FRET) is a mechanism describing energy transfer between two fluorescent molecules which are located very close (1 to 10 nm) [121, 122]. In a FRET process, the emission spectrum of one fluorophore (donor) is partially overlapped with the absorption spectrum of another fluorophore (acceptor). When the donor dye molecule is excited, its emission light will be absorbed by the acceptor dye molecule which will emit fluorescence light. The energy transfer efficiency is influenced by distance between the two molecules and investigation of the ratiometric FRET can be used to sense conformational changes or other molecular processes involving a change in

distance. Importantly, configuration with more than two-color single-molecule FRET has been performed as a powerful biophysical tool [123, 124].

For parallel analysis of different analytes, high-throughput detections with multiple fluorescent dyes could be employed [120]. However, multiplexing applications with organic dyes are quite limited, which is attributed to their discrete absorption spectra, small Stokes shifts and broad emission spectra. Although the problem can be overcome by multi-wavelength excitation using different lasers [125], this approach needed to rely on relatively complicated instrumentation.

In the sub-sections below, the specific properties and opportunities of the three fluorophores (Cy5, Propidium iodide and Quantum dots) used in this thesis are reviewed.

1.5.2 Cy5 fluorophore

Cyanine dyes have found widespread use as fluorescent labels for bio-molecules since early 1990s [126, 127]. This class of fluorophores have high extinction coefficients, moderate quantum yields and photostability. Cyanine dyes have the general structure shown in Figure 1.4, with two nitrogen-containing heteroaromatic rings linked by a polymethine bridge comprising an odd number of carbons. Cyanine dyes are ideal candidate probes for multi-color fluorescence detections since they can be synthesized with a wide range of absorption and emission spectra that span the whole visible region through controlling the length of the polymethine bridge and the identity of the heteroaromatic rings. Cyanine dyes are usually synthesized with reactive groups on either one or both of the nitrogen side chains so that it can be chemically linked to either nucleic acids or protein molecules. By using cyanine dyes as fluorescence probes, a series of biological applications are readily accessible, including proteomics [128, 129], DNA/RNA labelling [130-132] and live cell imaging [133, 134].

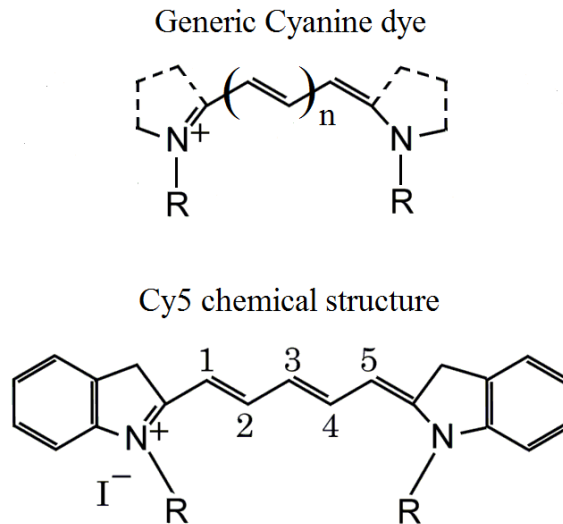


Figure 1.4 Chemical structure of generic Cyanine dye and Cy5.

Cy5 is a water-soluble fluorescent dye of the cyanine dye family and was firstly proposed by Ernst et al in 1989 [135, 136]. As shown in Figure 4.16, the chemical structure of Cy5 is symmetrical with 5 methine groups in the bridge. Generally, Cy5 conjugates are excited maximally at 650 nm and fluoresce maximally at 670 nm. For laser induced Cy5 fluorescence detection, a narrow bandwidth excitation light source such as 632.8 nm He-Ne laser can be used and the consequent emission spectrum is given in Figure 1.5.

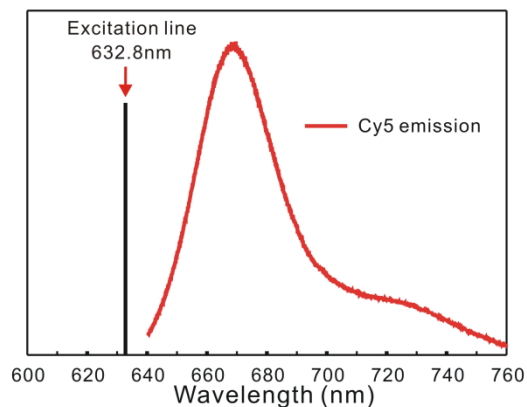


Figure 1.5 Spectrum of Cy5 emission and 632.8 nm excitation line.

1.5.3 Propidium iodide

Propidium iodide (PI) is a fluorescence dye and intercalating agent, commonly used for quantitative analysis of DNA [137-139]. As shown in Figure 1.6, propidium iodide is a

type of classical intercalator in which fused-ring aromatic molecules with positive charges are attached to a side chain or another ring system. The planar ring system stacks well with base pairs in the intercalation complex. There is little or no sequence preference for the binding of propidium iodide and DNA and it is best described by the nearest neighbour exclusion principle which means when DNA is saturated with intercalators, every second potential intercalation site on the helix remains empty. It should be noted that propidium iodide also binds to RNA and the intercalation does not interfere with hydrogen bonding of the base pairs.

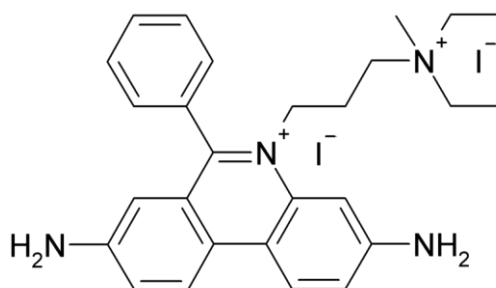


Figure 1.6 Chemical structure of propidium iodide (PI).

Once a PI molecule binds to DNA by intercalating the bases, its fluorescence intensity is enhanced significantly and its peak emission exhibits a blue-shift. The variation in equilibrium concentrations of bound and unbound PI with increasing DNA concentration is complex. However, when using a PI solution of a given concentration, the amount of bound PI increases smoothly as the concentration of DNA increases until either all of the PI is bound, or the DNA is maximally loaded.

1.5.4 Inorganic fluorophore – Quantum dots

Quantum dots are semiconductor nanocrystals which have unique electronic and optical properties differing from either discrete atoms or bulky solids owing to the effect of quantum confinement [140]. These quantum dots are often made from II/VI and III/V semiconductors in which CdSe and CdTe are the most prominent materials. Compared with conventional organic fluorophores, quantum dots are the ideal candidates for spectral multiplexing fluorescence measurements due to a series of attractive optical properties

[119]. As shown in Figure 1.7, the excitation spectra (i.e. absorption spectra) are very broad and the molar extinction coefficients gradually increase towards shorter wavelengths, making it possible for uncompromised simultaneous excitation with a single light source. Furthermore, the emission spectra of quantum dots are symmetric and can be very narrow, thereby reducing spectral crosstalk in complex labelling assays where multiple types of quantum dots are present. Additionally, the relatively high fluorescence quantum yield and photostability of quantum dots are advantages when really sensitive or long term monitoring is required. Above all, these nanometer-sized quantum dots are of great interest to bio-sensing not only because of their dimensional similarities with biological macromolecules (e.g. nucleic acids and proteins) but also due to their unique size-tunable optical properties [141].

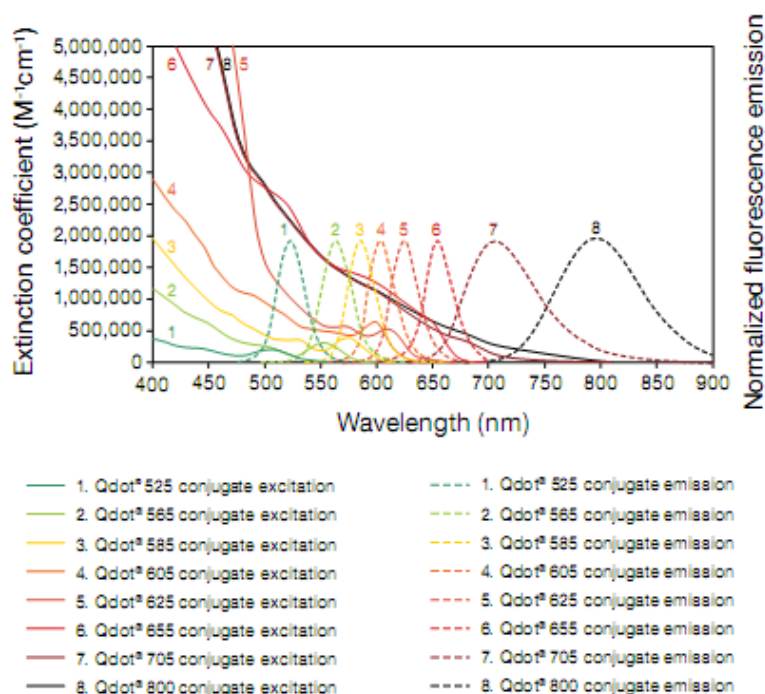


Figure 1.7 Absorption and emission spectra of different Quantum dots. Adapted from Quantum dots brochure of Invitrogen Inc.

However, the full potential of quantum dots (QDs) in biosensing was not realized until methods of synthesizing biocompatible QDs were introduced [142, 143]. Inherently, ‘naked’ quantum dots are not suitable for biological applications like immunoassays and cell related measurements because toxic elements such as cadmium (Cd) are generally involved during synthesis of quantum dots. Therefore, a reliable protecting layer outside the semiconductor nano-crystals is necessary to prevent leakage of the toxic elements into biological environment. Moreover, biological applications normally require water-soluble

fluorescence probes. Hence, quantum dots also need to be made water-dispersible through surface modification.

As shown in Figure 1.8, typical biocompatible quantum dots are core-shell structures functionalized with specific coatings. Commercial available quantum dots often consist of CdSe (from Sigma-Aldrich, Invitrogen, Evident and Plasmachem), CdTe (from Plasmachem) and InP or InGaP (from Evident) as the core material. The enclosing shell can be made of ZnS or ZnS/SiO₂, protecting and stabilising the inner core. An outer surrounding layer such as a polymer coating is used to modify the surface chemistry. Consequently, the quantum dots become water soluble and can be attached to target biomolecules through specific bonding.

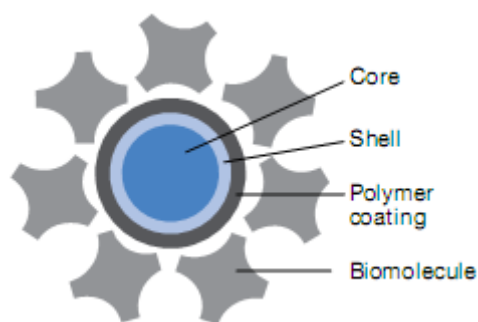


Figure 1.8 Schematic of the overall structure of a functionalized quantum dot. Adapted from Quantum dots brochure of Invitrogen Inc.

1.5.5 Instrumentation for fluorescence measurements

Generally, laser induced fluorescence (LIF) detections can be performed by using a laser light source, a lens, a dichroic filter, a band-pass or long-pass filter, and a photodetector. The target sample is excited by focused laser light passing through a lens. To reduce the laser background noise, an episcopic configuration is normally applied for excitation and emission light paths. The dichroic filter can reflect the laser light onto the sample but let the emission light collected from the sample go through to the photodetector. A band-pass or long-pass filter can be used to further reduce spectral crosstalk from the excitation light.

When simultaneous, high throughput detections are required, multiple fluorophores, either organic dyes or inorganic quantum dots, are necessary to label various targets in the sample. To separate signals arising from different fluorophores, a combination of optimal

dichroic mirrors and band-pass filters is crucial for the whole experimental configuration. Figure 1.9 shows the schematic setup of a three-color fluorescence measurement which involves three organic dyes including Cy3, Cy5 and Cy5.5. A solid-state laser excites a sample at 532 nm through a $\times 100$ oil-immersion objective. Emission from the multiple dyes is collected by the same objective and separated by dichroic mirrors and filtered out by bandpass filters. It is worth noting that 1 mirror, 3 dichroic filters, 3 band-pass filters, 3 photodetectors (APD) and more than 4 lenses were employed in this experiment setup. Besides considerable components and the relatively complicated configuration, the whole system needs to be extremely well-aligned to perform the required multiplexing fluorescence detection.

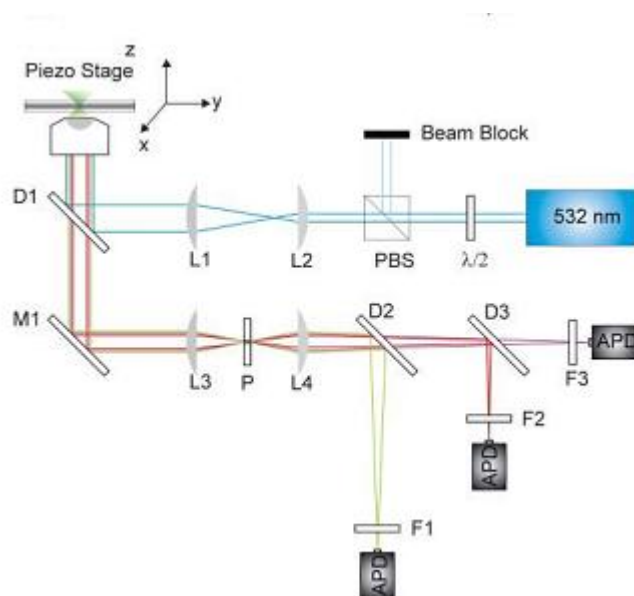


Figure 1.9 Schematic setup of multiplexing fluorescence measurement. Adapted from S. Hohng et al. (2004) *Biophysical*, **87**, 1328-1337 [123]. The confocal setup was made on an inverted microscope (Olympus, IX50). A solid-state laser excites a sample at 532 nm through a $\times 100$ oil-immersion objective. Emission from the multiple dyes is collected by the same objective and separated by dichroic mirrors and filtered out by bandpass filters. D1, D2, D3: dichroic filters; F1, F2, F3: bandpass filters; M: mirror; L: lens; P: pinhole; PBS: polarizing beam splitter; $\lambda/2$: half-wave plate; and APD: avalanche photo diode.

In the field of bio-sensing, spectroscopic analysis (e.g. fluorescence, Raman, IR spectroscopy) has been well established for a vast range of applications. Under this condition, good spectral discrimination of different wavelengths using a grating or prism type of spectrometer is required. At the macroscopic scale, these spectroscopic instruments are generally bulky and hence mounted on lab benches. Figure 1.10 provides a real picture and an optical diagram of a typical spectrometer used in many laboratories.

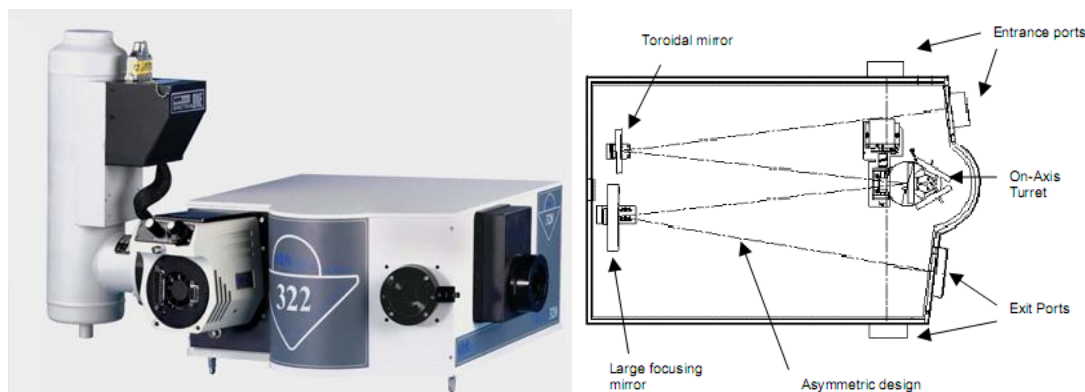


Figure 1.10 A typical spectrometer and its inside optical configuration. Adapted from Brochure of TRIAX Series spectrometer form Jobin Yvon Inc. Left: TRIAX series spectrometer equipped with array detectors. Right: optical diagram of TRIAX series spectrometer.

1.5.6 Fluorescence spectroscopy measurement

Most current fluorescence sensing methods, in which labelling is employed, detect intensity variations at fixed wavelengths corresponding to the emission of the fluorophore of interest. However, a wide range of targets, such as explosives and toxins, can't easily be measured in this way due to issues associated with sample labelling. In addition, there are many substances and environmental conditions that can affect the photo-physical properties of a fluorophore, leading to subtle changes in both intensity and the shape of its spectrum [144, 145].

Enhancing fluorescence assays by incorporating spectroscopic measurements easily would significantly enlarge the application areas for a portable biosensor, especially in those situations that favour minimal human interactions. The suitability of the AWG-microfluidic platform for performing an accurate, quantitative, spectroscopic fluorescence measurement was evaluated in this thesis by collecting the emission spectrum of Cy5 fluorophore which is a conventional organic fluorophore in biomedical sensing.

1.6 Flow cytometry

Briefly, cytometry is a process which can measure the properties of single component of a sample, such as cells or other biological particles. Since 1940s, flow cytometers have become commonly used research and clinical tools in a wide range of fields including biomedical, immunology and environmental microbiology [146-148]. The current commercial state-of-the art instruments use sample drops of $\sim 1 \mu\text{L}$, and as will be shown, the assay volume in the AWG-microfluidic system described here is $\ll 1 \mu\text{L}$. Although no cytometry measurements using the integrated AWG-microfluidic system have been made during the course of this thesis, a short review is given below so that the reader can appreciate how the AWG-microfluidic system could be used in this format in the future.

As shown in Figure 1.11, a typical flow cytometer consists of four units: (a) flow cell; (b) detection system; (c) electronic module and (d) sorting mechanism. First of all, the sample needs to be broken down to obtain a suspension of dissociated components floating free in suitable medium. Most flow cytometers use sheath flow to constrain the sample core stream to a well defined region in the centre of flow, which is called hydrodynamic focusing. Subsequently, each separate cell can be measured of its physical or chemical properties with different sensing methods involving impedance or optical systems. The flow cytometer entered a rapid development era after the introduction of laser light sources into systems [149]. A laser (or lasers) focused on the the interrogation point of the fluid stream is used for fluorescence and light scattering measurements. The excitation by a laser instead of a lamp allows optimal beam focusing on cells and simplifies the fluorescence signal filtering due to the extremely narrow laser line. Unsurprisingly, a new system named fluorescence activated cell sorting (FACS) was firstly developed at Stanford by Herzenberg's group [150, 151]. The optical signals acquired are sent to an electronic module for rapid processing and analysis. After the optical detection and cell measurement, targeted cells are separated into different collecting tubes by a specific sorting mechanism which is driven by feedback signals from the electronic module. The cell sorter typically operates under continuous flow separation and sorting mechanisms involving electric, magnetic or hydrodynamic forces cause deflections of target cells which will be collected by corresponding chambers.

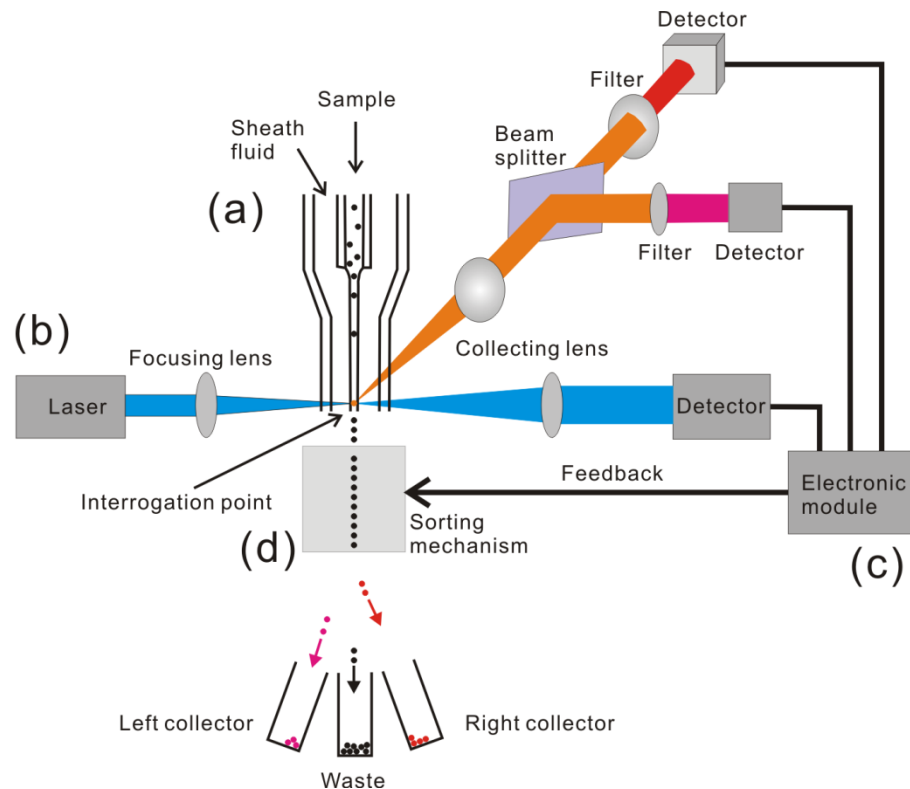


Figure 1.11 Schematic diagram of a typical fluorescence-activated flow cytometer. It consists of four units: (a) flow cell; (b) detection system; (c) electronic module and (d) sorting mechanism. The flow cell utilises the surrounding sheath fluid to obtain hydrodynamic focusing of the sample solution, thereby the cells or particles could pass the interrogation point one by one. A laser excitation beam is focused on the interrogation point and produces scattered and fluorescent light from the illuminated cell or particle. With the aid of collecting lens, beam splitters and various optical filters, both the scattering light and fluorescence signals are measured with proper photodetectors such as photo multiplier tube (PMT). For each cell or particle detected, output pulses from the scattering and fluorescence detectors are amplified and processed with a specified electronic module which will then send a feedback signal to the sorting mechanism. After receiving the feedback signal, the sorting mechanism will perform corresponding operation to ensure different types of cells or particles travel forward to specific collectors through deflecting their trajectories.

1.6.1 Microfabricated fluorescence activated flow cytometer

Although conventional fluorescence-activated flow cytometers have exceptional analytical capabilities and provide impressively efficient sorting, they are costly, bulky, and mechanically complex. For applications requiring low-cost, portable and easy-handling instruments, microfabricated fluorescence-activated flow cytometers need to be developed [152, 153]. According to the fundamental parts of a flow cytometer, the approaches of miniaturisation mainly focus on four areas: (1) using microfluidic channel for fluid handling and cell flowing, (2) employment of integrated optics, (3) miniaturization of the electronic module, and (4) integration of compact sorting mechanism. Considering relatively mature development of electronics, the microfluidics that can be used for both

the flow cell and sorting mechanism, and the integrated optics required to realize a micro-fabricated cell sorter will be discussed below.

1.6.2 Microfluidics for micro-fabricated cell sorter

Based on interrogation of a small fluidic sample volume, the flow cytometer is inherently microfluidic in nature. Thanks to advanced micromachining technology and emerging ‘soft lithography’, the flow cytometer can be transferred to a planar microfluidic platform which provides high compactness as well as flexibility [154]. It is worth noting that most microfluidic flow cytometers concentrate on simplifying construction of the flow cell by utilising the characteristics of laminar flow in microfluidic devices [155, 156]. In addition to the flow cell, other fluid handling components such as valves and pumps were also demonstrated with microfluidics. With regard to the sorting mechanism, sorting methods based on electroosmotic force, dielectrophoresis (DEP), magnetic beads labelling and hydrodynamic force were successfully implemented on a microfluidic chip [153]. It should be admitted that microfluidic devices have offered a promising small and simple platform for flow cytometry. However, most microfluidic-based flow cytometers still need to rely on bulky external optics, hence, an integrated optical detection system is in great demand.

1.6.3 Integrated optical detection system

To achieve the ultimate goal of a portable fluorescence flow cytometer, miniaturisation of optical detection system is an important consideration [153]. Conventional flow cytometers still use bulk optics and are generally established in a lab-bench environment. To scale down the size of optical detection system, compact components such as optical fibre and integrated waveguides need to be employed.

Insertion of optical fibres into pre-fabricated aligned grooves is considered to be the most simple and direct method to realize a compact optical system [157]. Although the commercially available optical fibres offer little light attenuation, there is a big challenge for applications requiring multiple excitation and collection units. Moreover, optical fibre embedded system is not an ideal on-chip system because one end of the fibre is connected

to a off-chip light source or detector while the other end is inserted into the devices with concomitant variabilities associated with alignment variations.

An alternative method is to fabricate integrated optical waveguides directly on the on-chip device by choosing appropriate materials. Patterned by precise photo or electron beam lithographic process, these integrated waveguides can deliver excitation light and collect fluorescent signal without any alignment [158]. Furthermore, light processing elements such as lenses, prisms and gratings could be realized in an on-chip format [159]. Apart from light guiding and processing components, a compact comprehensive optical detection system should also be in conjunction with small-size solid-state lasers and photodetectors.

Above all, microfabricated flow cytometers can be miniaturized by utilizing technologies like microfluidics and integrated optics and it is anticipated they will find a wide range of applications for point-of-care and on-site analysis.

1.6.4 Important trends of flow cytometry

1.6.4.1 Multicolor flow cytometry

For precise identification of cellular subsets and investigation of complex molecular functionalities, multiple parameters need to be acquired simultaneously and this purpose can be realized by multicolour flow cytometry which employs multiple fluorescent probes for labelling [160-162]. There are a wide range of organic chromophores which can be utilised as fluorescent probes for multicolour flow cytometry [114, 163]. These versatile fluorophores could conjugate with various molecules such as antibodies, DNA and lipids, and provide high sensitivity. Many of them are already commercially available while some remain to be synthesized in the laboratories. By contrast, a new type of fluorophore called quantum dot has attracted numerous attention due to its unique optical properties [164, 165]. Broad absorption spectra and narrow emission spectra enable the quantum dots to be ideal probes for multiplexing analysis in which a single laser could provide all the excitation and all the emission spectra are easily distinguishable.

1.6.4.2 Spectral analysis and Raman flow cytometry

Traditional fluorescence-activated flow cytometers always need to conjugate the target cells or molecules to specific fluorescent probes such as organic fluorophores or biofunctionalised quantum dots. However, it should be noted that not all biological molecules could be labelled with proper probes. Moreover, the extra labelling step would increase complexity of the measurement and under some circumstances affect the intrinsic biological events. By contrast, Raman spectroscopy could provide a label-free detection since Raman spectrum of a sample can be utilised as a ‘molecular fingerprint’ for identification. If basic spectroscopic capabilities can be incorporated into an on-chip micro flow cytometer, spectral analysis, not just limited to Raman detection, of target molecules, cells or particles may enable a range of new applications in biological and chemical analyses [166, 167].

1.7 Absorption spectroscopic measurement

UV-visible absorption spectroscopy is widely used in chemical analysis due to its specificity and its quantitative nature. Compared to fluorescence detection, the occurrence of colour in many natural, as well as labelled, materials makes the simple and direct absorbance method suitable for a wide range of possible applications including analytical chemistry, clinical diagnostic, and environmental monitoring.

For a target material, the absorption spectrum is the fraction of incident light absorbed by the material over a range of wavelengths. In a classical measurement of absorption as shown in Figure 1.12, a tunable monochromatic light source passes through the target analyte in a sample cuvette. The transmitted light signal is then received by a photon sensitive detector. Generally, a double beam system is implemented, which has two dedicated positions for the sample and the reference respectively, hence it can eliminate the errors induced by the cuvette material, variations in white light power levels and other environmental factors. The absorption spectrum is immediately acquired after tuning the monochromatic light source over the wavelength range of interest.

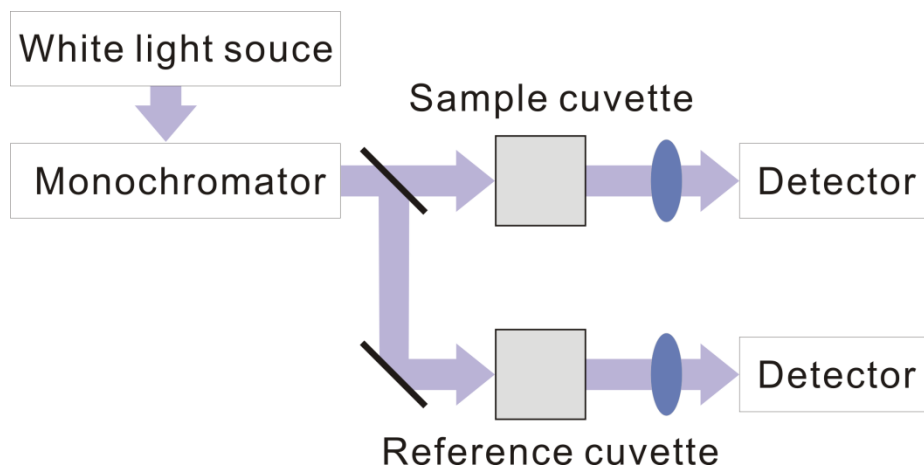


Figure 1.12 Schematic of double beam absorption measurement. The combination of white light source and monochromator provides a tunable monochromatic light which are divided into two beams by a splitter. The two separate light beams pass through the sample cuvette and reference cuvette respectively and the transmitted light signals are received by the detectors.

1.7.1 On-chip approaches for absorption spectroscopy

Absorbance based measurements rely on the Beer-Lambert law through the following relationship:

$$A = -\text{Log}_{10}\left(\frac{I}{I_0}\right) = \varepsilon cl \quad 1.1$$

Where I_0 and I are the intensity of the incident light and the transmitted light, respectively; ε is the molar absorptivity of the sample; c is the molar concentration; l is the effective absorption light path; $A = \varepsilon cl$, is the absorbance of the sample material.

The Beer-Lambert law states that the absorbance is light path dependent and this poses a severe problem for performing a sensitive and reliable absorbance measurement with a microchip where the fluidic channels are usually of small dimensions. However, many researchers have investigated different methods to address this on-chip problem. For example, embedded ‘air mirrors’ have been designed and fabricated to increase the absorption light path by reflecting the light while micro lenses were utilized to collimate the divergent light beam from the light source [23]. In other work, liquid core waveguides, based on total internal reflection, have been utilized to increase the sampling pathlength while maintaining a small detection volume [168]. Despite the relatively low sensitivity of absorbance measurements with microchips compared to fluorescence, the instrumentation

simplicity offers an advantage in certain applications. Therefore, miniaturization of an absorbance measuring system is desirable.

Microfluidics has been proved to be able to provide a miniature platform for fluidic sample handling. Incorporating optical fibres into the microfluidic chip is a simple approach minimizing the number of required on-chip optical components for absorbance measurements [28, 169]. However, most of the microchip based absorbance measurements still rely on external optical components such as light source and photon detectors, which are usually bulky and complicated.

The integration of optical components in a microfluidic platform is considered an effective way to tackle the miniaturisation problem. Thanks to the advancement of micro-machining technology, various optical functions including light sources, lenses, gratings, and photon detectors have improved the capabilities of monolithically integrated microfluidic chips [10, 15-17, 19]. Possibly the simplest format for absorption detection at a specific wavelength without bulky optics can be easily realized by positioning a laser diode (LD) on one side of the channel in the chip and placing a photodiode in the other side. However, an on-chip spectrometer is necessary if the absorption spectrum needs to be obtained. It should be noted that existing developments of devices with miniature spectroscopic elements are generally still in their infancy.

1.7.2 Absorbance measurement with an on-chip spectrometer

As discussed in Section 1.2, various techniques can be used for micro-spectroscopic components. However, there are only a very limited number of examples that have been demonstrated for absorbance measurements using these techniques. Waveguide gratings are the most popular candidates to perform an on-chip spectroscopic analysis and they have been used in the investigation of absorption measurements for over 20 years [103]. In early studies, buried diffraction gratings were employed for both the light coupling and simultaneous multi-wavelength detection. The absorption measurements were made by dispensing a small volume of Congo Red dye onto a thin film waveguide, over the region

where the light beam propagates between the in-coupling and out-coupling gratings. The Fabry-Perot optical interference filter allows the use of a white light source for illumination and can be designed to yield a narrow passband around the wavelength at which the absorbance measurement is conducted [46]. In another configurations, by directly depositing the dielectric filters onto detector arrays such as a CMOS imager, a polymer microfluidic chip can be placed straightaway on top of a detector to form an extremely compact and highly integrated sensor. Moreover, the dielectric filters can be deposited with a deliberate thickness variation, resulting in a specific wavelength response for each element in an imaging array [170, 171]. An array of dielectric filters therefore provides multiple optical channels each of which is sensitive to a unique, narrowband of wavelengths. These systems have been shown to work for the measurement of the concentration of different biomolecules simultaneously with the same device and the sensors were also able to acquire the absorption spectrum of a specific analyte. Despite the high degree of integration and parallel analysis capabilities, a disadvantage of this system is that dielectric filters require relatively complicated fabrication process with high quality of accuracy.

Compact and planar arrayed waveguide grating (AWG) devices have also been explored for absorption measurements by making use of their wavelength dispersion properties [172]. By using a parabola-shaped waveguide for sample injection, an absorbance measurement was made in which chlorophylls a and b were discriminated for applications in the field of environmental sensing. This work conceptually proved that a compact planar spectroscopic sensor using an arrayed waveguide grating (AWG) could meet the conditions for both miniaturization and high wavelength resolution. In the work described in Chapter 6, this concept is extended to the field of microfluidic sensing.

1.7 Thesis outline

The work in this thesis deals with the design, fabrication, characterization and application of the visible range AWG devices that integrate with microfluidic chips as shown in Figure 1.13. Spectroscopic measurements including fluorescence and absorption spectral analysis can be performed with the aid of a CCD detector. Details of the integrated system will be elaborated in the following chapters.

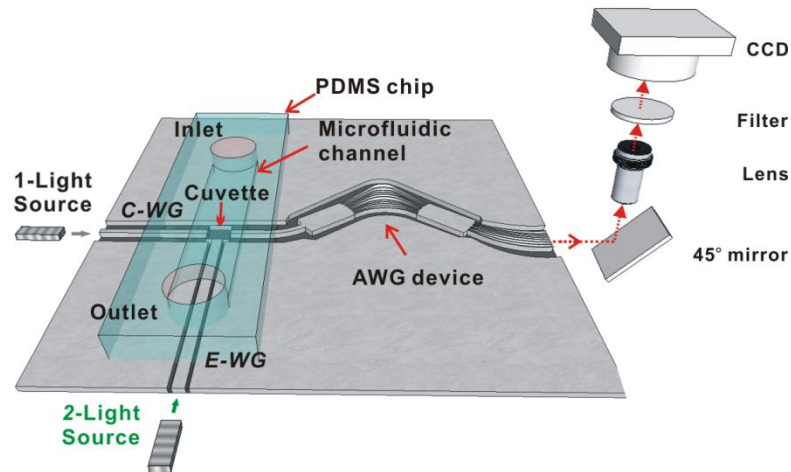


Figure 1.13 Schematic of the AWG-microfluidic platform with CCD detection

The following chapters are organized as below:

Chapter 2 introduces the fundamental theory of arrayed waveguide grating (AWG) devices. A specific design strategy based on Rowland circle configuration is provided and the simulation of an 8-channel visible AWG device is given.

Chapter 3 provides an overview of the fabrication process flow for both the AWG devices and microfluidic chips. Both photolithography and electron beam lithography are discussed. The developed and optimised lithographic, metal lift-off and dry etching techniques are described and analyzed. A moulding fabrication process for polymer microfluidic chips and an oxygen plasma bonding method is used to obtain an integrated AWG-microfluidic system.

Chapter 4 presents the experimental scheme and instrumentation that were employed for optical characterization of the AWG-microfluidic system. Following this, fluorescence

measurements based on quantum dots, Cy5 and propidium iodide are described and analyzed.

Chapter 5 describes a localised spectroscopic detection that based on lens-aided waveguides with focusing properties. Localised quantum dots fluorescence detection was performed and analysed. In addition, micro-beads based multi-color fluorescence assay was conducted.

Chapter 6 demonstrates absorption spectroscopy measurements with the AWG-microfluidic system. Using the AWG device as a colorimetric pH sensor, the pH dependence of the absorption spectra of bromophenol blue were measured and the results were compared to that obtained from a conventional spectrophotometer and a pH meter.

Chapter 7 summarizes the thesis and proposes future work for this research.

2. Chapter 2

AWG theory, design and simulation

Abstract

This chapter introduces the fundamental theory of arrayed waveguide grating (AWG) devices. Waveguide material considerations focus on using AWG devices for biological measurements in aqueous environment. A Rowland circle based AWG configuration is described and two critical parameters, namely, dispersion and free spectral range (FSR) are deduced from the basic AWG equations. Subsequently, a design strategy for the visible AWG device is described and important parameters are presented. Single mode condition and minimum bending radius of the waveguide were simulated to obtain a specific, optimal AWG design. Finally, the simulation result of a 8-channel AWG device operating at 680 nm with 10 nm wavelength spacing is given.

2.1 Introduction

Arrayed waveguide gratings (AWG) were first reported by M.Smit in 1988 as novel focusing and dispersive components which can be used as (de)multiplexers and wavelength filters [106, 173]. Since then, AWG devices have found many applications in systems that involve wavelength division multiplexing (WDM) links and networks [107, 174]. Most of the current AWG devices operate in the near-infrared wavelength region because the low-loss windows at 1310nm or at 1550nm are used for fibre optical communication. However, near-infrared light is not recommended for biosensing in aqueous environment because of the strong absorption of light by water, which may cause detrimental heat or unwanted optical signal absorption. According to the water absorption spectrum shown in Figure 2.1 [175], the absorption coefficient in 1540nm is about 11.83 cm^{-1} which means 70% of the incident intensity will be absorbed over the path length of 1mm; this absorption will easily heat and even kill the biological cells. Therefore, the work in this thesis was aimed at designing an AWG biosensor working in the range of ultraviolet (UV), visible and the near infrared (NIR) region below 900 nm.

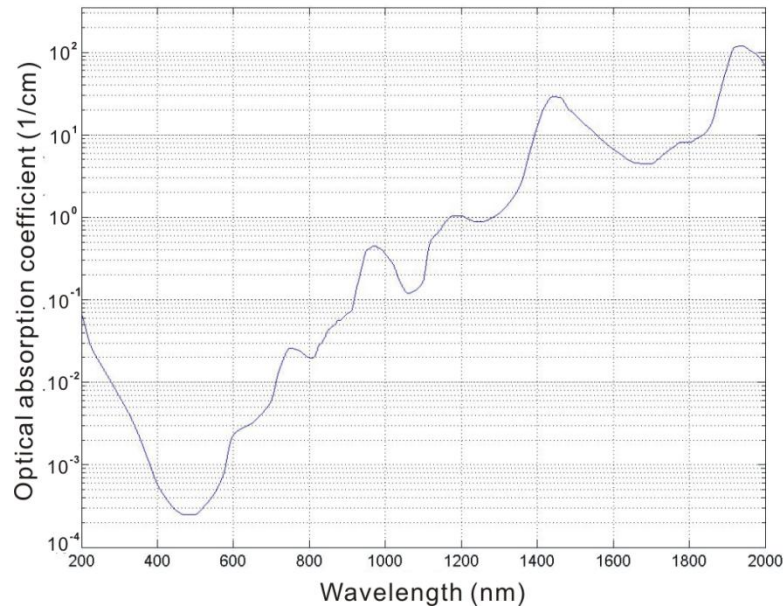


Figure 2.1 The spectrum of water absorption. Adapted from [175].

2.2 Material consideration for visible AWG

Different kinds of waveguide materials have been used to fabricate AWG devices, namely, silicon-on-insulator [176-178], semiconductors (InP, GaAs and InGaAsP) [179-181], silica [182-184], silicon-oxynitride (SiON) [185], and polymers [186]. According to the optical data in Table 2.1, silicon and semiconductor materials are not suitable to work in the target visible wavelength range. Although polymer material is flexible and can be easy to fabricate, it is to some extent too fragile and not resistant enough to corrosion by some chemical or biological reagents. Additionally, many polymer materials have poor UV transmission and their autofluorescence under UV radiation is a potential barrier for optical detection [187, 188]. Hence, silica (SiO₂) and silicon-oxynitride (SiON) were decided upon as being the most suitable materials to fabricate AWG devices working in visible range. (Note: as shown in subsequent chapters, the fabrication of well defined thick film polymer structures with the small, precise features required for the AWG design, is not trivial.)

Table 2.1 Properties of different waveguide materials [189, 190]

		Si	SiO ₂	SiON	InP	GaAs	InGaAsP
Refractive index	@632.8nm	---	1.457	1.481-1.881	---	---	---
	@1550nm	3.518	1.444	1.46-1.9 [191]	3.165	3.339	3.16-3.4
Transparent regions*	(μm)	1.1-6.5	0.16-3.8	NUV-IR	0.93-20	1.4-11	1.4-11

*Region with absorption coefficient $< 1 \text{ cm}^{-1}$.

Silicon-oxynitride (SiON) is a flexible waveguide material in the respect of both composition and refractive index. The refractive index of SiON thin films can be easily tuned over a large range, i.e., between 1.45 (SiO₂) and 2.0 (Si₃N₄); a range that allows it to be considered for different elements in the overall chip design. The most extensively applied technologies to deposit silicon oxynitride thin films are [191] plasma-enhanced chemical vapor deposition (PECVD) and low-pressure chemical vapor deposition (LPCVD). Typically, the source gases used in SiON_x deposition are silane (SiH₄), oxygen (O₂) and ammonia (NH₃). Different refractive indices of the deposited layer can be obtained by changing the gas flow ratios. The deposition rate is typically from 30 to 50 nm/min, and the thickness ranges from 0.5 to 10 μm. While PECVD is suitable for layers with lower refractive index (1.46 < n < 1.7) [192], optical waveguides with high refractive indexes (1.7-2.0) are reliably grown using LPCVD [193]. LPCVD is more suitable to form thin layers (10-500 nm), because its deposition rates range from 1 to 10 nm/min.

A small-size silicon-oxynitride AWG designed to operate at around 725 nm has been fabricated by Schauwecker, B., et al [194]. They presented experimental results of very compact (5mm × 2mm), high Δn (Δn = 4.1%), five-channel AWG with 5 nm channel spacing in the silicon-oxynitride material system.

Due to the ease of index-matching with single-mode silica fibres, silica-based waveguides have been the most extensive and important choice for the fabrication of AWG devices [183]. Silica-based optical waveguides are fabricated on silicon substrates using a process that involves the combination of flame hydrolysis deposition (FHD) [195] and reactive ion etching (RIE). For the FHD step, a mixture of SiCl₄-TiCl₄ or SiCl₄-GeCl₄ vapour is burnt in a torch using a hydrogen/oxygen gas stream. The fine glass particles synthesized by the flame hydrolysis are deposited onto the surface of Si wafers. The deposited soot is then sintered at 1200-1300 °C to form a thin glassy film. The width and height of the waveguide core are then defined by successive photolithography and RIE. A waveguide core of relatively high refractive index is realized as a consequence of the presence of oxides such as TiO₂ or GeO₂ in the SiO₂ matrix, and the lower index cladding layer is created using a pure SiO₂ layer. Thus, for silica-based waveguides, the refractive index contrast (Δn) is controlled by the ratio of other oxides to SiO₂ in the mixed glass. The conventional

refractive index contrast being used is 0.25%, and it can also be obtained with medium (0.45%), high (0.75%) or super-high (1.5-2%) values for Δn [107].

Silica based AWG devices for visible light have been designed and fabricated by several researchers. G.Przyrembel and B.Kuhlow evaluated the suitability of silica based AWG for shorter wavelengths into the visible range [196]. However, in that work only the simulation was shown without fabrication and experimental results. Kodate et al. proposed a compact spectroscopic sensor through using a visible AWG device supplied by Japanese NTT Photonics Laboratories [172, 197]. They scribed grooves across the AWG input waveguide to contain a sample and performed absorption spectrum measurements of different concentrated chlorophyll solutions. However, a major limitation with absorbance measurement in microfluidics is that the optical path length is generally very short and consequently the optical absorbance is very small, as determined by the Beer-Lambert law.

Table 2.2 compares the experimental properties of visible AWG devices made in previously mentioned researchers' work.

Table 2.2 Experimental properties of visible AWG devices

	SiON AWG [194]		Silica AWG [172, 197]
Index contrast (Δn)	4.1%		0.75%
Waveguide dimension (μm)	0.3 (Height) \times 4 (Width)		3.0 (H) \times 4.2 (W)
	Type 1	Type 2	
Central wavelength (nm)	726.5	725.8	800
Diffraction order	30	28	7
Number of output channels	5	5	8
Wavelength spacing (nm)	4.6	5.2	12.5
Insertion loss (dB)	4.5-7	4.5-6	~4
Crosstalk (dB)	< -30	< -30	< -15
Device dimension (mm \times mm)	5 \times 2	< 5 \times 2	26 \times 5
Applications conducted	None	None	Absorption spectroscopy

In this work, flame hydrolysis deposited (FHD) silica was used to fabricate a compact AWG that operated in the visible range. The choice of FHD silica over SiON (or polymers), each of which have their own merits, was in part a pragmatic selection guided by the availability of good quality material and local expertise. The FHD silica wafer, comprising 2 μm FHD germanium (Ge) doped SiO_2 as waveguide core and 8 μm BPSG (Boron-Phospho-Silica-Glass) underlayer, was purchased from Gemfire Europe Ltd (Livingston, U.K.). The custom specification for these wafers included a refractive index contrast between layers of 1.5% with 1.478 for the core and 1.456 for the under-cladding.

In the section below, the AWG configuration and working principles will be introduced briefly. Then, design considerations for a visible AWG will be provided.

2.3 AWG configuration and working principle

2.3.1 AWG structure

Arrayed waveguide grating (AWG) is a planar device that is based on an array of waveguides with both imaging and dispersive properties [107]. The AWG splits the wavelengths of the input light, and focuses them onto spatially different output waveguides.

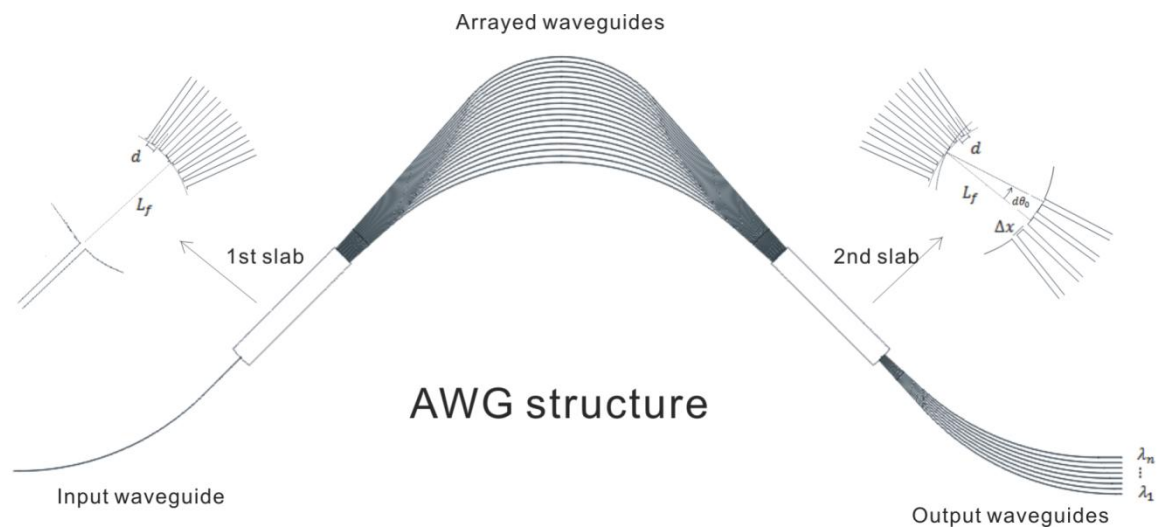


Figure 2.2 AWG configuration

The configuration of an AWG comprises 5 essential parts as shown in Figure 2.2: the input waveguide; 1st slab waveguide; arrayed waveguides; 2nd slab waveguide and output waveguides. Light coupled into the input waveguide traverses 1st slab waveguide (also called 1st star coupler) and then enters arrayed waveguides (channel waveguides). The optical path length in each arrayed waveguide is slightly different because of the particular geometrical design and consequent physical increment in length between adjacent waveguides. The design is such that this increment in length is a constant. Thus, a constant phase shift is induced when the light exits from arrayed waveguides into the 2nd slab region. This phase difference leads to constructive interference across the 2nd slab region and the entrances of output waveguides are located at positions where interference maxima occur. Consequently, light of different wavelengths is collected by different output waveguides. Although the light is transmitted rather than reflected, the working principle of AWG is still quite similar to that of a conventional diffraction grating as displayed in Figure 2.3.

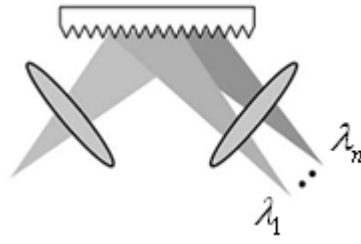


Figure 2.3 Equivalent optical system of AWG

The working principle of an AWG is based on light interference induced by a constant optical path length difference. So a critical part of AWG is the region of arrayed waveguides, where the optical length difference can be tailored for different purposes. Apart from arrayed waveguide design, that of the two slab regions needs careful consideration. Here, a Rowland circle configuration is used, as shown in Figure 4, to provide the advantage of reducing aberrations [198-200]. The input waveguide and output channels are placed along the Rowland circle while arrayed waveguides are distributed along the grating circle with a constant angular spacing. The Rowland circle has a radius of $R/2$ and is tangent to the grating circle on the edge.

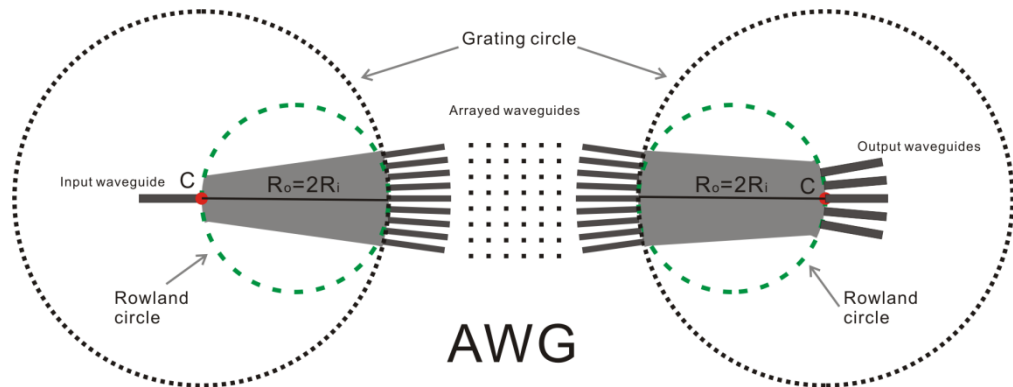


Figure 2.4 Rowland circle configuration of AWG

2.3.2 AWG equation

The important variables used in AWG structure are listed in Table 2.3.

Table 2.3 Variables used in AWG structure

Symbol	Description
λ_c	Center wavelength
m	Diffraction order AWG operates
ΔL	Optical path length difference between adjacent arrayed waveguides
$L_f(R_o)$	Focal length of slab waveguide (Radius of grating circle)
d	Pitch of adjacent arrayed waveguides
Δx	Pitch of output waveguides
$\Delta \lambda$	Wavelength spacing between adjacent output waveguides
Δf	Centre frequency spacing between adjacent output waveguides
FSR	Free spectral range of AWG
θ_i	Diffraction angle in input slab waveguide
θ_o	Diffraction angle in output slab waveguide
i	Number of i th input waveguide away from centre
j	Number of j th output waveguide away from centre
n_s	Effective refractive index of slab waveguide
n_a	Effective refractive index of arrayed waveguides
n_g	Group index of waveguide mode, $n_g = n_a - \lambda_c \cdot \frac{dn_a}{d\lambda}$
N_{chan}	Number of wavelength channels
N_{out}	Number of output ports
M	Number of arrayed waveguides

For the centre wavelength λ_c , the AWG equation is

$$n_a \cdot \Delta L = m\lambda_c \quad 2.1$$

Because the two slab waveguides are symmetrical, at the centre wavelength, light coming out from the centre input waveguide will be received in the centre output waveguide. However, at other wavelengths ($\lambda \neq \lambda_c$), the circular wave front generated at the output of

arrayed waveguides is tilted with respect to the one for λ_c , and the focal point is located at a different spatial position.

For all wavelengths, the AWG equation can be rewritten:

$$n_s \cdot d \cdot \sin\theta_i + n_a \cdot \Delta L + n_s \cdot d \cdot \sin\theta_o = m\lambda \quad 2.2$$

Where:

$\theta_i = i \cdot \Delta x / L_f$, $\theta_o = j \cdot \Delta x / L_f$. Considering only the centre input waveguide is used, so $\theta_i = 0$. The equation can be written as:

$$n_a \cdot \Delta L + n_s \cdot d \cdot \sin\theta_o = m\lambda \quad 2.3$$

2.3.3 Dispersion

To get the angular dispersion of the AWG, both sides of the above equation are differentiated with respect to λ . Thus,

$$\Delta L \cdot \frac{\partial n_a}{\partial \lambda} + n_s \cdot d \cdot \cos\theta_o \cdot \frac{\partial \theta_o}{\partial \lambda} = m \quad 2.4$$

Because θ_o is very small compared to other valuables, $\cos\theta_o \approx 1$. According to equation 2.1, ΔL can be substituted with $\frac{m\lambda_c}{n_a}$, then

$$\frac{\partial \theta_o}{\partial \lambda} = \frac{m}{d \cdot n_s} \left(1 - \frac{\lambda_c}{n_a} \cdot \frac{\partial n_a}{\partial \lambda}\right) \quad 2.5$$

So the angular dispersion of the AWG is

$$\frac{\partial \theta_o}{\partial \lambda} = \frac{m \cdot n_g}{d \cdot n_s \cdot n_a} \quad 2.6$$

$$n_g = n_a - \lambda_c \cdot \frac{\partial n_a}{\partial \lambda} \quad 2.7$$

Accordingly, the linear dispersion of the AWG can be obtained by using $\partial \theta_o = \partial x / L_f$, so

$$\frac{\partial \lambda}{\partial x} = \frac{d \cdot n_s \cdot n_a}{m \cdot n_g \cdot L_f} \quad 2.8$$

2.3.4 Free Spectral Range (FSR)

Another important parameter of an AWG system is the Free Spectral Range (FSR), which is also known as the demultiplexer periodicity. This periodicity is due to the fact that constructive interference at 2nd slab waveguide region can happen for all wavelengths in the light (c.f. the observation of different orders or periods in a diffraction grating system). The free spectral range is the largest wavelength range for a given order that does not overlap with spectrum of adjacent order.

The FSR for the wavelength λ under diffraction order m can be defined by the wavelength spacing $\Delta\lambda$ (or frequency spacing Δf) when $m + 1$ order diffraction of the wavelength $\lambda - \Delta\lambda_{FSR}$ (or frequency $f + \Delta f_{FSR}$) happens at the same angle θ_0 .

$$n_a \cdot \Delta L + n_s \cdot d \cdot \sin\theta_0 = m\lambda$$

$$(n_a + \Delta n_a) \cdot \Delta L + (n_s + \Delta n_s) \cdot d \cdot \sin\theta_0 = (m + 1) \frac{c}{f + \Delta f_{FSR}} = (m + 1) \cdot (\lambda - \Delta\lambda_{FSR})$$

2.9

Where:

$$\Delta n_s = \frac{\partial n_s}{\partial f} \cdot \Delta f_{FSR} = -\frac{c}{f^2} \cdot \frac{\partial n_s}{\partial \lambda} \cdot \Delta f_{FSR}$$

2.10

$$\Delta n_a = \frac{\partial n_a}{\partial f} \cdot \Delta f_{FSR} = -\frac{c}{f^2} \cdot \frac{\partial n_a}{\partial \lambda} \cdot \Delta f_{FSR}$$

2.11

By using the approximation: $f(f + \Delta f_{FSR}) \approx f^2$, $n_a \approx n_s$, $\frac{\partial n_a}{\partial f} \approx \frac{\partial n_s}{\partial f}$, FSR can be obtained:

$$\Delta f_{FSR} = \frac{c}{n_g \cdot (\Delta L + d \cdot \sin\theta_0)}$$

2.12

$$\Delta\lambda_{FSR} = \frac{\lambda}{m} \cdot \frac{n_a}{n_g}$$

2.13

Where $n_g = n_a - \lambda_c \cdot \frac{\partial n_a}{\partial \lambda}$

As with a conventional diffraction grating, an order-sorting filter is necessary when the wavelength range to be investigated is larger than the FSR of an AWG.

2.4 AWG design strategy and simulation

After understanding the operation principle of AWG devices, a general design procedure can be summarized as shown in Figure 2.5.

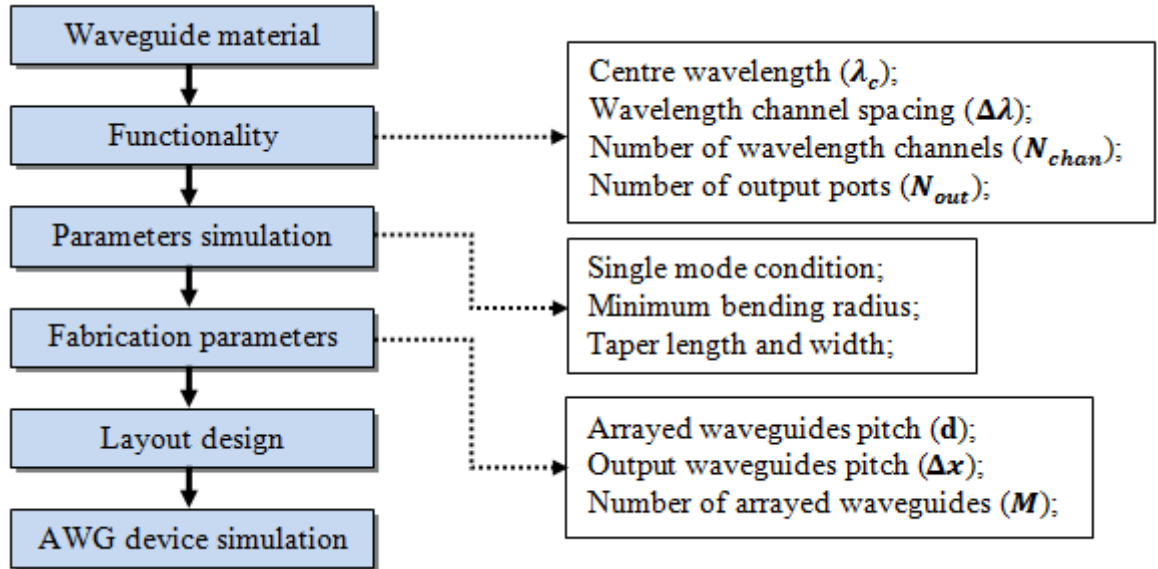


Figure 2.5 General design procedure of AWG

As shown in Figure 2.6, The FHD silica wafer consists of 2 μm FHD germanium (Ge) doped SiO_2 as waveguide core and 8 μm thermal oxidize BPSG (Boron-Phospho-Silica-Glass) underneath. The refractive index contrast is 1.5% with 1.478 for core and 1.456 for under-cladding at wavelength of 632.8 nm. As discussed in later chapters, Hydrogen Silsesquioxane (HSQ) was used as an over cladding material due to its excellent gap-filling and self-planarization properties [201]. The HSQ (Fox 16) from Dow Corning has a refractive index of ~ 1.37 (at 632.8 nm). It is worth noting that 200 nm PECVD SiO_2 can also be used as an additional protecting layer on which other fabrication steps can be performed.

Waveguide profile

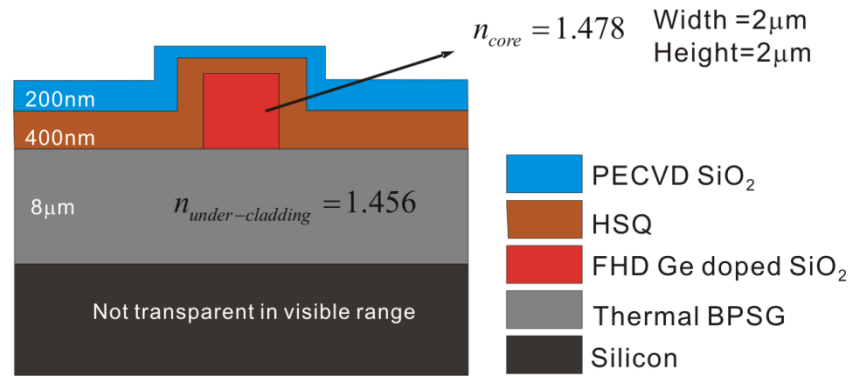


Figure 2.6 Schematic illustration of the cross section profile of the waveguide. The values of refractive indexes given correspond to those at a wavelength of 632.8 nm. BPSG: Boron-Phosphor-Silica-Glass.

The required functionality of the AWG device optimized to detect Cy5 fluorescence is:

Centre wavelength: $\lambda_c = 680\text{nm}$;
 Wavelength channel spacing: $\Delta\lambda = 10\text{nm}$;
 Number of wavelength channels: $N_{chan} = 10$;
 Number of output ports: $N_{out} = 8$;

The above values are arrived at firstly by estimating the centre of mass of the Cy5 emission peak as being 680 nm (the peak is at 670 nm). Thus, if the AWG device is designed to operate at a centre wavelength of 680 nm, the whole Cy5 emission spectrum can be covered with an acceptable resolution by using 8 outputs with ‘centre wavelengths’ spaced 10 nm apart. Following exploratory simulations and fabrication, both this number of output channels and the geometrical constraints imposed by the required bandwidth were found to be quite feasible. In our work, N_{out} is smaller than N_{chan} , which although it creates a ‘blank’ frequency gap between adjacent periodicities, also reduces the crosstalk from other grating orders.

By use of 3D BeamPROP simulation (Rsoft Ltd) with the above structure, the waveguide profile of single mode condition at $\lambda_c = 680\text{ nm}$ can be obtained. As shown in Figure 2.7, the simulation indicated that the width of the waveguide should be below $2.6\ \mu\text{m}$, provided the thickness of the FHD waveguide layer (i.e. height) is $2\ \mu\text{m}$. (Note: Mode 0 represents

the fundamental mode. When the dimension of the waveguide increases, higher order modes such as mode 1 will start to occur.)

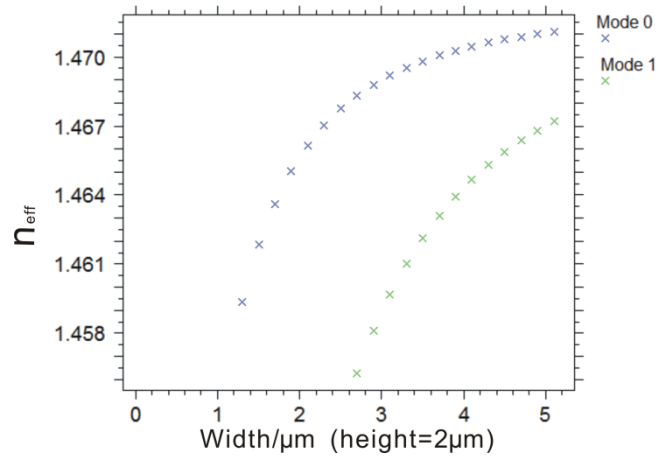


Figure 2.7 Single mode condition of waveguide at $\lambda_c=680$ nm.

Bending waveguides are unavoidable to realize the particular geometry of arrayed waveguides adapted to meet the requirement of constant optical path increment. To reduce the loss caused by bending curvatures, minimum bending radius needs to be investigated. The minimum bending radius ($Min(R)$) of waveguide is defined by the value with which the loss of 90 degree bending arc is 0.1 dB (i.e. the power after the bending arc is more than 97.724%). With the waveguide parameters (2 μm for both the height and the width), $Min(R)$ is about 400 μm as seen in Figure 2.8.

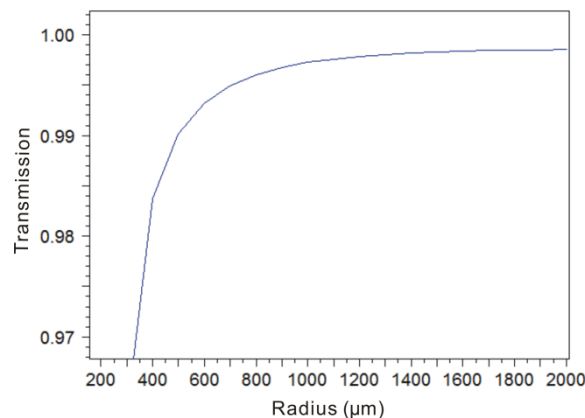


Figure 2.8 Minimum bending radius ($Min(R)$) of waveguide

From the standpoint of reducing AWG loss and crosstalk, the number of arrayed waveguides (M) should be infinite and the gap between adjacent arrayed waveguides in the

junction should be zero to ensure all the light is coupled into and out of the device. However, if layout design and device fabrication processes are taken into account, a balance is necessary between theory and real fact. As a general rule, the number of arrayed waveguides should be bigger than four times the number of wavelength channels. The value of arrayed waveguide pitch is dependent on which fabrication tool will be employed. Generally, electron beam lithography (EBL) can provide higher resolution than photolithography. Likewise, output waveguides pitch (Δx) can be determined under a compromise between device performance and its physical size.

After the independent parameters such as λ_c , $\Delta\lambda$, and N_{chan} having been determined,

other factors can be calculated. The diffraction order is fixed by $m = \text{round}\left(\frac{\lambda_c}{N_{chan} \cdot \Delta\lambda}\right)$

which is 7 in our case [$q = \text{round}(y)$: q is the integer that is closest to y]. Compared to a conventional AWG, the use of low diffraction order results from a design requirement of a short operating wavelength and large free spectral range ($FSR = N_{chan} \cdot \Delta\lambda = 100\text{nm}$).

Considering the large number of arrayed waveguides used, this imposes a challenge to both layout design and fabrication process of the AWG device because a small length difference

($\Delta L = \frac{m \cdot \lambda_c}{n_a} \approx 3.2\mu\text{m}$) is required.

As shown in Figure 2.9, with assistance of the AWG Utility from Rsoft Design Group, layout of the AWG can be created provided all the waveguide parameters have been given.

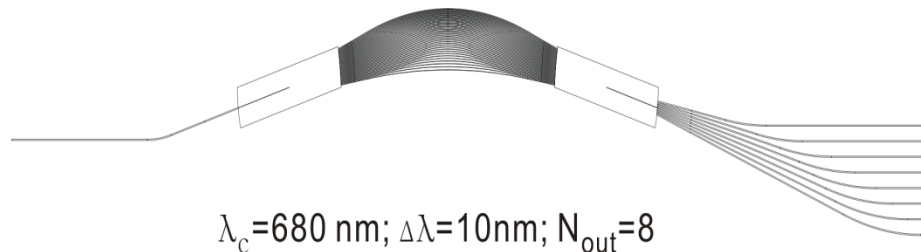


Figure 2.9 AWG design layout

The AWG was designed to work at centre wavelength of 680 nm and there are 8 output ports with 10 nm wavelength spacing. The size of AWG device was 12.1mm×1.5mm. The

simulation result using the Beam Propagation Methods (BPM) software for the AWG device is given in Figure 2.10.

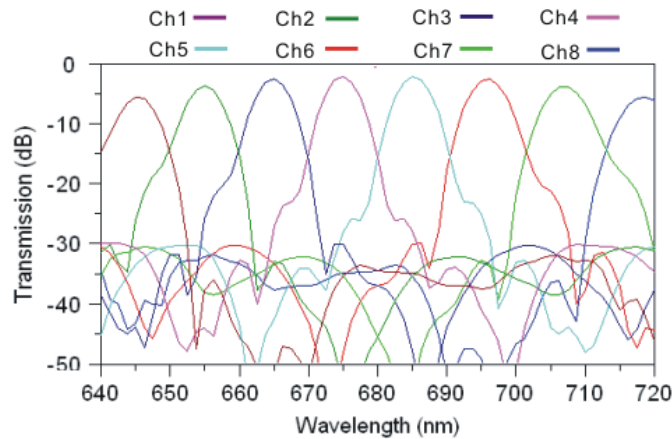


Figure 2.10 Simulation result of AWG device

Based on fundamental design of the visible AWG device, different adjustments could be employed for various applications such as absorption and emission measurements, each of which will be presented in the following chapters.

2.5 Summary

In this chapter, the AWG technique was introduced and described. Considering ultimate target applications of biological measurements in aqueous environment, FHD silica was chosen to fabricate the AWG devices working in visible region. Furthermore, a classical configuration based on Rowland circles was utilized to design the AWG device. Prerequisite waveguide simulations including single mode condition and minimum bending radius were performed in order to obtain optimal physical parameters for a specific AWG design. Finally, the output performance simulation was conducted for an 8-channel AWG device ($\lambda_c=680$ nm, $\Delta\lambda=10$ nm) that would be used for measurements in the following chapters.

3. Chapter 3

Fabrication of AWG device and microfluidics

Abstract

This chapter investigates the fabrication issues during the process of the AWG devices and microfluidic chips. For realisation of the AWG waveguide features, two different lithographic techniques, namely, photolithography and electron beam lithography were compared and optimized. In the photolithography process flow, a single-layer lift-off method based on an additional developer soaking step was employed, leading to a simplified fabrication process with satisfactory yield of qualified AWG devices. For the electron beam lithography process, two sensitive resists including SU-8 and UVIII were investigated. Subsequently, the reactive ion etching process was studied by testing different etching mask materials and instrumental parameters in order to obtain the optimal conditions for AWG pattern definition. The AWG fabrication process was accomplished after formation of the over-cladding and protecting layers. Following this, a final lithographic step and dry etching process were used to create a microfluidic cuvette to hold the target samples. In a parallel process, PDMS based microfluidic chips were made by moulding using a pre-fabricated silicon master. An oxygen plasma bonding method was used to bond the AWG device to the PDMS microfluidic chip, resulting in an integrated AWG-microfluidic system.

3.1 Overview of the process flow

The main processing steps for preparing an integrated AWG sensor chip are summarized in Figure 3.1. An ultrasonic solvent clean followed by washing with piranha solution ($H_2SO_4/H_2O_2 : 3:1$) was used to remove organic residues and other contaminants from the FHD silica wafer. Two lithographic techniques that can be used to define AWG structures are photolithography and electron beam lithography (EBL). In each case, after pattern definition, samples need to be processed to remove unwanted FHD glass, using reactive ion etching (RIE) with resist or deposited metal as the etching mask. Subsequently, a waveguide over-cladding layer of HSQ and a protecting layer of deposited PECVD silica are used to complete the AWG waveguide fabrication steps. At this point, a typical AWG device is ready to be tested after cleaving and mounting.

In order to perform solution based spectrophotometric assays, a sample cuvette needs to be introduced into the AWG chip. To define such a sample cuvette, the same processes as that are used for AWG structure are employed. In addition, a silicon mould for microfluidic pattern definition is prepared using standard photolithography and reactive ion etching (RIE) processes. Soft lithography using poly(dimethylsiloxane) (PDMS) elastomer is then employed to make the microfluidic channels used to deliver analytes to the sensing cuvette [202]. In the final stage of construction, the PDMS chip with suitable channels is irreversibly bonded with the cleaved AWG chip by exposing the mating surfaces to an oxygen plasma [203].

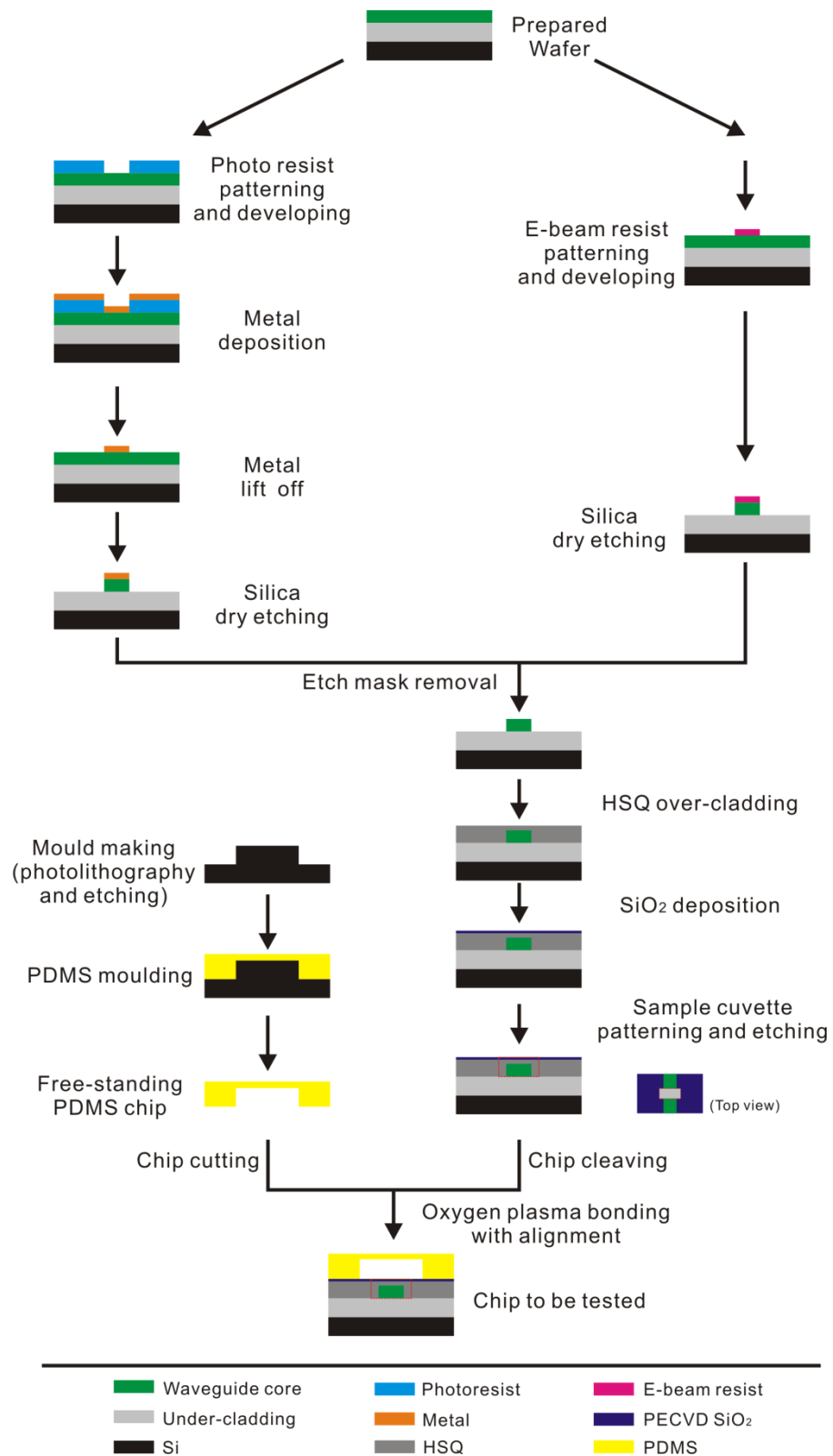


Figure 3.1 Schematic of the process steps for integrated AWG sensor chip. Either photolithography or electron beam lithography (EBL) can be used to define AWG structures. Process with Photolithography is more simple and accessible while E-beam lithography provides design with a high flexibility.

3.2 Fabrication issues and challenges

Simulation results in Chapter 2 indicated that both the width and the height of waveguide should be below 2.2 μm . In addition, ideally, to reduce AWG loss and crosstalk, the number of arrayed waveguides should be infinite and the gap between adjacent arrayed waveguides in the junction should be zero to ensure all the light is coupled into and out of the device. However, in practice, fabrication tolerances compromise the realisation of such a theoretical design. Therefore, optimisation of lithographic techniques including photolithography and electron beam lithography need to be investigated. Considering the high density of small features of the AWG design, a thin layer of photoresist S1805 was used for photolithography and a single-layer lift-off method was proposed. In the case of electron beam lithography, two sensitive resists including SU-8 and UVIII were investigated.

Lithographic techniques are used to transfer the pre-designed pattern into the resist, subsequently, reactive ion etching (RIE) process is required to realise all the design features in the ultimate waveguide material. The waveguide profiles after dry etch mainly determine the optical performance of the AWG device, thus different materials need to be tested as the etch mask and the instrumental parameters require to be investigated to obtain the optimized conditions.

3.3 Optimisation of the AWG device fabrication

3.3.1 Feature patterning via photolithography

3.3.1.1 Consideration of diffraction limits of photolithography

Fast processing and large scale production are important features of photolithography, as currently employed by industrial manufacturers. The photolithography tool in the James Watt Nanofabrication Centre (JWNC) [SUSS MicroTec Mask Aligner (MA6)] of Glasgow University is equipped with a mercury lamp and a 350 nm filter. By using a UV light source, all the features in the designed patterns can be transferred from a mask plate onto target material simultaneously. Taking into account the high density of arrayed waveguides

in the design of Figure 2.7, a thin layer of 500 nm photo resist (S1805, Shipley) was employed to transfer the AWG structure from a pre-patterned mask plate to the FHD wafer. Note, due to the diffraction limit of light illumination and the optics of the MA6 mask aligner, the resolution of photolithography is restricted to $\sim 1 \mu\text{m}$ [204, 205]. For this reason, the arrayed waveguides need to be arranged with a nonzero value for the gap between adjacent waveguides (Figure 3.2b) where they intersect with the free space slab regions as shown in Figure 2.2. If this gap is not incorporated into the design, the interface between slab region and arrayed waveguides will be messy and ambiguous resulting in degradation of AWG device reproducibility (see Figure 3.2a). After exposure, the resist pattern was developed using Microposit developer.

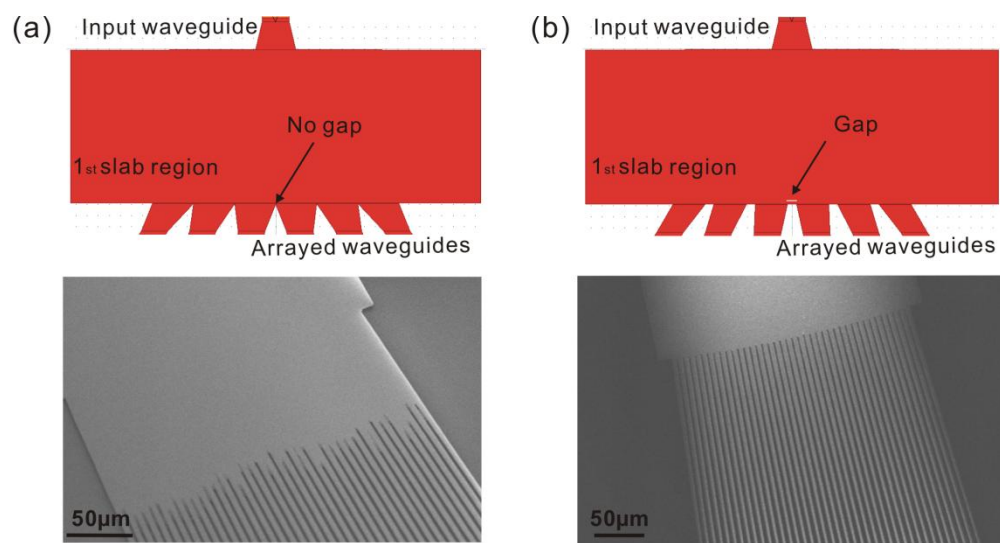


Figure 3.2 Schematics and SEM images of joint area of 1st slab region and arrayed waveguides. (a) without gap between arrayed waveguides; (b) $2 \mu\text{m}$ gap between arrayed waveguides.

3.3.1.2 Developer soaking and lift-off process for creating reliable dry etching mask

Here, commonly, the photolithography steps above are followed by a metal deposition and lift-off process to create metallic interconnections or to form a metal mask for etching process. In this work, a lift-off process was applied to obtain a 75 nm NiCr mask for the subsequent FHD silica dry etching steps.

To obtain the high resolution pattern definition required for the AWG designs, a lift-off resist (e.g. LOR) can be used as a sacrificial layer to define an undercut, making it easier

for the resist and unwanted metal to be washed away. This undercut can be tailor-made by slightly increasing standard resist developing time. In addition to the use of a sacrificial lift-off resist, gentle sonication in an ultrasonic bath can also assist in obtaining a clear pattern, although much caution needs to be taken if the structure comprises dense and small features. However, as an alternative, a single-layer metal lift-off process could be employed, instead of using a sacrificial LOR resist; here an extra fabrication step was added in which the sample with spun resist was soaked in standard developer (Microposit developer concentrate:H₂O 1:1 or Microposit MF-319) for 60 seconds before exposure. With this extra process, unwanted metal was easily lifted-off by immersing in 50 °C acetone for <15 minutes, without the assistance of an ultrasonic bath, see Figure 3.3b. Without the pre-soaking step in developer, it was not unusual to see samples with a metal residue in the small gaps at the end of the AWG structure, as shown in Figure 3.3a. It is believed that the developer soaking step before exposure modified the top surface of the photoresist by removing short-chain molecules and forming long-chain, high molecular weight molecules [206-208]. Furthermore, this would also possibly increase hydrophobicity of the near-surface layer imparted by alkaline based developer incorporation. This soak treatment reduces development rate of the surface layer, whilst the resist beneath develops at the normal rate, therefore resulting in an undercut profile after development. Compared to the multi-layer techniques, this single-layer method is inexpensive and easier to control. More importantly, the additional soaking step was experimentally proved to have simplified the fabrication and increased the yield of qualified AWG devices.

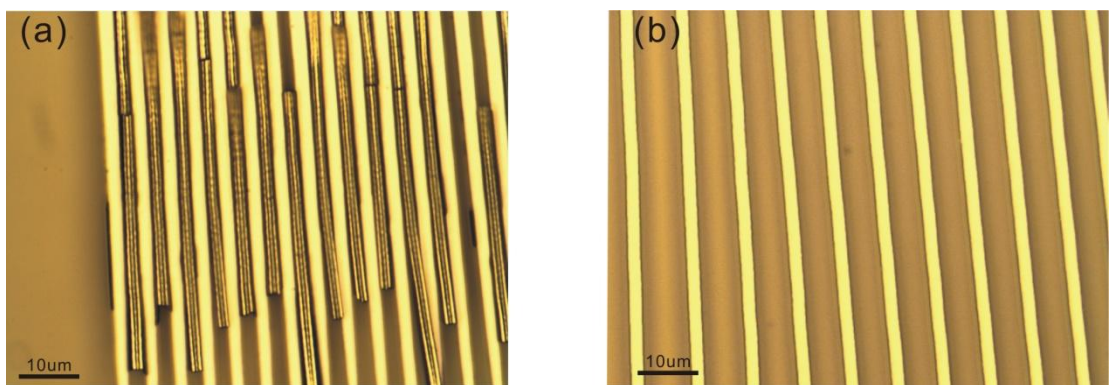


Figure 3.3 Microscopic images after lift-off (a) without developer soaking; (b) with 60 seconds developer soaking before UV exposure.

3.3.2 Optimisation of electron beam lithography process

An alternative to photolithography is Electron beam lithography (EBL). Here, instead of light, a beam of electrons is used to write a pattern in the resist through which exposed or unexposed areas can be removed by a suitable developer. However, since the EBL tool writes all the features in a serial fashion, the process of EBL is time-consuming and the throughput is not high. However, electron beam lithography offers the advantage to beat the diffraction limit of light and realize features in the nanometer regime. Furthermore, it provides a great flexibility in the iteration of an AWG design since no pre-patterned mask plate is needed.

Considering the potentially long writing times with e-beam lithography and relatively large area of the AWG device, two different resists each of which only required low exposure doses were investigated, namely SU-8 and UVIII. Note, to prevent loss of pattern definition due to electron charging effects, the resist was covered with a 10nm layer of nichrome (NiCr) before exposure in the beam-writer. (The 10 μm thick non-conducting silica on the silicon wafer would otherwise create a build up of negative charge in the FHD wafer that adversely affects the positioning of the incident electron beam.) The NiCr layer was deposited by electron beam evaporation in a Plassys MEB 400S and removed after exposure by chrome etchant (a mixture of ceric ammonium nitrate and nitric acid). In the sections below, the merits and drawbacks of using either SU-8 or UVIII are described.

3.3.2.1 Use of SU-8 as an electron beam resist

SU-8 is a negative tone, chemically amplified resist which was originally developed by IBM Research Zurich Laboratory in 1996 [209]. When this resist is exposed to UV light or an electron beam, a low concentration of a strong acid is generated and acts as a catalyst for a cross-linking process. Subsequent baking of the polymer activates the cross-linking process and regenerates the acid catalyst. As a consequence, SU-8 is a very sensitive resist and the required dose with e-beam lithography is very low.

In this work, we used the commercially available NANO™ SU-8-2002 formulation from MicroChem Corp. USA. The FHD wafer was cleaned in a solution of hot Piranha (75%

H_2SO_4 : 25% H_2O_2) followed by an oxygen plasma (60W@5min) and dehydrated on a 150 °C hot plate for 5 min. The resist was dispensed statically, followed by a ramped spread cycle to 500 rpm (100 rpm/s), and then a 600 rpm/s ramp to reach 3000 rpm which was maintained for 60s (following recommendations by MicroChem Corp.). The resist thickness was about 2 μm for SU-8-2002, as measured using profiling (Veeco Dektak). The substrate was soft baked at 65 °C for 60 s, then at 95 °C for 120 s prior to e-beam exposure. A hot plate post-exposure baking (PEB) protocol of 60 s at 65 °C plus 60 s at 95 °C was used to initiate the cross-linking process. The samples were then developed using MicroChem SU-8 Developer for 60s, (Microposit 2-methoxy-1-methylethyl acetate (EC solvent) developer was obtained from Shipley European Ltd, UK.) followed by a 10 s immersion in isopropyl alcohol, and a rinse in de-ionized water. Exposures were carried out with Vistec VB6 UHR EWF electron beam lithography system which was operated at 100 keV. When fracturing the pattern, the step size was set to 50 nm and the sample current was 1 nA. A dose of 2.5 $\mu\text{C}/\text{cm}^2$ was chosen to write the AWG structure, determined empirically by a dose test.

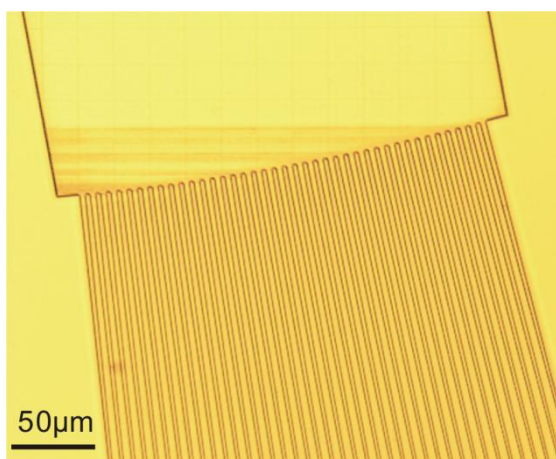


Figure 3.4 AWG structure with SU-8 e-beam lithography after resist development and the applied dose was 2.5 $\mu\text{C}/\text{cm}^2$.

Because SU-8 is a chemically amplified photo resist, it is extremely sensitive to the high energy electron irradiation. As shown in Figure 3.5 (left), the dose of 1.3 $\mu\text{C}/\text{cm}^2$ was too low so that arrayed waveguides became wavy and discontinuous. On the other hand, when a higher dose was applied, SU-8 resist between arrayed waveguides was partially polymerised and impossible to remove without affecting the AWG structure (see the area inside red dashed ellipse of Figure 3.5 b). Therefore, the high sensitivity of SU-8 didn't offer any advantage here but resulted in adverse barrier to the e-beam fabrication process because of the narrow tolerant range of dose.

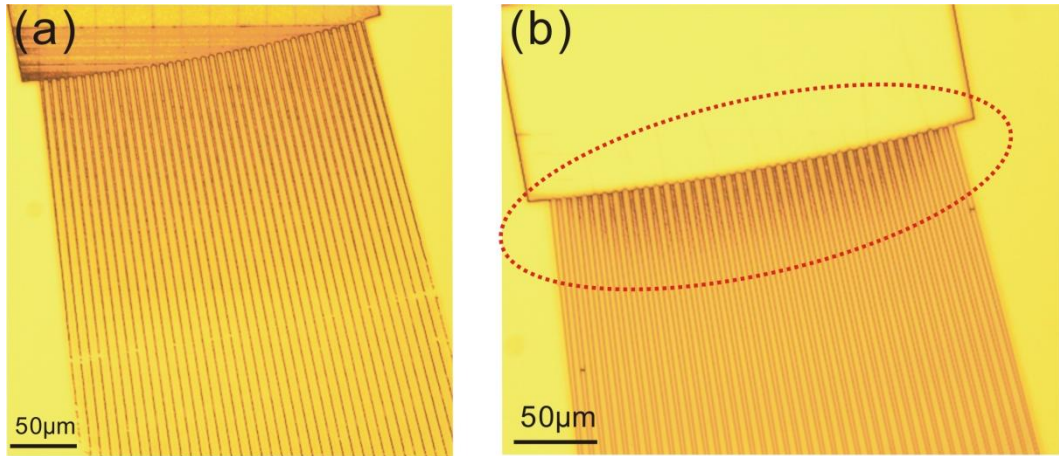


Figure 3.5 AWG structure with SU-8 e-beam lithography after resist development and the applied doses were (a) $1.3 \mu\text{C}/\text{cm}^2$ and (b) $3.3 \mu\text{C}/\text{cm}^2$. Wavy and discontinuous arrayed waveguides could be found in (a) because of lower dose used. Inversely, the right image (b) reveals higher dose effect which causes SU-8 resist between arrayed waveguides to be polymerised in the area inside the red dashed ellipse.

It is worth pointing out the challenge was not only induced by the high sensitivity of SU-8. A fundamental limitation of EBL is that the spatial distribution of electrons at the resist interface is not strictly confined within the diameter of the primary electron beam. Instead, the electrons scatter and expose resist molecules much further from the point of impact, leading to a loss in resolution and to the well known ‘proximity effect’. This is especially important when writing dense patterns such as arrayed waveguides, and extremely sensitive e-beam resists such as SU-8 will make this effect more likely to occur. Taking into account chemically amplified property of SU-8, the post exposure baking can also trigger or worsen the proximity effect [210, 211], which causes the whole process very difficult to control. Figure 3.6 shows the AWG structure with proximity effect. The gaps between arrayed waveguides were not clear but filled with polymerised SU-8 residue. From this perspective, SU-8 is not a suitable resist for AWG structure definition.

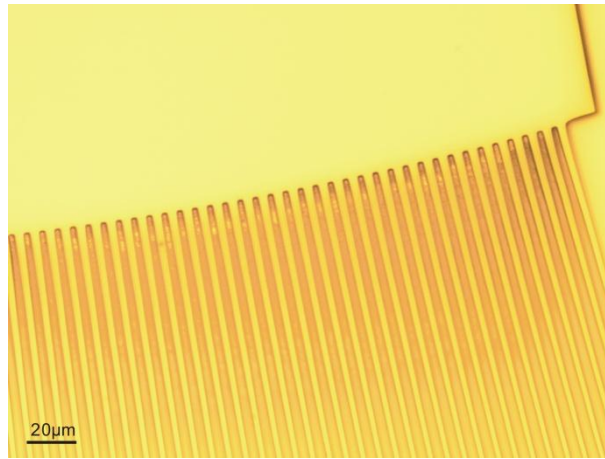


Figure 3.6 Proximity effect of AWG structure with SU-8 e-beam lithography after resist development. Inside red dashed area, the gaps between arrayed waveguides are not clear but filled with polymerised SU-8 residue.

3.3.2.2 Use of UVIII as an electron beam resist

UVIII is another chemically amplified resist but with positive tone. It contains a copolymer of hydroxystyrene and t-butylacrylate and has been designed to function with a high post exposure bake temperature in order to decrease the sensitivity of the resist to airborne contamination that can diffuse into the films, and inhibit the formation of a photoacid generator that affects resist sensitivity [212].

A primer (Hexamethyldisilazane (HMDS)) was applied to a clean FHD wafer which was dehydrated on a 150 °C hot plate for 5 min. A 900 nm layer of UVIII-0.9 (SHIPLEY) was obtained by spinning the sample at 3000 rpm for 60 seconds, and then baking on a hotplate at 130 °C for 1 minute. Dose tests were performed over the range 20-70 $\mu\text{C}/\text{cm}^2$ with 55 $\mu\text{C}/\text{cm}^2$ producing the best results as shown in Figure 3.7. Then the sample was given a post exposure bake (PEB) at 135 °C for 1 minute on a hot plate. Finally, the sample was developed for 60 seconds in Microposit CD-26 followed by a DI water rinse and nitrogen blow-dry.

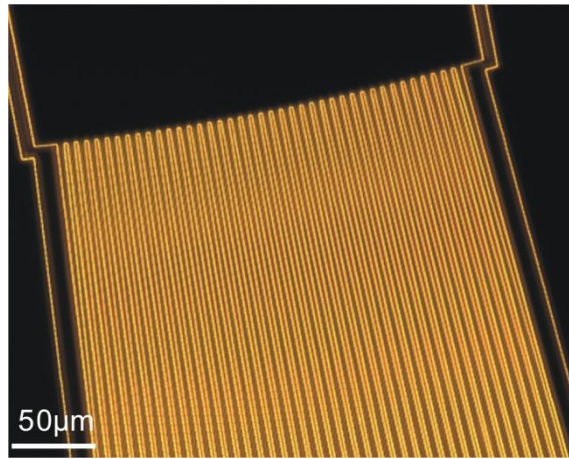


Figure 3.7 Microscopic dark field image of AWG structure with UVIII e-beam lithography after resist development and the applied dose is $55 \mu\text{C}/\text{cm}^2$.

Compared with SU-8 resist, UVIII e-beam lithography process is much more stable and reproducible. As shown in Figure 3.8, the dose of $34.5 \mu\text{C}/\text{cm}^2$ was not high enough to define the AWG structure. However, the dose test result revealed a relatively large effective range in which the AWG structures didn't show any observable difference. Additionally, the post exposure bake (PEB) sensitivity is quite low ($<5 \text{ nm}/^\circ\text{C}$, from UVIII datasheet) and is less sensitive to baking times compared to SU-8.

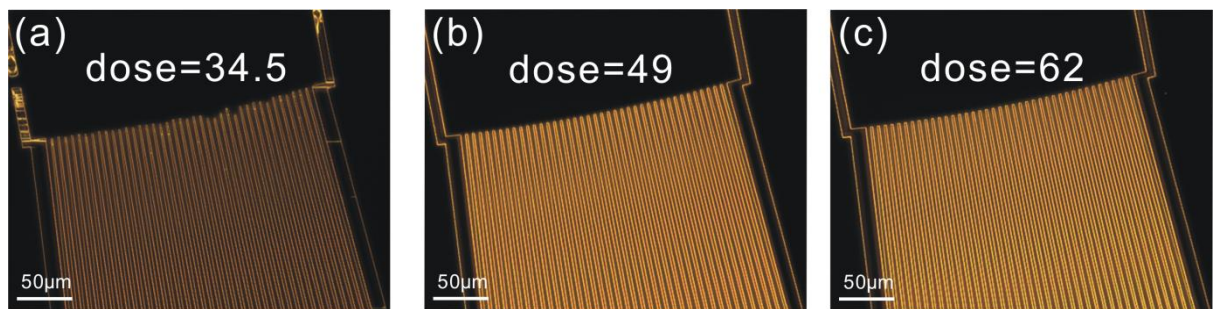


Figure 3.8 Microscopic dark field image of AWG structure with UVIII e-beam lithography after resist development. (a) under-exposed, dose= $34.5 \mu\text{C}/\text{cm}^2$; (b) dose= $49 \mu\text{C}/\text{cm}^2$; (c) dose= $62 \mu\text{C}/\text{cm}^2$. No observable difference was found of AWG structures when doses of range 49 to $62 \mu\text{C}/\text{cm}^2$ were applied.

Compared to SU-8, the improved pattern fidelity and increased yield compensate for the longer exposure times and thus UVIII was selected as the most appropriate e-beam resist to use for the AWG fabrication.

3.3.3 Dry etching process

To transfer the AWG structure from sample surface to the FHD silica waveguide core, a reactive ion etching (RIE) process was utilised. Reactive ion etching (RIE) is a mixed process in which chemical etching is accompanied by ionic bombardment. On the one hand, the bombardment helps open areas for chemical reactions and undercutting is minimized since side-walls are not exposed. On the other hand, the chemical reaction can greatly increase the etching selectivity and rate.

Figure 3.9 shows a schematic of the Oxford Instruments RIE80+ etching machine used in this work. Typically, an RIE machine consists of a low pressure chamber (5-500 mTorr) containing two electrodes, of which the lower one is connected to a strong radio frequency (RF) electromagnetic field and the top grounded electrode often actually comprises the rest of the entire chamber. The gases enter the process chamber via a ‘showerhead’ inlet in the top electrode and exit via a vacuum pump. The sample is usually not directly on the lower electrode but on a quartz or graphite “coverplate” to avoid sputtering or re-deposition of electrode material. Plasma is initiated in the system by applying a strong radio frequency (RF) electromagnetic field which will induce a negative self-bias on lower electrode. The power of the applied field is a few hundred watts with a typical frequency of 13.56MHz.

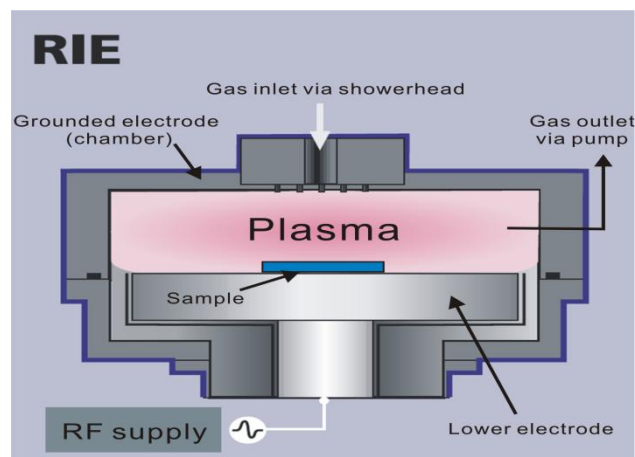


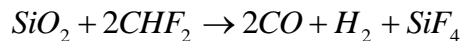
Figure 3.9 Typical configuration of a RIE system. (picture adapted from Oxford Instruments website)

It has shown that many factors can impact on etching performances such as etching rate, sidewall anisotropy, surface roughness and chamber contamination [213]. To achieve an effective etching process for the AWG device, it is necessary to optimise the instrumental

parameters, of which the choice of gas, gas flow and the power of RF are the critical ones. In addition, the combination of these instrumental parameter with the etch masks developed in the lithographic processes were also optimised as detailed in the following sections.

3.3.3.1 Instrumental parameters

Proper gases need to be employed for etching of different materials. Fluorine based chemistries have shown to be suited for silicon dioxide dry etching since a gaseous product SiF_4 is formed. Generally, gases such as sulphur hexafluoride (SF_6), tetrafluoromethane (CF_4) and trifluoromethane (CHF_3) are often used for reactive ion etching of silicon dioxide. It appears that CF_x ($x < 3$) radicals chemisorb on the SiO_2 and dissociate [214]. The radicals supply carbon to form CO , CO_2 , and COF_2 gases from the oxygen in the film. They also supply fluorine to form SiF_4 gas. Overall reactions such as the following occur [214]:



The dissociation of the feed gas is determined by the RF power. A high intensity field would break the gas down to a greater degree so that the gas would have more kinetic energy and the ion bombardment would be much stronger. The chamber pressure determines the level of interaction within the plasma. A high pressure would increase ion density, which possibly leading to an increase in etch rate. However, high pressure may also increase residence time, thus encouraging polymer deposition. The gas flow rate allows the control of the feed gas into the chamber. If the flow rate is too low, insufficient material may be discharged. However, if applied flow rate is too high, the dwell time in the chamber may not be long enough for the gas to break down. In addition, the gas flow rate and chamber pressure are inter related.

3.3.3.2 Choice of a dry etch mask

Using UVIII as a dry etch mask

Apart from performing well as a fast process electron beam resist, UVIII has been shown to have good dry etch resistance [212]. In that work it was found to be similar to that of standard photoresists. Thus, an effective dry etch mask was made using a layer of 870 nm UVIII in the above EBL process and 30-second oxygen plasma ashing after development to remove any residual resist. A final hard bake of 150 °C on a hot plate for 3 minutes was also performed before the dry etching to improve the resistance of the material.

A typical silicon dioxide reactive ion etching (RIE) process with Oxford Instruments RIE80+ machine employs a mixture gas of CHF_3/Ar with flow rates of 25 and 18 sccm respectively. The RF power was applied at 200 W and the chamber pressure was set at 30 mTorr. At this condition, the etching rate of the FHD silica was about 35.5 nm/min and the etching mask selectivity ($SiO_2/UVIII$) was over 4. In the fabrication steps used to define the AWG and waveguide pattern, the FHD wafer needed to be etched down by 2 µm. This would take ~1 hour at the above etch rate, however, after the first 30 minute of an etch run the process needs to be interrupted for the chamber to be conditioned with an oxygen plasma clean. It is worth noting that after the etching process the UVIII mask was very difficult to remove, possibly because the etching gas has further crosslinked and polymerized the UVIII resist. Thus, instead of using an RIE technique or a solvent, we used a piranha solution ($H_2SO_4 : H_2O_2 = 3:1$) to remove the polymerized UVIII [215]. A Dektak surface profilometer was used to measure the feature thickness, before and after etching process.

As shown in Figure 3.10, the process with CHF_3/Ar RIE using UVIII mask resulted in a vertical profile. However, from the SEM image of Figure 3.11 it can be seen that the side wall roughness was still not perfect, possibly caused by the non-ideal side wall of the UVIII mask which transferred its profile to the waveguide layer underneath. However, it did show a good uniformity of the etching process covering the large AWG structure as seen in Figure 3.12, and this leads to the fabrication of AWG devices with reproducible properties.

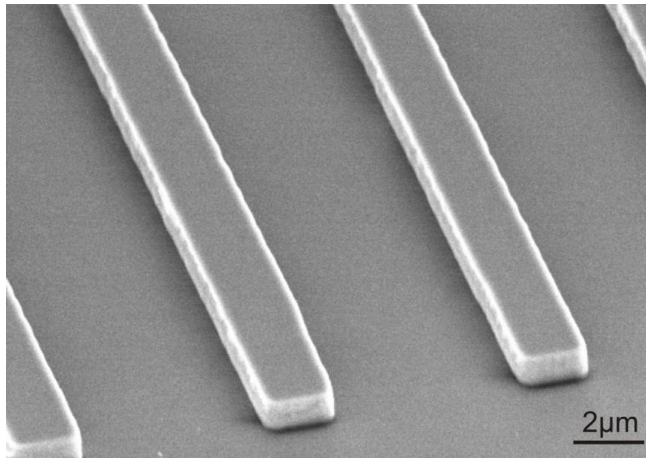


Figure 3.10 SEM image of FHD silica etching profile with CHF_3/Ar RIE using UVIII mask.

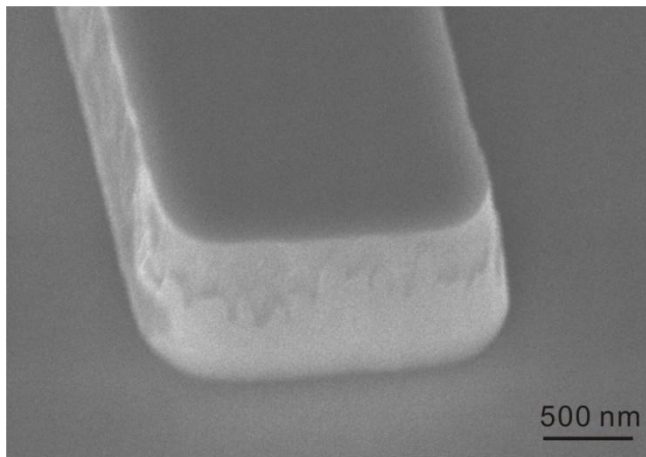


Figure 3.11 Illustration of the sidewall profile of CHF_3/Ar plasma etching using UVIII mask.

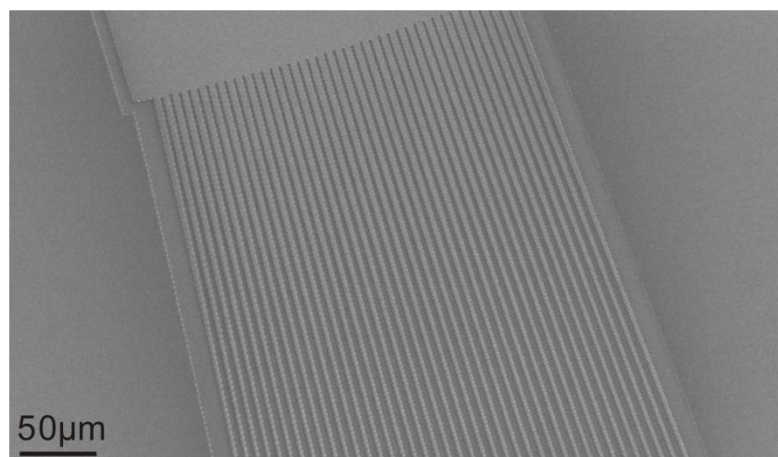


Figure 3.12 SEM image of the junction of AWG slab region and arrayed waveguides after dry etching with CHF_3/Ar RIE using UVIII mask.

Using nichrome as a dry etch mask

Whilst photoresist is the most commonly used dry-etch mask material, a relatively thick layer of resist is required in this work because of the low etching selectivity. A consequence of using a thick layer is that the thicker the resist mask layer, the greater the sidewall roughness and slope generated in the resist pattern during fabrication. Reducing the mask thickness is therefore essential to effectively reduce the mask-induced defects that are transferred into the profile of the FHD structure. Following on from previous work, this can be realised by using different metal films [216, 217]. Furthermore, by choosing a metal etching mask, a process can be developed that is compatible with photolithography using resist S1805 and thus more suited to commercially oriented fabrication procedures. (Note, a thin layer of S1805 resist (~500 nm) alone is not resistant enough to support the 2 µm FHD silica etching process [218]. Generally, the metal mask is selected based on the ease of deposition, the strength of adhesion on the substrate and the relative inertness to the reactive ion etching process chemistry. This means, for example, that the metal used should not react with the feed gas and form volatile fluorides. Nichrome (NiCr) is well known to have good adhesion to silicon dioxide and great inertness to different chemical gases [218]. Typical etching selectivities (SiO₂/NiCr) is within the range of 30:1 to 100:1 [219]. The problem of performing a RIE with a metal mask is that the metal will be physically sputter etched by the high energy ions in plasma and the sputtered metal can deposit onto other areas of the sample surface resulting in ‘micro-masking’ residues. This effect leads to a very rough surface topography [216]. The occurrence of metal redeposition is affected by a series of factors including ion species, ion density, ion energy and chamber pressure. By optimizing these parameters, a micro-mask residue free surface can be obtained [219].

In Ruano’s work [216], the FHD silica etch depths were between 12 µm and 25 µm, considerably greater than the depth required here. This means that there is a reduced likelihood of metal redeposition. Additionally, in the protocols used below, the etch runs were stopped periodically (every 30 minutes) to allow for chamber conditioning as a further precaution against the possibility of micro-masking effect.

In the NiCr mask etching processing used here, a 75 nm NiCr layer was deposited onto the FHD silica to develop and optimise the NiCr dry etch mask procedure. The RIE process was performed with an Oxford Instruments RIE80+ machine. The first set of etching process parameters tried were: 25/18 sccm CHF_3/Ar ; 200 W RF power and 30 mTorr chamber pressure. The inert gas, Ar was added to the chamber as a diluent and a plasma stabilizer [214]. The etching rate of the FHD silica was again around 36 nm/min and the etching selectivity for NiCr was in excess of 35:1. Figure 3.13 displays the waveguide profile after the etching processing. A problem, clear from the SEM image, was that the sample surface looked a bit dirty with random spot-like residues that appear to have been caused by redeposition processes.

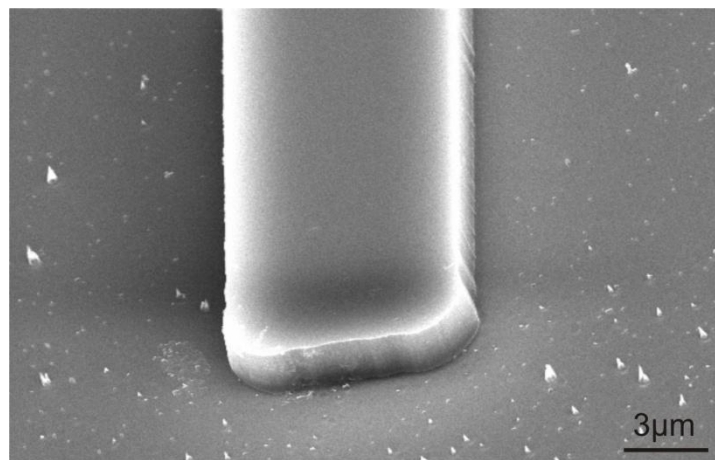


Figure 3.13 Waveguide profile of CHF_3/Ar plasma etching using NiCr mask.

It was suggested in McLaughlin's PhD thesis that addition of oxygen to a CHF_3 process can reduce the dirty nature of the etching [213]. This reduction is thought to be because the oxygen oxidises carbon based molecules and removes polymer depositions within the plasma. However, such a process also leads to a reduction in the level of the thin polymer film that can prevent waveguide sidewalls being laterally eroded. Hence, the advantages of using oxygen to control surface roughness must be balanced with the disadvantage of lateral sidewall erosion.

Bearing in mind the balance of CHF_3 and O_2 flow rates, a close to optimal dry etching process was found by using 50/5 sccm CHF_3/O_2 , 30 mTorr chamber pressure and a RF power of 200 W. Waveguide profiles generated with these parameters has a good, vertical sidewall (Figure 3.14). The sidewall roughness indicated in Figure 3.15 was very small

although a small amount of erosion of the upper sidewall still occurred. Importantly, the sample substrate surface roughness was improved significantly as shown in Figure 3.16, and this can be attributed to the addition of oxygen to the standard CHF_3 etch process. It is worth noting that the etching rate of the FHD silica and etching selectivity for NiCr were almost unaffected and stayed at a reasonable level (>35 nm/min and $>30:1$ respectively).

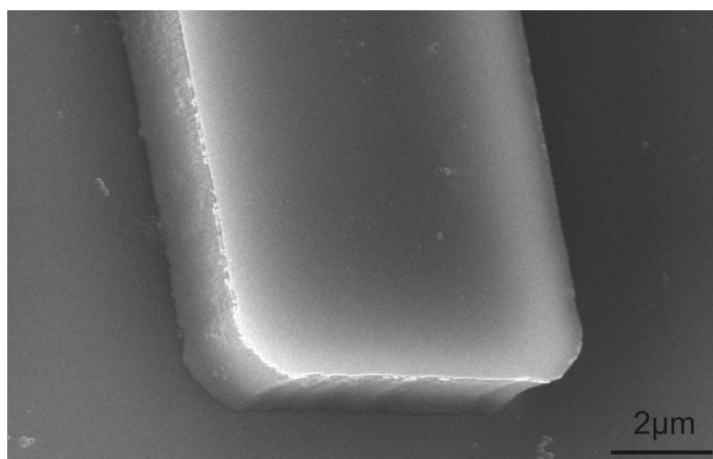


Figure 3.14 Waveguide profile of CHF_3/O_2 plasma etching using NiCr mask.

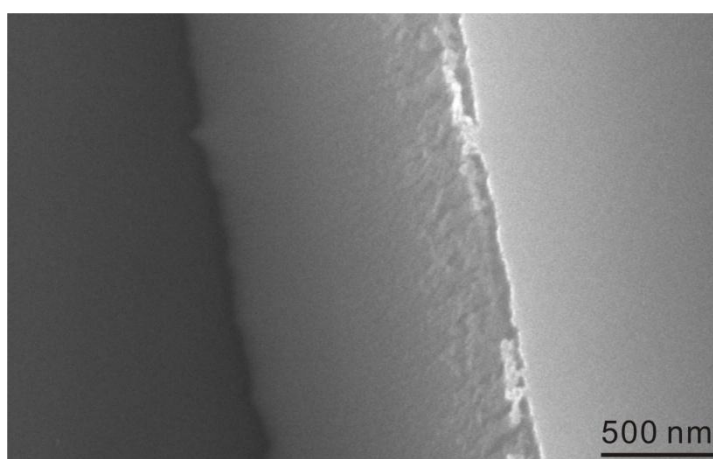


Figure 3.15 Waveguide sidewall of CHF_3/O_2 plasma etching using NiCr mask.

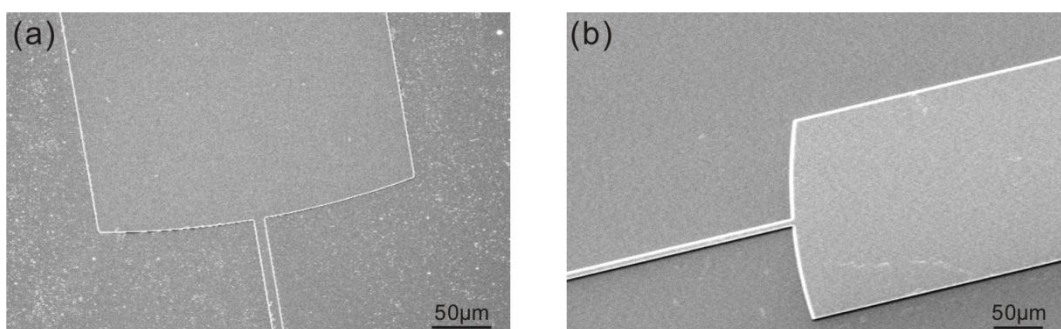


Figure 3.16 Comparison of etching processes with CHF_3/Ar and CHF_3/O_2 . (a) Dirty surface after etch using CHF_3/Ar ; (b) The addition of O_2 to the standard CHF_3 etch process improved the surface roughness significantly.

3.4 Overview of AWG structure definition

All the fabrication processes discussed in earlier sections are intended to perfectly transfer the designed structure into the real waveguide material, thereby leading to a practical device to be tested. In this work, SEM investigation was utilised to ensure the waveguide sidewall roughness and structure uniformity be kept at an acceptable level. Figure 3.17 provides SEM pictures of different regions from a fabricated AWG device. All the features including input/output waveguides, arrayed waveguides and slab junctions were well defined by lithography and dry etching process. As found from measurements made using devices fabricated early on in this work using what are notably less than optimal fabrication procedures (e.g. Fig 3.2 and Fig 3.16a), the performance of different devices in terms of optical throughput and channel cross-talk was much more variable. Whilst it cannot be determined whether or not the side-wall profiles are sufficiently smooth to give the optimal optical transmission characteristics, what has been found is that devices prepared with the characteristics such as in Fig 3.17 have a consistently similar performance.

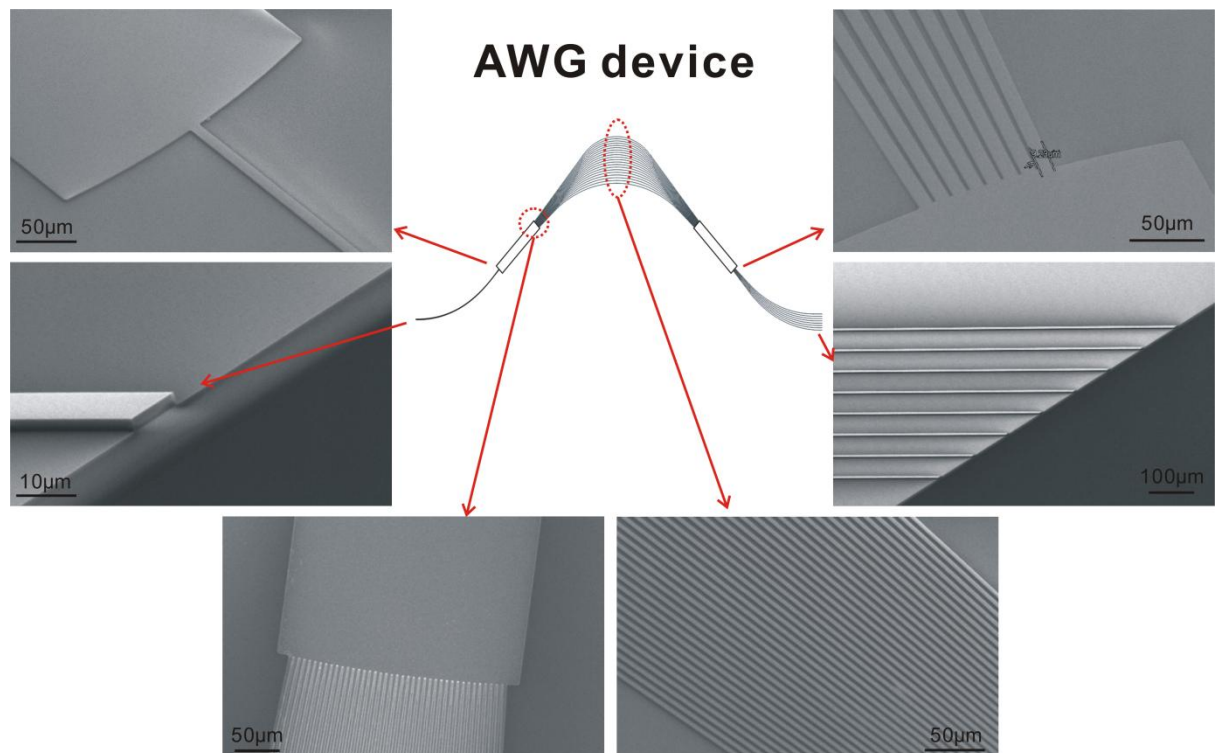


Figure 3.17 Illustration of different regions from a fabricated AWG device.

3.5 Formation of cladding layer

A silica based cladding layer was formed on the top of the AWG core structure by HSQ coating and PECVD silica deposition. Hydrogen Silsesquioxane (HSQ) is an inorganic sol gel with superior gap-filling and self-planarization properties that can be used as low-index overcladding material in many photonic applications [201]. It consists of repeated units of $\text{HSiO}_{3/2}$ which convert to SiO_x after thermal curing. It therefore has similar optical properties to SiO_2 [220]. It is commercially available in solution as FOx[®] flowable oxide from Dow Corning Inc.

After definition of the AWG structure, an over-cladding layer was formed by spin coating Dow Corning Fox-25 on the surface. Multiple spins could be used to increase the HSQ thickness although the high intrinsic tensile stress limits the maximum value of the thickness to 1.2 μm [201]. To cure the sample, it was placed into a 180 °C oven for a 60 minute hard bake.

The over-cladded sample needs further lithography and etching processes, to generate a cuvette for analyte sensing. Since the quality of the HSQ layer is important, and it is relatively fragile, a protecting layer with 200 nm PECVD SiO_2 was deposited on the surface. Figure 3.18 provides the SEM image of waveguide cross section, in which the borders of different layers are marked with white dashed lines.

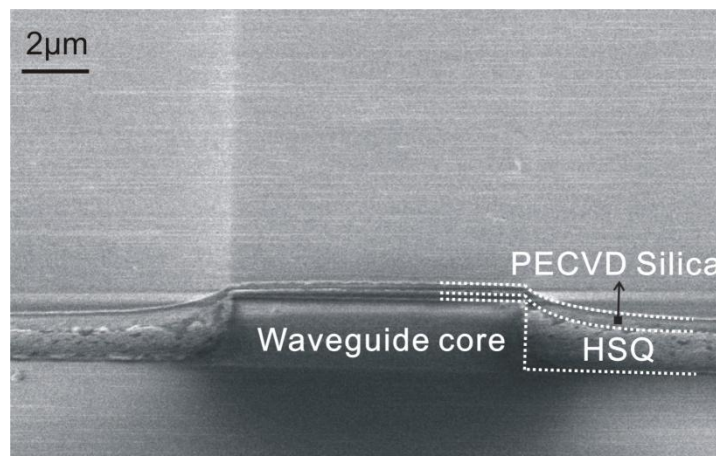


Figure 3.18 SEM profile of waveguide cross section.

3.6 Patterning of sample cuvette

To employ the AWG device for on-chip bio-sensing, a cuvette is necessary to provide a physical site for sample loading and light-matter interactions. As shown in Figure 3.19, the most direct method is to fabricate a groove across the AWG input waveguide. The groove, or in other words, the sample cuvette can be obtained by etching process.

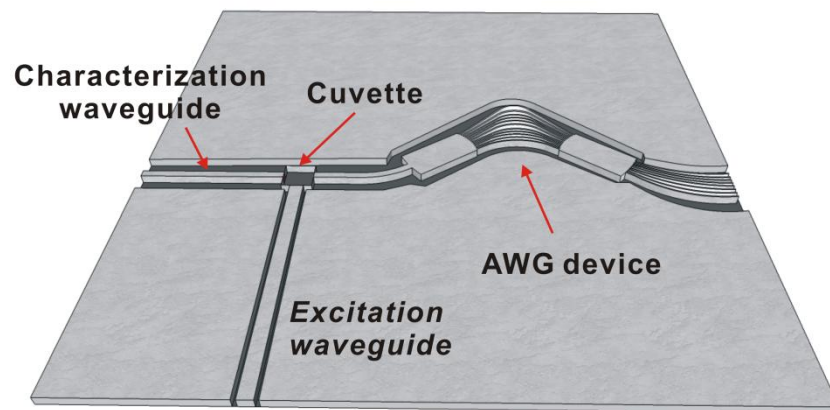


Figure 3.19 Schematic of the AWG device with a sample cuvette

Technically, the cuvette could be produced by different etching methods. However, wet etching such HF etching of SiO_2 is usually isotropic, which means the sidewall of etched pattern will not be vertical. Although the non-vertical profile of the cuvette would not affect the sample loading, it could have an adverse effect in optical applications as a consequence of the light wavefront being deformed and the light coupling efficiency being significantly decreased. Although an index-matching oil could be used to compensate and rectify the light wavefront, this method would be impractical when an aqueous sample fluid is introduced to the sample cuvette. Therefore, vertical anisotropic plasma etching is required to realize the sample cuvette on the AWG chip.

To accomplish this, a second lithography process (either photo lithography or e-beam lithography) was used to define the pattern of sample cuvette. To precisely locate the cuvette pattern in the right place, registration (or ‘alignment’) markers need to be

incorporated into the AWG mask patterns. Generally, these markers are small metal crosses and squares, which are positioned round the centre of the intended pattern area, allowing one lithographic layer to be aligned to the next. Resist lithography, metal deposition and metal lift-off are commonly involved to realize these metal markers. To reduce process steps and simplify the fabrication, etch markers rather than metal markers were used in this work. The etch markers, which could be fabricated together with AWG structure during the first lithography and dry etching process, provide good image contrast with sharp topography. The alignment process between cuvette pattern and the pre-fabricated AWG structure was performed either by the e-beam software automatically, or by manual positioning when using the SUSS MicroTec Mask Aligner (MA6).

The etching process of the cuvette was very similar to that of previous AWG structure except the thickness to be etched. In order to reach the under-cladding layer of the FHD wafer, 3 upper layers including waveguide core layer, over-cladding HSQ and PECVD silica film need to be etched through, a total etch depth of $\sim 3 \mu\text{m}$. Again, the Oxford Instruments RIE80+ machine was used to perform the dry etching process. The etching rate of FHD silica, as stated in previous dry etching chapter, was again $\sim 35\text{nm}/\text{min}$. This means the whole dry etching process of sample cuvette needs to consume three 30-minute etch runs. Considering the time for chamber conditioning between each etch run, over half day's continuous use of the RIE80+ machine was needed to complete the cuvette dry etch fabrication.

Due to the lengthy time of the dry etch jobs, selection of the mask material needs to be considered carefully. If e-beam lithography is employed, a thicker UVIII resist ($>750\text{nm}$) should be prepared to protect the unexposed area. For photolithography, a standard process with AZ4562 resist (AZ Electronic Materials) could provide $6.2 \mu\text{m}$ mask layer which is resistant enough for the dry etch job. However, when using the thick resist layer alignment under microscope is difficult since image sharpness is sensitive to the focal distance. To overcome this problem, a thinner resist such as S1818 (Shipley) could be used and an extra layer of NiCr could be deposited on the sample surface before resist spinning. This would provide an enhanced bi-layer mask with NiCr and resist both contributing to masking in the following dry etching process.

Figure 3.20 illustrates different stages of the sample cuvette fabrication. As the AWG device was to be used to measure laser induced fluorescence from the analyte, a perpendicular waveguide was designed for delivery of the excitation light (Figure 3.19 a). The original input waveguide in the AWG pattern (horizontal waveguide in Figure 3.19a) was divided into two by the formation of the sample cuvette. The left part was used to introduce a broad band light source for optical spectroscopic characterization of the AWG device while the right part was connected to the dispersive element of the AWG device which would analyze the collected light signals.

To fabricate this cuvette, a bi-layer mask with S1818 resist and NiCr was used for the dry etching process. After the lengthy dry etching job, the sample surface looked dirty possibly due to non-uniform consumption of resist layer and poor chamber condition caused by large covering area of NiCr metal mask (Figure 3.20 b and c). However, as shown in Figure 3.20d, the sample cuvette was well defined after mask material removal.

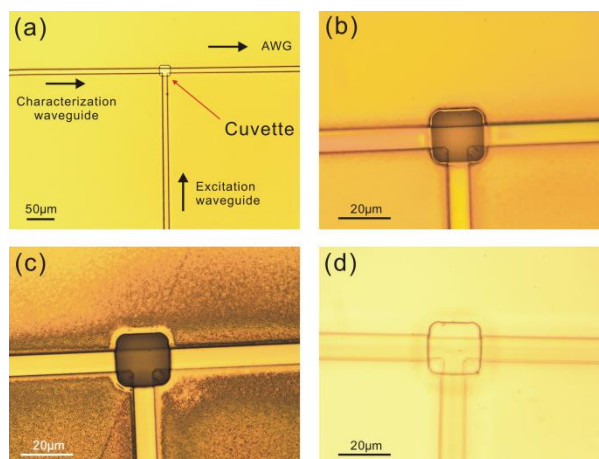


Figure 3.20 Illustration of sample cuvette fabrication. (a), after S1818 resist development. The right end of the horizontal waveguide is connected to the AWG device while the left part is used to introduce a broad band light source for AWG device characterization. The perpendicular waveguide is designed to deliver the excitation light for fluorescence measurement and the sample cuvette of $20\mu\text{m}\times 20\mu\text{m}$ is located in the central junctions. (b), after the first 30 minute dry etch with bi-layer mask of S1818 and NiCr. (c), after whole process of dry etching. The sample surface became dirty possibly due to non-uniform consumption of resist layer and poor chamber condition caused by large covering area of NiCr metal mask. (d), after mask material removal.

3.7 Integration with PDMS microfluidic chip

To realize an integrated on-chip biosensor, a functional fluidic component for sample loading and control is also required. Conventional liquid handling systems such as petri

dishes and microplates are difficult to integrate with compact planar optical systems. Fortunately, a microfluidic technology has emerged in the last 20 years which can manipulate the fluids in channels with dimension of micron scale [221]. Since the first demonstration of microfluidic device by Manz et al [108], this new field has experienced an explosive growth [222-224]. The components required for microanalytical systems can be fabricated with different materials, and polymer materials are often more favoured by researchers due to their inexpensive, flexible and easy to fabricate properties [225]. Among various polymer materials, polydimethylsiloxane (PDMS) is the most popular choice to make microfluidic devices since it is an optically transparent (down to 230 nm), bio-compatible, easy-to-make and easy-to-bond material [226-228].

A further advantage of PDMS systems is that rather than using conventional photolithography every time, a PDMS microfluidic device can be fabricated with lower cost and shorter time by using replica moulding, a fabrication method termed soft lithography [202, 229]. Following these works, in the devices described below, polydimethylsiloxane (PDMS) elastomers (or silicone rubbers) have been used as the materials to make the microfluidic chip.

3.7.1 Fabrication of a silicon mould

The PDMS chip was replicated from a mould which was produced by using photolithography and dry etching process. Figure 3.21 outlines the fabrication steps required to make a silicon mould (or ‘master’). The pattern was firstly defined in resist with a standard photolithography process and then transferred to silicon substrate by reactive ion etching (RIE). After removing the resist residue, a silicon mould was ready for use. It is worth noting that a rigid resist (e.g SU-8) after development and hard bake can also be used as the master for PDMS replica moulding [230]. The obvious advantage is this simplified fabrication procedure that it does not require repetitive dry etching processes, however, the robustness and consistency of microfluidic channel dimensions are not as good as what a silicon mould is used.

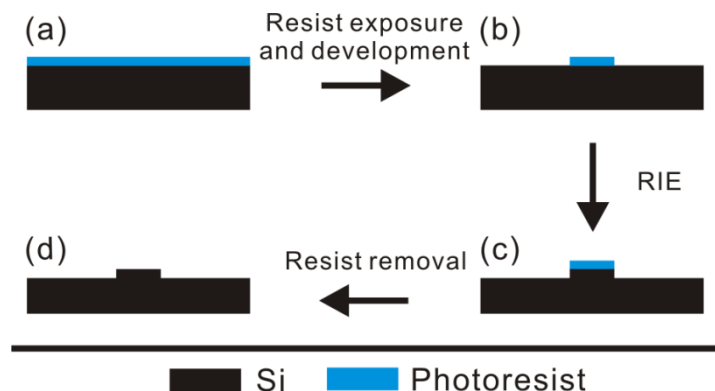


Figure 3.21 Illustration of fabrication steps to make the silicon mould. (a), photoresist was spun on the surface of silicon wafer; (b), photolithography step to expose the resist and finish the development; (c), Reactive ion etching (RIE) of silicon; (d), remove the resist residue and obtain the silicon mould.

3.7.2 Preparation of a PDMS chip

Once the silicon mould was fabricated, PDMS chips were made by replica moulding following the steps shown in Figure 3.22. First of all, the silicon mould was cleaned using acetone, isopropanol (IPA) and DI water in an ultrasonic bath followed by a blow-dry with nitrogen. The silicon mould was then placed in a desiccator under vacuum for 2 hours with a vial containing a few drops of Perfluorooctyltriethoxysilane (98%, from Sigma Aldrich). This leads to a coating of the fluorinated anti-sticking agent being formed on the silicon master, so preventing PDMS adhesion during the curing process and promoting smooth separation of the mould and PDMS after curing. After coating with the fluorosilane, a 10:1 mixture of PDMS prepolymer and its curing agent (Sylgard 184, Dow Corning) was stirred thoroughly and then poured onto the silicon mould. The PDMS filled silicon mould was then placed in a desiccator which was evacuated to remove the bubbles inside the PDMS prepolymer before being put in a 70 °C oven to cure. After curing for ~2 hours, a free standing PDMS chip with a microfluidic channel of 500 µm width and 100 µm height was obtained by peeling away from the silicon master.

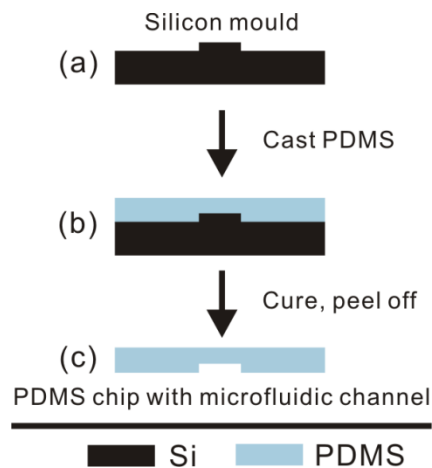


Figure 3.22 Schematic of PDMS replica moulding. (a), silicon mould was cleaned in an ultrasonic bath and the surface was treated with fluorinated silanes. (b), a liquid PDMS prepolymer (a 10:1 mixture of prepolymer and its curing agent) was poured onto the silicon mould. (c), the PDMS was cured in an oven at 70 °C. Then the PDMS was peeled off to obtain a free standing microfluidic chip.

3.7.3 Bonding of PDMS chip and AWG device

Before bonding the PDMS structure to the AWG device, small through holes were drilled into the PDMS using a tipless needle punch to produce inlets and outlets for the microfluidic channels. After this, both the PDMS chip and the AWG device were cleaned with methanol in an ultrasonic bath followed by drying for 30 minute in an oven at 90 °C. Irreversible bonding between PDMS and silica based AWG device was achieved by putting both the microfluidic chip and the AWG device into an oxygen plasma, in accordance with one of the most commonly used bonding methods in microfluidic applications [227].

The PDMS-SiO₂ bonding process is believed to work as follows. Both silica and PDMS are Si-based materials since PDMS comprises repeating units of $-O-Si(CH_3)_2-$. The oxygen plasma process generates radical groups on each surface that can go on to form a covalent $O-Si-O$ bond between the two Si-based materials and this bond can withstand 30-50 psi of air pressure and is practically inseparable. It was suggested that oxygen plasma exposure at lower RF power with shorter duration could lead to an excellent irreversible bonding between PDMS and silica surfaces [203]. In this work, the applied oxygen plasma process parameters were: RF 20W and 20 seconds.

Typically, the two treated surfaces must be placed into contact within several minutes after the oxygen plasma process, otherwise, the bonding will fail because the surface chemistry changes and goes back to their initial state quite fast in air [226]. However, because the sample cuvette in the AWG device was generally tens of microns in dimension and was expected to be covered by the microfluidic channel as shown in Figure 3.23, the bonding process required a precise alignment which may take a period of time. Additionally, the two devices must still be able to move smoothly in all directions after the contact of the two surfaces. Therefore, drops of non-swelling solvents such as methanol were placed between the treated surfaces to act as a lubricant during alignment and to prolong the working time [231]. After the bonding process, the device was left in air for a couple of hours to allow the evaporation of the solvent and formation of a strong bond between the two surfaces.

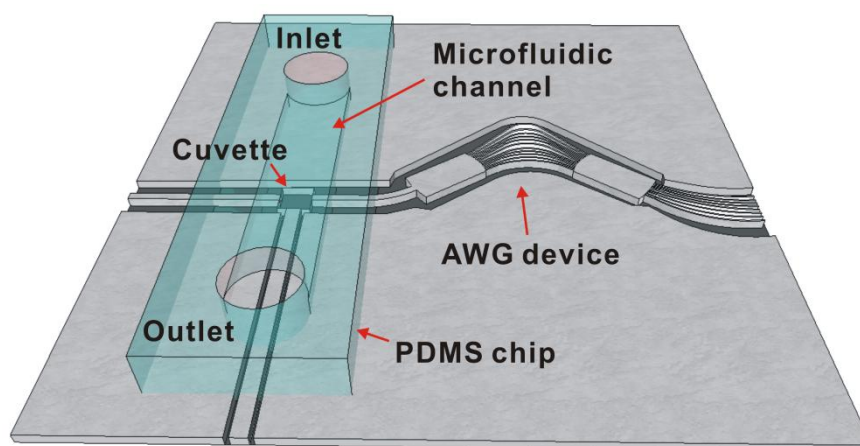


Figure 3.23 3D illustration of AWG device bonded with PDMS microfluidic chip

To make the assembled device into a complete system, inlet and outlet of the microfluidic channel were connected to polymer tubes (polytetrafluoroethylene ‘PTFE’) through tip-flattened syringe needles (BD Microlance). Figure 3.24 provides an image of the complete system including AWG device, bonded PDMS chip and necessary tubing.



Figure 3.24 Real AWG device after bonding with PDMS chip. Inlet and outlet of the microfluidic channel were connected to polymer tubings through tip-flattened syringe needles.

3.8 Summary

In this chapter a brief overview of the fabrication flow of the AWG device and microfluidic chip was given. In case of photolithography, diffraction limit was considered to optimize the AWG design to increase the fabrication reproducibility and a sing-layer lift-off technique was utilized to simplify the fabrication process. To satisfy with the flexible AWG design iteration, electron beam lithographic technique was also investigated by testing two sensitive resists, SU-8 and UVIII. Considering process stability and reproducibility, UVIII was chosen to pattern the AWG features. With regard to the reactive ion etching process, both UVIII resist and NiCr layer were tested as the etch mask materials and acceptable etching profiles could be obtained in both cases. Specifically, the instrumental parameters of dry etch using 75 nm NiCr layer were investigated and CHF_3/O_2 was proven as a better gas mixture to obtain clean, satisfactory etching profiles.

Formation of cladding layer and patterning of sample cuvette were also described. Following this, a PDMS microfluidic chip, prepared by moulding from a pre-patterned silicon master, was bonded with the AWG device using oxygen plasma method. With proper tubing and sealing techniques, an integrated AWG-microfluidic system was ready for optical characterization and fluorescence measurements.

4. Chapter 4

Optical characterisation and fluorescence measurement

Abstract

This chapter describes the optical characterisation and fluorescence measurements using the integrated AWG-microfluidic system. Two different methods were used to validate the optical performance of the AWG device, one using a white light source and a spectrophotometer and the other using a monochromatic light source and a CCD camera. Both the approaches have demonstrated light dispersing capabilities of the AWG devices, notably, the latter CCD-based method easily combined with the AWG-microfluidic system bioassay experiments. Evaluation of fluorescence detection was performed by measurements of (i) mixed quantum dots solutions, (ii) an organic fluorophore (Cy5) and (iii) the propidium iodide (PI)-DNA assay. Signals from the output channels could be used to re-create the complete fluorescence spectrum of an analyte. The work illustrated the unique advantages of the AWG-microfluidic platform for simultaneous and quantitative multiplex detection as well as its capability of detecting small spectroscopic shifts.

4.1 Validation of the optical performance of the AWG device in the visible region

4.1.1 Characterization using a white light source and a spectrophotometer

Once the protecting layer of PECVD silica was deposited as described in Chapter 3, the AWG device was ready to be cleaved and used in optical measurements. For characterization of an AWG's transmission properties, the outline scheme shown in Figure 4.1 was used. The experiment setup was established on an adapted microscope stage as shown in Figure 4.2. A white light source (Anritsu MG922A) ranging from 400 to 1600 nm was utilised to acquire the transmission spectrum of the AWG device. As shown in Figure 4.3, tapered lensed fibres were used for the input and output coupling. The spectroscopic characteristics of the output light signals from the AWG device were analysed using a conventional spectrometer (TRIAX 320, Jobin Yvon) with typical acquisition times of 1 second. To aid alignment, the AWG sample was viewed on an upright microscope fitted with a CCD camera (Andor iXon) and fibre positioners mounted on the sample stage. Optical images of the input and output channels, and the disposition of the lensed fibres were taken using this camera.



Figure 4.1 Experiment diagram to characterise the AWG device with a white light source and a spectrometer.

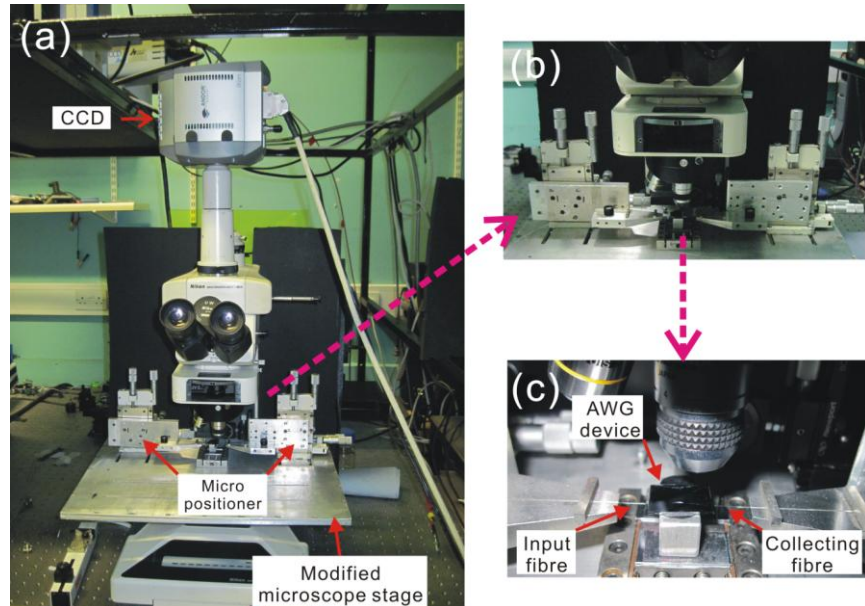


Figure 4.2 Experimental setup for characterising the AWG device with a white light source and a spectrophotometer. (a) Photo of the experiment platform. The white light source and spectrophotometer are fibre connected and not shown in this picture. (b) A close view of the fibre micropositioners and sample stage. (c) A close view of the AWG device and disposed fibres.

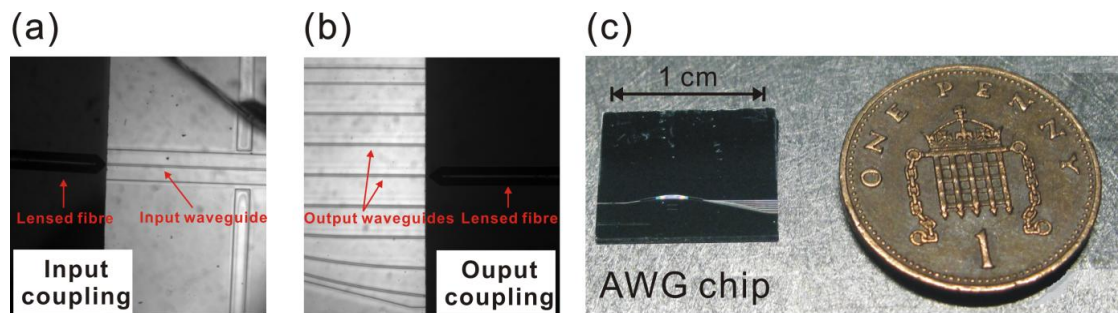


Figure 4.3 Microscopic images of (a) input coupling and (b) output coupling with lensed fibres. (c) A picture of an 8 output channel AWG chip compared to one British penny.

As shown in Figure 4.3c, the fabricated AWG device has a length scale of 1 cm, which can be seen compared with a British penny. The spectra collected from the AWG output channels (Figure 4.4) show that the full width at half maximum (FWHM) of each output peak is about 10 nm, which is consistent with simulations obtained using BeamPROP software (Rsoft Ltd) (see Chapter 2 AWG simulation). Due to the high coupling loss between the lensed fibre and the AWG chip, quantitative results of the device's insertion loss are not given in this thesis. Regarding the crosstalk, the practical AWG device experienced deteriorated performance compared to the simulation result. One major cause of crosstalk are random errors in the phase transfer of the arrayed waveguides, resulting

from random or uncontrollable variations in the waveguide width, layer thickness or composition. Another cause of crosstalk is the generation of higher order modes in the array at junctions between straight and bent waveguides or other irregularities. It should be noted that stray light propagating in the 8 μm underlayer of the AWG device could also contribute towards high background light levels, and hence crosstalk. To obtain better crosstalk performance, arrayed waveguides that are specifically designed for low excitation of higher order modes, as well as improved lithographic and etching process need to be employed.

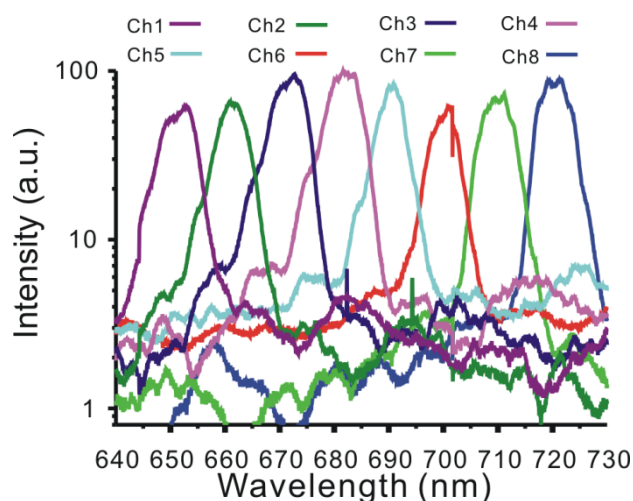


Figure 4.4 Experimental transmission spectrum of the AWG device. Intensities scaled so that the maximum transmission equals 100 arbitrary units. Different colours indicate signals from each output channel.

4.1.2 Characterisation of AWG-Microfluidic device with a monochromatic light source and a CCD camera

As an alternative to characterising the AWG device using a white light source and a spectrophotometer, a monochromatic light source and a CCD detector can also be used (Figure 4.5). In brief, using a broad band light source as the input, the monochromator can provide a mechanically selectable narrow band of wavelength of light, which is coupled into the AWG device via a tapered lensed fibre. To obtain the light intensity distribution from all output channels resulting from injection of the narrow-band light, the outputs are imaged onto a CCD detector using a low magnification objective lens. Thus, by collecting CCD images for a selection of monochromatic wavelengths, the spectroscopic performance of the AWG device can be analysed and evaluated.

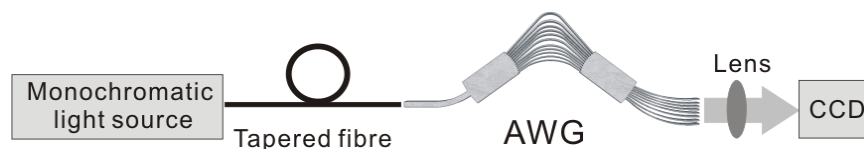


Figure 4.5 Experiment diagram to characterise the AWG device with a monochromatic light source and a CCD camera.

A white light source was used as the input for the monochromator, which produced output light of narrow-band (FWHM $\sim 2.2\text{nm}$). Figure 4.6 shows a representative spectrum of the monochromator output with centre wavelength at 680 nm. To couple the narrow-band light into the AWG device, a lensed fibre was employed. The fibre obtained commercially, has two asymmetrical terminals: one end is a standard FC connector and the other is a single-mode bare fibre with lens curvature at the tip. A conventional lens-to-fibre coupler was used to focus the monochromator output into the lensed fibre through the end with standard FC connector. The bare lensed fibre was fixed on an aluminium V-groove fibre holder of which the position could be adjusted accurately in 3 axes using a micro-positioner.

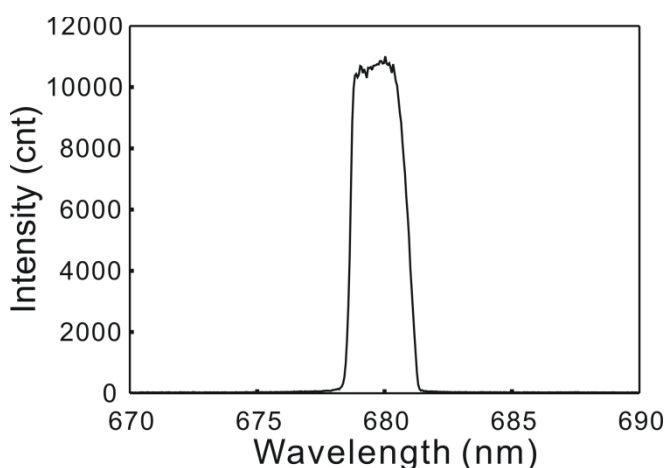


Figure 4.6 Spectrum of monochromator output with centre wavelength at 680nm.

In order to characterize the AWG device over a wavelength range from 650 nm to 720 nm, the monochromator output needs to be scanned over the same range. Considering the monochromator output and CCD sensitivity are not uniform over such a range of wavelengths due to the properties of the grating, input white light source and the detector material, it is necessary to obtain the intensity profile for the region by imaging the monochromator output directly onto the CCD and spectrophotometer. This data was then used to calibrate the AWG device performance. For example, Figure 4.7 presents the intensity profile of the monochromator output from 650 nm to 720 nm.

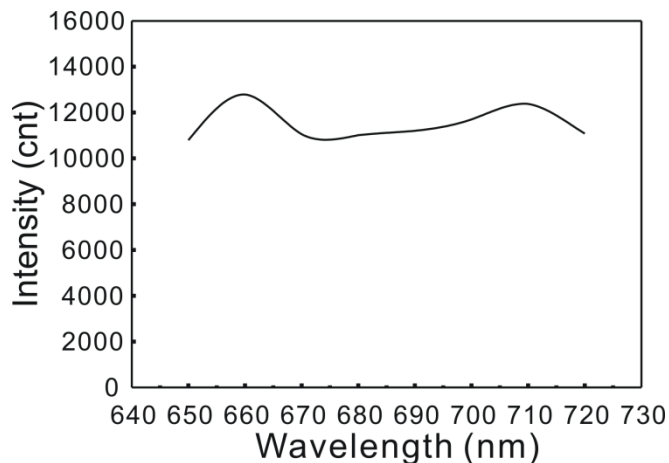


Figure 4.7 Intensity profile of monochromator output from 650 nm to 720 nm.

The advantage of this characterisation method is that ultimately, the AWG device is designed to work as a spectroscopic component and integrated with an array detector (e.g. CCD). Therefore, a CCD-based characterisation method is compatible with the experimental configuration for fluorescence based bioassay measurements. Notably, the AWG device can be characterised in this way after integration with the PDMS microfluidic chip. As shown in Figure 4.8, the AWG-microfluidic system can be used to perform bio-sensing measurements directly after the AWG device characterisation, without any rearrangement of the experimental set up.

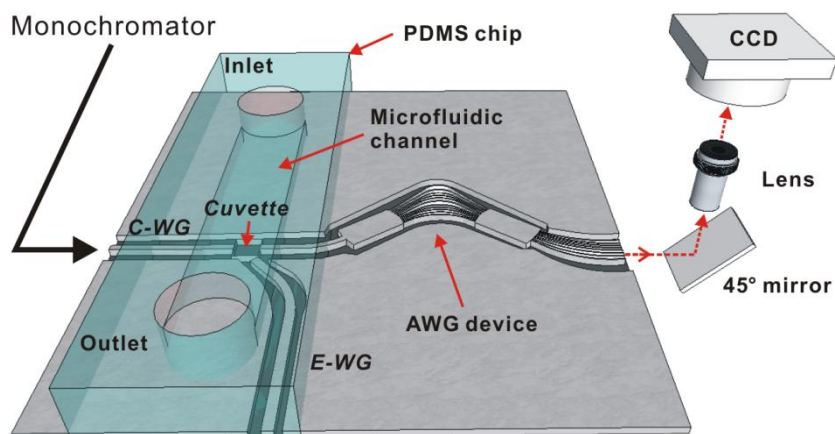


Figure 4.8 Illustration of CCD-based characterisation method for the AWG-microfluidic system. A monochromator was used to provide mechanically tuned light of narrow-band wavelength. A 45° mirror and a $\times 4$ objective lens were used to reflect AWG output signals onto a vertically mounted CCD camera.

It can be seen from Figure 4.8 that the monolithic integrated AWG-microfluidic platform contains three units: 1) light source waveguides, 2) sampling region (Note: this can be part of a microfluidic network), and 3) an AWG device. The initial design of the sampling

region consisted of a square shaped cuvette located at the junction of the light source waveguides and the AWG input waveguide. The characterisation waveguide (C-WG in Figure 4.4) crosses the centre of the sample cuvette and extends to the AWG input waveguide in a straight line. This allowed characterisation of the AWG device and could also be used for absorbance analysis. The off-axis waveguide (E-WG) was used to provide the excitation light in a fluorescence measurement. It intercepts the sample cuvette at an angle of 45° to the AWG input waveguide axis, to reduce the amount of excitation light entering the AWG, (Note: In a fluorescence measurement, the excitation light intensity is generally much higher than that of the emitted light. Similar to previous 90° configuration shown in Figure 3.19, the 45° scheme used here was also utilised to physically prevent most of the excitation light entering the AWG input.). Lastly, a 45° mirror and a $\times 4$ objective lens were used to reflect AWG output signals onto a vertically mounted CCD camera (Andor iXon).

The characterisation results of the AWG-microfluidic system using the CCD-based method are given in Figure 4.9. On the left side are the acquired CCD images of output signals from 8 output channels of the AWG device. These CCD images show the distribution of power in the 8 output channels at different wavelengths. It is clear to see that the position of the brightest spot was shifted from Ch1 to Ch8 as the injected narrow-band light wavelength was tuned from 650 nm to 720 nm, which is as expected from original design of the AWG device and the spectrophotometer based characterisation of section 4.1. Corresponding to each of the CCD images, the right side part of Figure 4.9 displays plots of the light intensity profile measured along a horizontal line that connects the light spots of the output channels in the CCD images. It can be seen clearly from these intensity profile plots that for each of the monochromator settings, not all of the light comes out from the expected channel. Indeed, each of the output channels emits some light, although at differing intensities. In practice, however, since most of the monochromatic light does exit from the expected output channel, CCD images from ‘unknown’ light source can be analyzed using pattern recognition methods by using images such as in Figure 4.9 as the basic set. Quantitative analysis of CCD images allows one to obtain a more accurate ‘result’ by using calibrated data that includes cross-talk intensities.

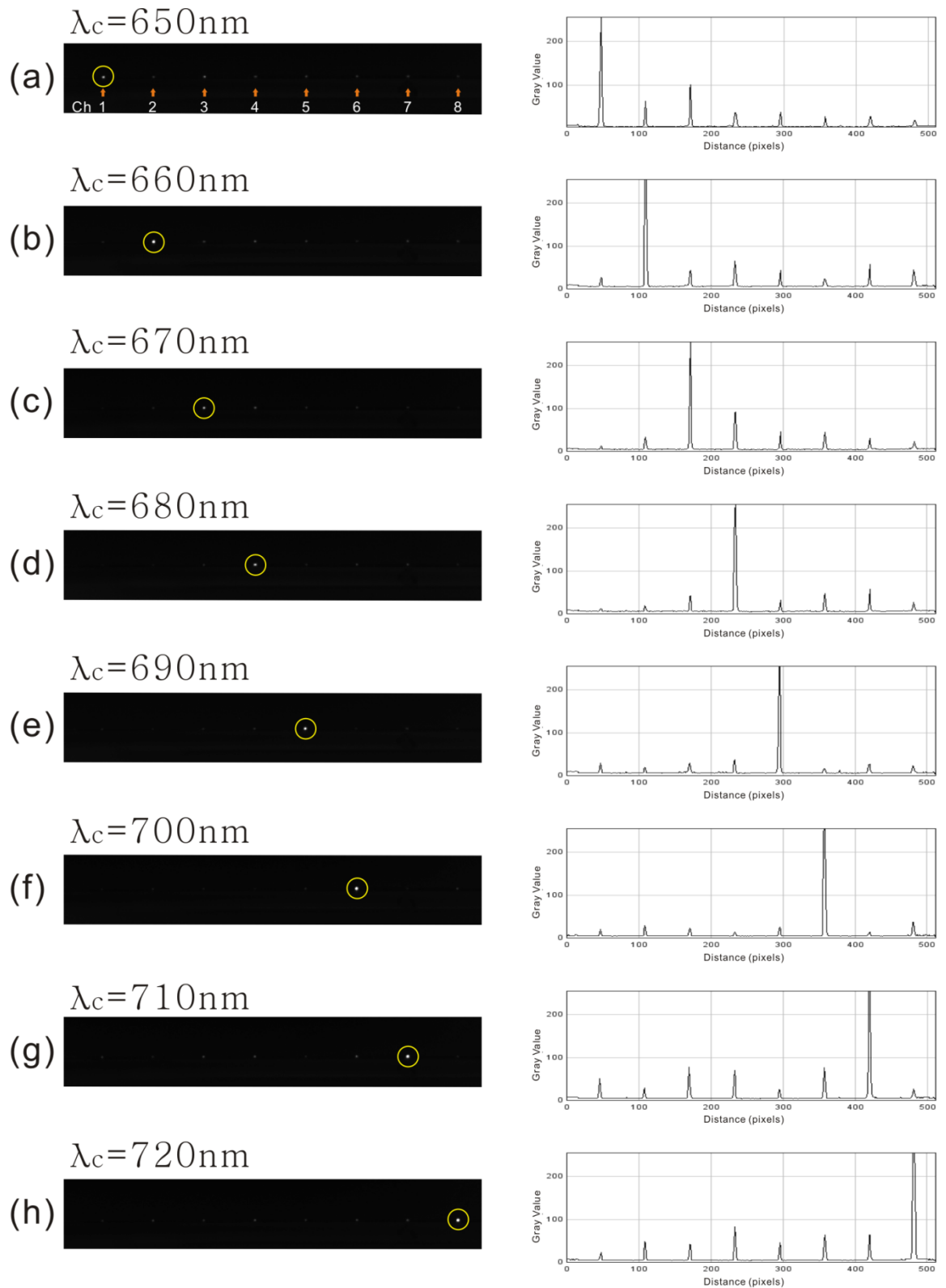


Figure 4.9 Characterisation results of AWG-microfluidic system using the CCD-based method. On the left side: CCD images of output signals from 8 output channels corresponding to narrow-band light of different centre wavelengths. On the right side: plots of the intensity profile along a horizontal line that connects the light spots of the output channels in the CCD images.

4.2 Evaluation of fluorescence measurements

4.2.1 Multiplexing fluorescence measurements with quantum dots

As indicated in Chapter 1, Quantum dots are widely used as fluorescence probes due to their narrow emission bandwidth and long-term photostability [142] as well as their suitability for surface functionalisation [232]. Importantly, several quantum dots can be excited using a single light source, making them good probes for simultaneous detection of multiple analytes. Due to the narrow bandwidth of a quantum dot's emission, emissions from multiple quantum dots are well suited to be detected simultaneously from the individually addressable output channels of the AWG device.

To evaluate this proposal, two quantum dots, namely QD655 and QD705 were used. The emission from QD655 (655 nm) and QD705 (705 nm) falls into the wavelength range of AWG channels 1 and 6 respectively. As shown schematically in Figure 4.10, a solution made by mixing QD655 and QD705 and excited by a single light source could have their emission light collected and processed simultaneously by two separate output channels on the AWG device.

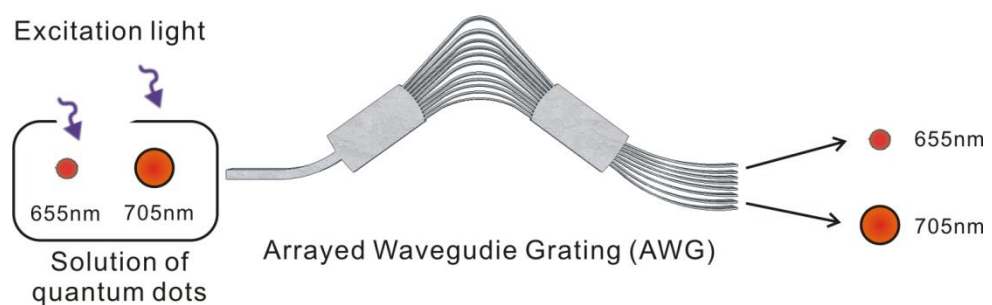


Figure 4.10 Experiment diagram for quantum dot measurements. Two different quantum dots (QD655 and QD705) were excited by a single light source and their emission light were collected and processed by the AWG device. Emissions from the two different quantum dots separate and exit from their corresponding output channels.

Figure 4.11 shows a more detailed layout of the quantum dots experiment in which the AWG device is mounted on a modified upright microscope stage. A 2 μm deep, 100 μm \times 100 μm sample cuvette was fabricated across the AWG input waveguide, into which the

quantum dot solution could be placed; this ensured efficient coupling of the fluorescent light into the AWG. A filter set (Exciter: 330-380 nm, bandpass; Dichroic: 400 nm, longpass; Emitter: 420 nm, longpass.) was used to obtain the blue excitation light from the mercury lamp installed on the microscope, and a $\times 50$ objective lens was used to focus this excitation light onto the cuvette area. Quantum dot QD655 and QD705 solutions were purchased from Invitrogen, and used as received. To minimise the amount of material used, 2 μL of a quantum dot solution was dropped in the cuvette of the AWG device and then covered with a thin glass cover slip to prevent water evaporation. For the purpose of evaluating the AWG's spectroscopic performance only, the spectra from each output channel on the AWG device were characterised by fibre coupling individual output waveguides to the entrance slit of a conventional spectrometer (TRIA320), as described in section 4.1.

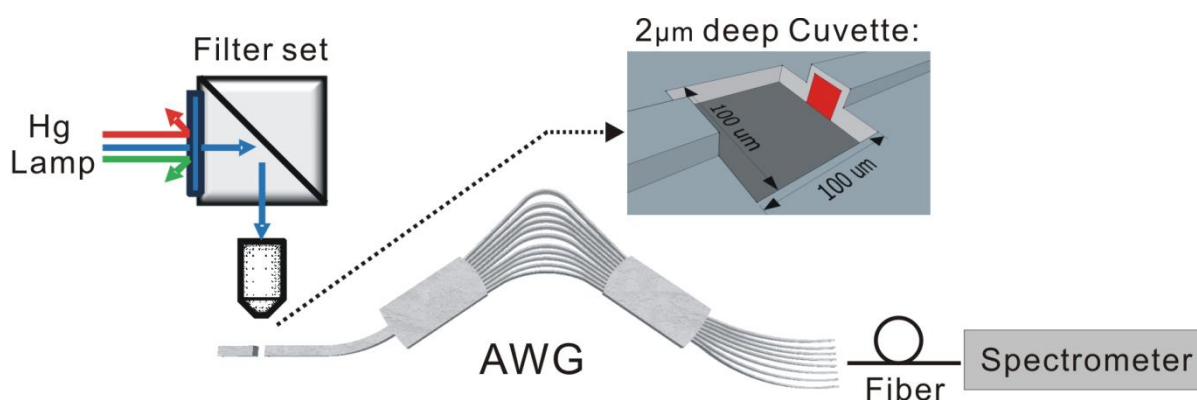


Figure 4.11 Illustration of quantum dot experiment setup. The experiment was performed by mounting the AWG device on a modified upright microscope stage. There was a fabricated sample cuvette (100 μm wide, 100 μm long and 2 μm deep) across the AWG input waveguide. The quantum dot solution filled in the sample cuvette was excited by a $\times 50$ focused blue light source which was realised by allowing the mercury lamp light to pass through an appropriate filter set. Light from the AWG output channels were coupled into a conventional spectrometer (TRIA320) for characterisation. Inset image indicated by the dashed arrow: illustration of the sample cuvette.

Results and discussion

Emission spectra from three different solutions: (a) QD655 only, (b) QD705 only and (c) a mixture of QD655 and QD705 were measured from each of the output channels. Spectra measured off chip from the same solutions were also collected to use as references in order to verify the performance of the AWG.

As shown in Figure 4.12a & b, the signal from QD655 was only detected in channel 1 while that from QD705 only appeared in channel 6. This indicates minimal cross talk between the channels. Importantly, the single peak spectra from both channels are in excellent agreement with their reference spectra obtained off chip (the black curves in Figure 4.15a & b). For a mixture of QD655 and QD705, signals from both channels 1 and 6 were detected (Figure 4.12c). However, as the spectroscopic measurement of these signals showed, the light emitted from these channels consisted of only a single peak corresponding to the individual QD655 or QD705 fluorophores (channel 1 and 6 respectively, Figure 4.12c); c.f. the low crosstalk seen in Figures 4.9a and 4.9f. Adding the spectroscopic outputs from these channels together gives an envelope that compares well with the double peak spectrum obtained from an off-chip, bulk solution, measurement using a conventional spectrometer. This demonstrates the effective capability of the AWG device in the discrimination of wavelengths and opens up the possibility of assaying a sample containing multiple targets.

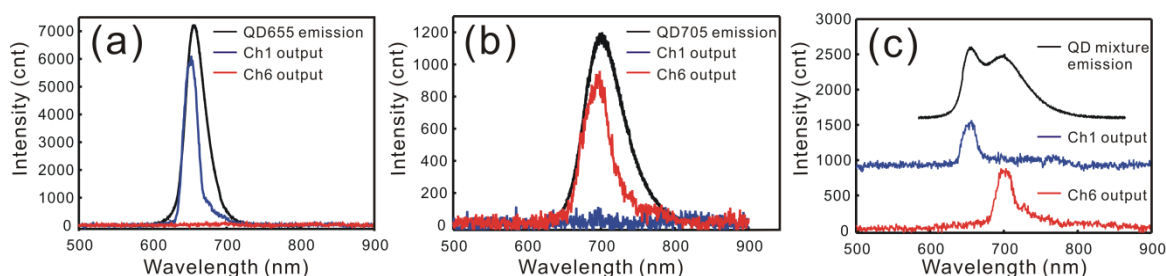


Figure 4.12 Multiplexed measurement of quantum dots using the AWG device. Spectra of quantum dots in red and blue were obtained from the representative AWG output channel (1 and 6) while those in black were the corresponding references obtained via off chip measurement. Three solutions were used: (a) QD655 only, (b) QD705 only and (c) a mixture of QD655 and QD705.

It should be noted that a blue ray laser diode could be utilised for the excitation light and it offers significant advantages over the bulky mercury lamp due to its compact size and potential capability for monolithic integration. The use of a blue ray laser diode will be described in Chapter 5.

Detection limit

The detection limit of an analytical measurement is regarded as being the lowest concentration of the analyte that can be distinguished with reasonable confidence from a background, which defined as a sample solution containing zero concentration of the analyte. Generally, the detection limit is estimated from the mean of the background measures, the standard deviation of the background measures and 3 as the confidence factor, which can be seen clearly from the equation below [233]:

$$x_L = \tilde{x}_B + 3s_B$$

\tilde{x}_B is the mean of the background measures, s_B is the standard deviation of the background measures, and x_L is the smallest measure of response that can be detected. Therefore, the detection limit in terms of concentration is given by [233]:

$$c_L = \frac{3s_B}{S}$$

S is the sensitivity of the measuring method and c_L is the detection limit in terms of concentration.

It should be noted that both the definition and the estimation of detection limit are statistical matters related to the random errors which require a considerable number of experimental measurements in which both the same solutions would be measured many times, and each solution of a nominal composition would be made-up many times. However, the work in this thesis is targeted to conceptually prove the feasibility and reliability of the AWG-microfluidic platform rather than search for the absolute detection limit for one individual assay, or set of measurements. Consequently, whilst the error in the value of the optical signal for each measurement will be low (as a consequence of the large number of counts detected, or long integration times), it would be misleading to use this low error to estimate the limit of detection of a particular assay.

4.2.2 Cy5 spectroscopic fluorescence measurements

4.2.2.1 Measurement with AWG and spectrometer

As described in the introduction, the ability to measure the spectroscopic envelope of fluorescence emission greatly increases the number of areas in which fluorescence analysis can be used. Thus, to demonstrate the AWG's performance in this area, a Cy5 fluorescence measurement was performed with an AWG-microfluidic platform. The experimental configuration used either a coupled spectrophotometer, as in Figure 4.13 (for initial validation experiment), or a CCD (section 4.5). Various Cy5 solutions were delivered into the microfluidic channel at a flow rate of 6.7 mm/s and the fluorophores passing the cuvette area were excited by 632.8 nm laser light coming from the 45° intercepted waveguide (E-WG). The light signals from each AWG output channel were fibre coupled into the conventional spectrometer for investigation of both wavelength and intensity.

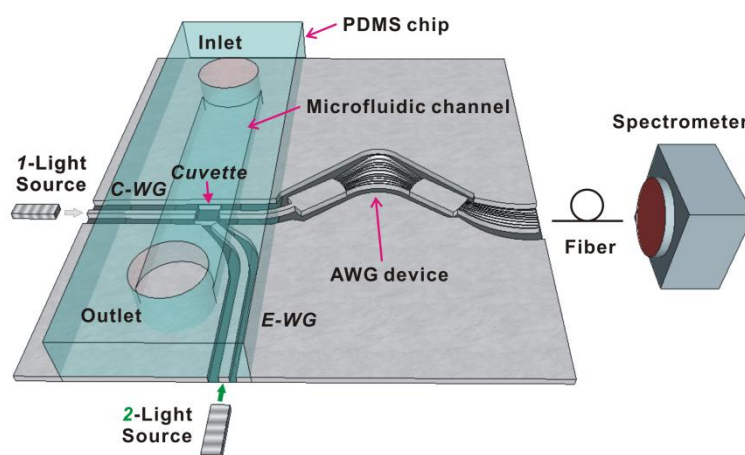


Figure 4.13 Illustration of Cy5 fluorescence measurement with the AWG-microfluidic platform and a conventional spectrometer. Cy5 solution was flowing in the microfluidic channel and the fluorophore passing cuvette area was excited by 632.8 nm laser light coming from the 45° intercepted waveguide (E-WG). The optical signals from each AWG output channel were fibre coupled into a conventional spectrometer (TRIA320) for wavelength and intensity investigation.

Preliminary results

The spectrum from each output channel was shown in Figure 4.14. It is clear that, taken together, the peak intensities of the spectra collected from each of the 8 channels follow the envelope of the reference Cy5 emission spectrum. Low crosstalk was observed between

spectra from each output channel, demonstrating again good fidelity of spectroscopic measurements by the AWG-microfluidic platform.

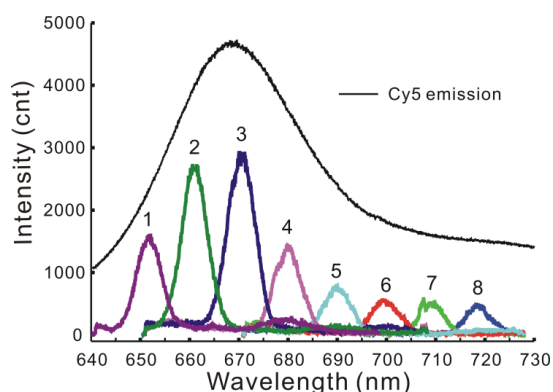


Figure 4.14 Cy5 fluorescence measurement result with the AWG-microfluidic platform and a conventional spectrometer. The comparison between different wavelength peaks (colour lines) from the 8 output channels (indicated by the digit numbers) and the reference Cy5 emission spectrum (the black line) is shown.

For use in a diagnostic assay, if different concentrations of Cy5 solution were tested, the output spectra should reflect corresponding changes in the fluorescence intensity. Thus, in this work, four different concentrations ($1\ \mu\text{M}$, $10\ \mu\text{M}$, $20\ \mu\text{M}$ and $85\ \mu\text{M}$) of Cy5 solution, and deionised (DI) water were measured with the AWG-microfluidic platform in conjunction with a conventional spectrometer. The output channel 3 was selected to demonstrate the quantitative study since it corresponds to the maximum wavelength (670 nm) of Cy5 emission spectrum. As shown in Figure 4.15, the spectral intensity increased with the concentration. However, only a representative group of measurement results were recorded so that the detection limit could not be derived from the limited data. As shown later, in experiments in which the AWG output is collected by a CCD, measurements such as these provide the basis for constructing a calibration curve.

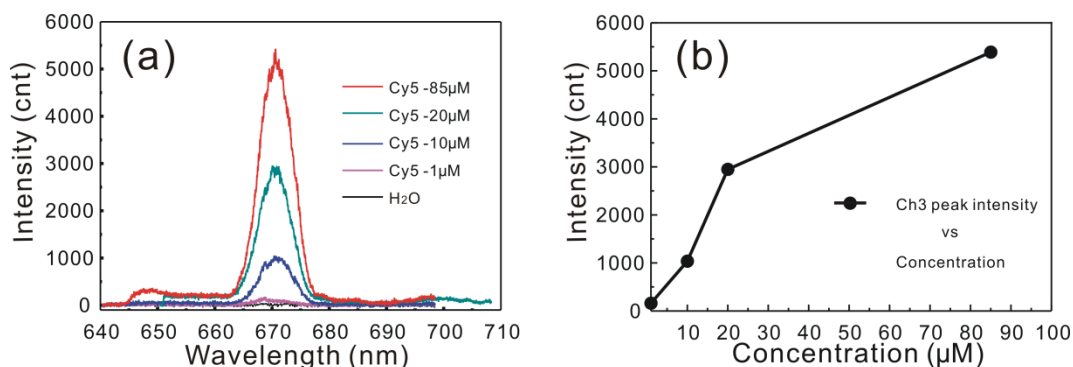


Figure 4.15 (a) Spectroscopic signals from AWG output Channel 3 (670 nm) with different concentrations of Cy5 solution. (b) the relationship between Ch3 peak intensity and Cy5 solution concentration. Four different concentrations ($1\ \mu\text{M}$, $10\ \mu\text{M}$, $20\ \mu\text{M}$ and $85\ \mu\text{M}$) were tested comparing with deionized (DI) water.

4.2.2.2 Measurement with AWG and CCD

Following on from the Cy5-AWG characterisation experiments of section 4.4, with an understanding of and confidence in the output spectra from individual channels, a CCD camera was then employed to detect the light intensities from the output channels simultaneously. Figure 4.16a illustrates integration of the AWG device with microfluidics and CCD camera. A 45° mirror and a $\times 4$ objective lens were used to reflect AWG output signals onto a vertically mounted CCD camera. A 2 μm deep sample cuvette with planar dimension of 50 μm by 50 μm was fabricated by dry etching as shown Figure 4.16b.

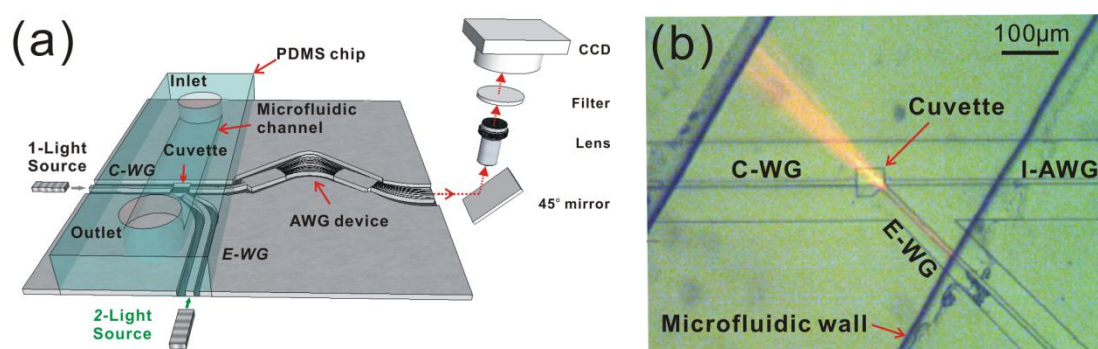


Figure 4.16 Illustration of Cy5 fluorescence measurement with the AWG-microfluidic platform and a CCD detector. (a) Schematic illustration of integration of AWG device with microfluidics and CCD. A 45° mirror and a $\times 4$ objective lens were used to reflect AWG output signals onto a vertically mounted CCD detector. (b) A close up view of the monolithic integrated AWG-PDMS microfluidic chip, where the sampling cuvette is located in the middle of the microfluidic channel. The red flare starting in the cuvette area and going diagonally towards the top left of the microfluidic channel shows the path of light emanating from the excitation waveguide. C-WG: white light characterisation waveguide. E-WG: excitation waveguide. I-AWG: AWG input waveguide.

Figure 4.17 provides pictures of the experimental setup for Cy5 fluorescence measurement with the AWG-microfluidic platform and a CCD detector. As shown in the left half of Figure 4.17, the experimental setup was built around an upright microscope (Nikon Microphot SA) with a modified stage. The AWG-microfluidic platform was mounted on a sample holder which was positioned in the centre of the modified microscope stage. External light sources, including broad band white light and narrow band excitation laser, were fibre coupled into the AWG device. Two V-groove fibre holders were attached respectively to two different 3-axis micropositioners (Line Tool Company) which were fixed on the modified microscope stage. A CCD camera (Andor 885 iXon) was mounted

vertically onto the microscope. A 45° mirror (made by depositing 75 nm NiCr on a silicon wafer) and a ×4 objective lens were used to reflect AWG output signals onto the CCD detector. Sample solutions were delivered into the microfluidic channel of the PDMS chip by using PTFE tubings, a plastic syringe and a pumping unit. Various flow rates could be obtained by adjusting the pump control.

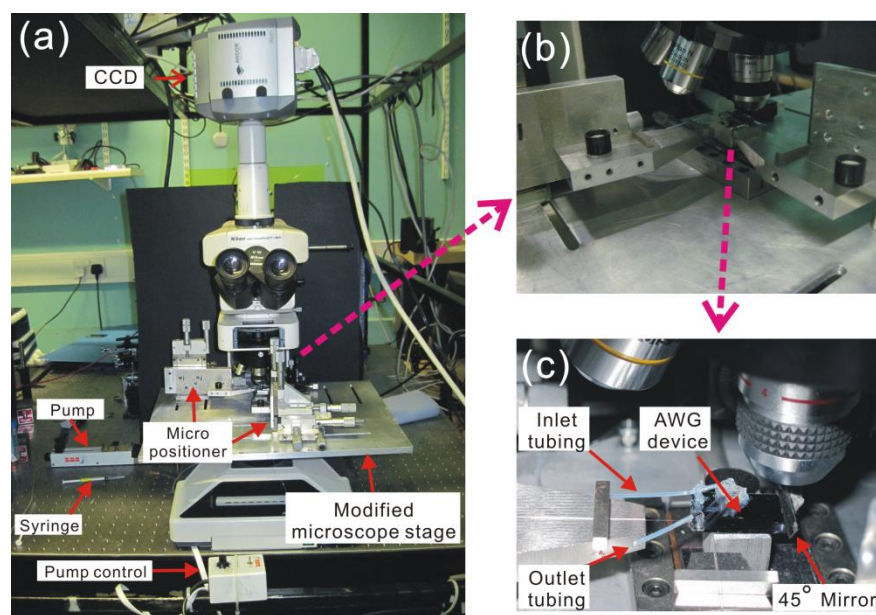


Figure 4.17 Pictures of real experiment setup for Cy5 fluorescence measurement. (a) Picture of the complete experiment setup. (b) A close view of the modified microscope stage. (c) A close view of the AWG-microfluidic platform. The whole experiment setup was using an upright Nikon microscope (Microphot SA) by modifying its stage. The AWG-microfluidic platform was mounted on a sample holder which was positioned in the centre of the modified microscope stage. External light sources, including broad band white light and narrow band excitation laser, were fibre coupled into the AWG device. Two V-groove fibre holders were attached respectively to two different 3-axis micropositioners (Line Tool Company) which were fixed on the modified microscope stage. A CCD camera (Andor 885 iXon) was mounted vertically onto the microscope. A 45° mirror (made by depositing 75 nm NiCr on silicon wafer) and a ×4 objective lens were used to reflect AWG output signals onto the CCD detector. Sample solutions were delivered into the microfluidic channel of the PDMS chip by using PTFE tubings, a plastic syringe and a pumping unit. Various flow rates could be obtained by adjust the pump control.

Qualitative and quantitative results

Figure 4.18 (i) shows a CCD image of the output from the 8 channels using a 1 μM Cy5 solution. The 8 bright spots correspond to the 8 output channels (Figure 4.18 (ii)). Plotting the intensities from the 8 spots versus their centre wavelengths (Figure 4.18 (iii)) clearly replicates the envelope of the Cy5 emission spectrum. Thus, the AWG device in conjunction with an imaging camera can provide a facile way to achieve a spectroscopic measurement.

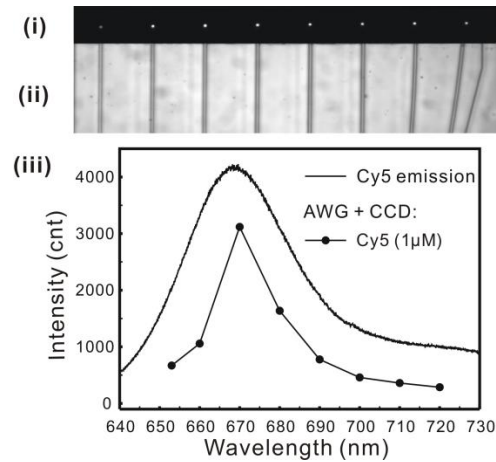


Figure 4.18 Result of Cy5 fluorescence measurement with the AWG-microfluidic platform and a CCD detector. (i) CCD image of the output from Cy5 emission, channels from left to right are channel 1 to channel 8. (ii) top-down bright field image of the output waveguides. (iii) The intensities of the CCD images from the output in comparison to a Cy5 emission spectrum. A 633 nm notch filter and a 650 nm long pass filter were used to remove all the excitation light from the signal.

Importantly, an increase of Cy5 concentrations resulted in a proportional increase in intensity on the CCD. This linear relationship is illustrated in Figure 4.19 where the intensity in the CCD image of an area corresponding to the output from a single example channel, channel 3, is integrated. Extensive efforts were not made to determine a limit of detection for Cy5 fluorescence; however, the results obtained suggest this would be significantly lower than the 100 nM measured (note the LOD would depend on the assay time and the excitation intensity). It should be noted that the linear relationship between the fluorescence intensity and concentration is only correct for very diluted Cy5 solutions (i.e. concentration < 2.0 μM in Figure 4.19). When the sample concentration increases, saturation effect starts to occur. Overall, the spectral resolution and linearity of the fluorescence-concentration plot demonstrate that the device is suitable for quantitative as well as qualitative (e.g. quantum dot) fluorescence measurements. These capabilities offer new avenues for assays that involve detecting both intensity and shape of spectra, such as a propidium iodide (PI)-DNA assay (see following section).

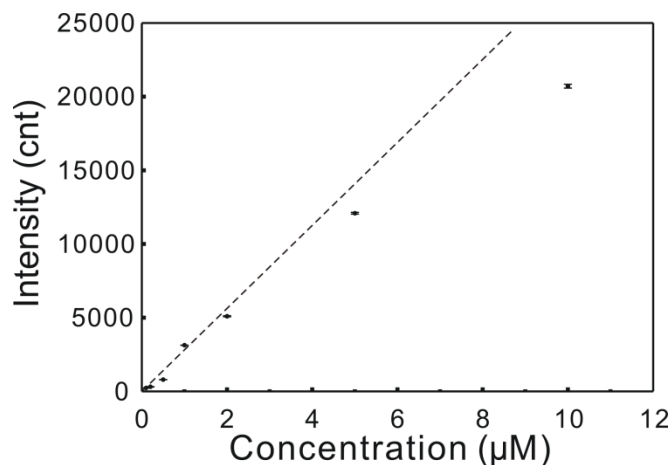


Figure 4.19 Graph of output channel 3 signal intensity with error bars and regression line for measuring different concentrations of Cy5 solution with AWG-microfluidic platform and CCD detector. Output channel 3 was selected as the example channel since it corresponded to the maximum wavelength (670 nm) of Cy5 emission spectrum. 3 or 4 measurements were performed for each concentration (0.1 μM , 0.2 μM , 0.5 μM , 1.0 μM , 2.0 μM , 5.0 μM and 10 μM). The error bars were made by using maximum, average and minimum values for each group of the measurement results and the deviations were within the range of $\pm 6\%$.

4.2.3 Assay based on spectroscopic analysis

4.2.3.1 Measurements with a conventional spectrometer

As described in the introduction, the shift in wavelength of propidium iodide (PI) fluorescence when it intercalates into DNA makes it a candidate for investigating whether the AWG device can be used to measure wavelength shifts in fluorescence. However, as can be seen in Figure 4.20, the emission from PI spans a large wavelength range. As discussed below, this imposes the complication in using the simple AWG device fabricated here.

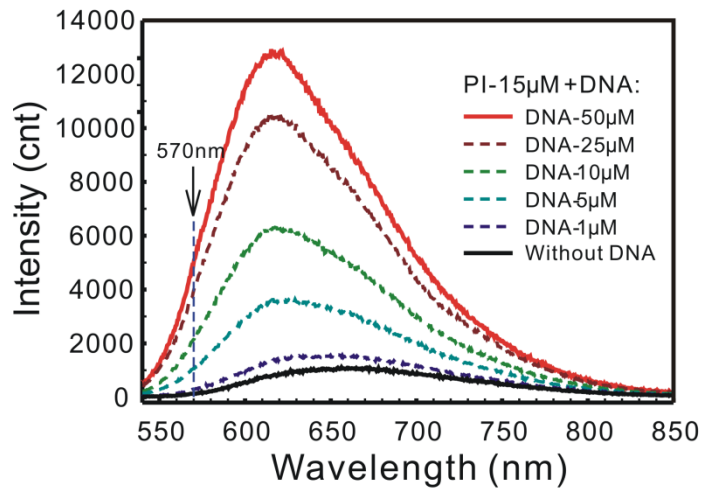


Figure 4.20 Fluorescence spectra of PI solutions with and without DNA (obtained off chip).

Propidium iodide (PI) and salmon sperm DNA were purchased from Sigma-Aldrich and made into aqueous solutions using deionised water (pH7, Millipore).

The 15 μM PI solution was made by diluting the 1 mg/mL stock solution (1500 μM) with deionised water. The PI and DNA solutions were prepared with a fixed PI concentration (15 μM) and various DNA concentrations including 0, 0.5 μM , 1.0 μM , 2.5 μM , 5 μM , 10 μM , 25 μM and 50 μM . All the sample solutions were left in room temperature for 3 hours before test.

4.2.3.2 Using AWG device with a different diffraction order

Similar to a conventional diffraction grating, an AWG device generally has more than one order which can be used for light dispersion. Figure 4.21 shows the transmission spectrum for two diffraction orders ($m=7$ and $m=8$). The disadvantage of this periodical performance when measuring broad band light source is that two or more wavelength peaks will exit from the same output channel of an AWG device (e.g. in Figure 4.21a and Figure 4.21b, 570 nm and 650 nm wavelength peaks both coming out from Ch1). This degrades or even ruins the AWG device's capability for wavelength resolving, especially when a wavelength insensitive photon detector is integrated. This problem could be completely tackled by an order-sorting filter or cascade of AWGs, however, fabrication of these was beyond the scope of the work in this thesis. For example, by using specific order-sorting filters (i.e. a bandpass filter or a combination of a long-pass and a low-pass

filter.), the light to be investigated can be pre-filtered and restrained to an effective wavelength range (i.e. FSR in Chapter 2) which the AWG device can then distinguish.

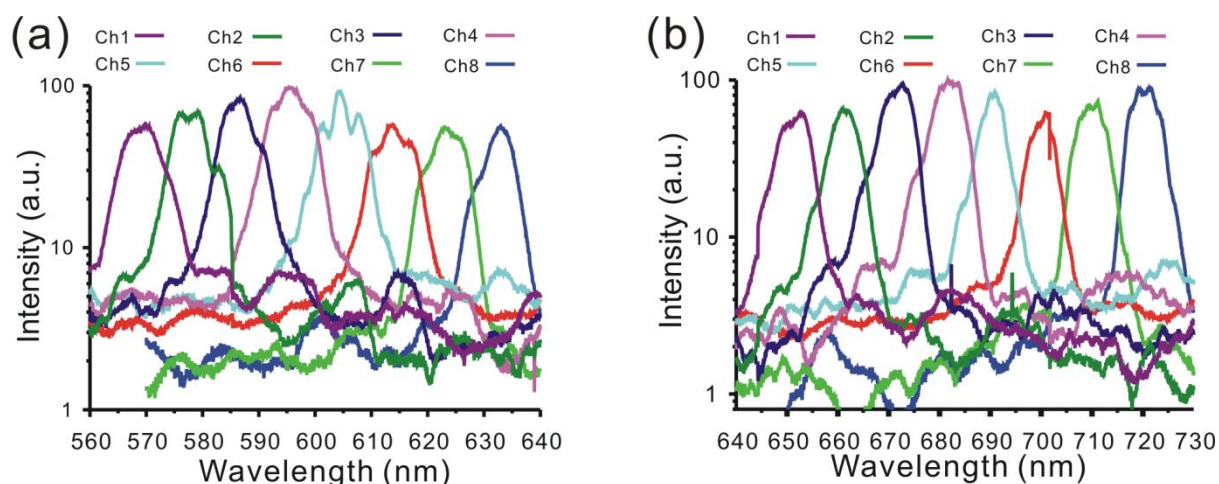


Figure 4.21 Normalized transmission spectral response of the AWG device for two different diffraction orders. (a) $m = 8$; (b) $m = 7$.

However, by understanding the periodical property of the AWG device, we can still use the AWG-microfluidic platform to investigate the peak shift and intensity enhancement of fluorescence spectra from PI and DNA solutions. By comparing the spectra of Figure 4.20 and Figure 4.21, the peak wavelength (617 nm) of the fluorescence spectrum for a PI+50 μ M DNA solution occurs in channel 6 output spectrum while maximum for unbound PI emission (654 nm) is out of the transmission window for order $m = 8$. Therefore, by using the AWG-microfluidic-CCD platform for fluorescence detection, a spectral peak occurrence as well as intensity enhancement was expected if the CCD detection window was limited to below 650 nm.

4.2.3.3 Measurement results with AWG and CCD

Various PI-DNA solutions were measured using the AWG-microfluidic device, interfaced to a CCD camera. For the PI-DNA assay, a range of concentrations were delivered into the microfluidic chip at a flow rate of 6.7 mm/s. Between measurements on two different solutions the channel was flushed with 500 μ L deionised water. A solid state 532 nm laser was used for the PI-DNA assay. To remove the scattered and stray light from the excitation light source, a combination of 550 nm long-pass and 650 nm short-pass filters was utilised.

Acquisition times on the CCD varied from 10 seconds to 5 minutes, depending on the strength of the fluorescence signal and the signal/readout noise ratio desired.

As illustrated in Figure 4.22a, when PI is bound to DNA, the fluorescence intensities from the different channels recorded on the CCD increase. It is also observed that for the unbound PI solution the greatest intensity is on channel 8 (633 nm), corresponding to the low wavelength side of the 654 nm peak seen in Figure 4.20. In contrast, when PI is bound to DNA, the greatest intensity in the CCD image is seen on channel 6 (614 nm) i.e. at the same wavelength range as the peak position of the corresponding PI-DNA spectrum in Figure 4.20. Thus the AWG response accurately reflects the shift in wavelength between the fluorescence spectra of PI and PI-DNA.

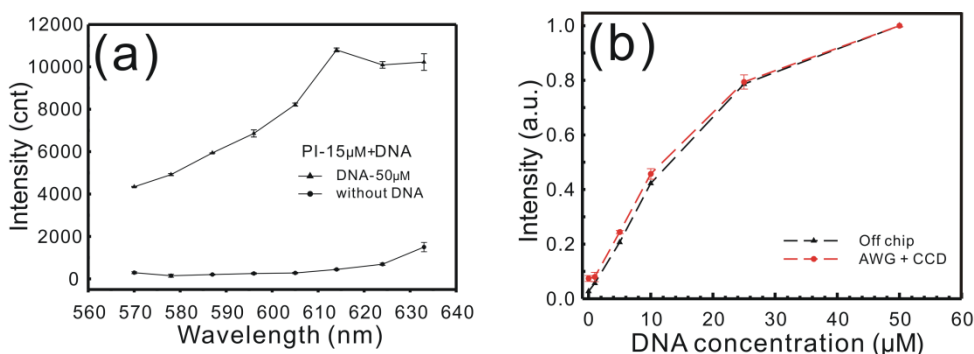


Figure 4.22 PI-DNA fluorescence measurement result with AWG-microfluidic-CCD system. (a) The intensity profile of the 8 outputs taken from the CCD images from for the PI solutions with and without DNA. (b) fluorescence intensity versus DNA concentrations plots comparing off chip spectrometer measurement (data taken from Figure 4.20 at 570 nm) and on chip measurement with a CCD detector (data taken from channel 1). The images were acquired for 5 minutes. Error bars indicate +/- one standard deviation.

In order to determine which channel has the greatest sensitivity for the detection of DNA bound to PI, the fluorescence intensity of bound PI was compared to that of unbound PI for each channel. It was found that the relative increase in intensity is greater at 570 nm (channel 1), compared to 614 nm (channel 6, where the absolute intensity is greatest). Thus, in Figure 4.22b, the intensity from channel 1 is plotted against DNA concentration and compared with the corresponding intensities measured at 570 nm using a conventional spectrometer. Both plots are in excellent agreement, again validating the functionality of the AWG device and demonstrating the utility of being able to subtly adjust or select the particular wavelength range used in quantifying an assay so as to optimise a signal to background (e.g. blank) measurement.

It is worth noting that such an imaging based approach measures intensity patterns of all the outputs simultaneously, and thus enables detailed analysis of individual channels. This can be advantageous for more demanding analysis, for example in FRET measurements and in quantitative ratiometric measurements, where variations at two or three wavelengths occur simultaneously.

4.3 Summary

In the first section of this chapter, the integrated AWG-microfluidic platform was optically characterised with two different methods. The first one was using a white light source and a conventional spectrophotometer while the latter employed a monochromatic light source and a CCD camera. With the white light source, the acquired spectra from all the output channels of the AWG device validated light dispersive capability of the AWG device. With the monochromatic light source, however, the CCD-based characterisation method is compatible with the ultimate experimental configuration using the AWG-microfluidic system for the following fluorescence measurements.

Different fluorescence measurements were performed to evaluate the AWG-microfluidic system. Firstly, fluorescence from mixed quantum dot solutions was detected with the AWG device. The quantum dot fluorescence experiment results have demonstrated the effective capability of the AWG device in the discrimination of wavelengths and opened up the possibility of assaying a sample containing multiple targets. Then an organic fluorophore (Cy5) was measured with the AWG+CCD system in a microfluidic format and the Cy5 fluorescence spectrum envelope was successfully re-created by analyzing the signals from the CCD camera. Furthermore, spectroscopic shifts were detected with the AWG device by measuring the propidium iodide (PI)-DNA assay. Quantitative as well as qualitative experimental results have conceptually proved the capabilities of the AWG platform for simultaneous, multiplex detection and spectroscopic measurements.

5. Chapter 5

Localised spectroscopic measurements

Abstract

This chapter describes an adapted AWG design with focusing properties and localised spectroscopic measurements that can be used to extend the applications using AWG-microfluidic platform to other fields such as flow cytometry and single cell analysis. Lens curvatures were incorporated into the ends of the integrated waveguides (E-WG and I-AWG) and the controllable focusing properties were evaluated by fluorescence measurements. Subsequently, localised quantum dots fluorescence detection with excitation from a blue ray laser diode was attempted. Following this, micro-bead based, localised spectroscopic measurements were performed with the AWG+CCD platform. These results demonstrate the potential capabilities of using the modified AWG device for continuous and multiplexed fluorescence detections that require high sensitivity and spatial resolution.

5.1 Introduction

As discussed in the introduction chapter, by devising methods to probe small volumes in an AWG-microfluidic device, applications in the fields of flow cytometry, cell sorting, single cell analysis, and pathogen/antibody detection are opened up.

With the combination of planar waveguide technology and a spectroscopic capability, arrayed waveguide grating (AWG) devices provide a suitable platform for development of a miniaturised optical detection system for flow cytometry. As described in detail below, to exploit this potential, an AWG device with focusing facets on the excitation and input waveguides was designed and fabricated. With this device, localised detection of quantum dots and a micro bead-based fluorescence assay were performed to prove the concept. Although the final stages of complex microfluidic integration have not been completed as

yet, elsewhere in this thesis details are given to show how a microchannel superstructure could be integrated with the established AWG platform, thereby realising a fully functionalised micro flow cytometer.

5.2 Results and Discussion

5.2.1 Adapted AWG devices for localised detection

5.2.1.1 AWG device with focusing waveguides

As shown in Figure 5.1a, conventional fluorescence-activated flow cytometers generally employ a lens-aided optical detection system. The laser excitation beam is focused through a lens onto the component passing by the interrogation point. Then the induced scattering or fluorescence signals are collected by another lens and focused onto the photodetector via a selection of filter sets. The basic principle for an integrated optical detection system is not unlike that of conventional flow cytometry. With lens curvature at the end of integrated waveguide, a focusing excitation and a highly localised collection could be realized. This is illustrated in Figure 5.1b which shows the optical detection unit from an AWG device without (i) and with (ii) lens at the end of the integrated planar waveguides.

It is commonly believed that, lensing is highly desirable, especially in cases where sensitivity is decreased due to the small size and volume of samples. Focusing light down to a small spot can increase fluorescence emission, and likewise collecting light from a highly localised area can greatly reduce unwanted signals from light scattered by other features/objects inside the sample cell. However, it is worth noting that the 2D lenses of current design shown in Figure 5.1b only focus light in the horizontal plane. Whilst implementation of 3D lenses is possible, the complexity of fabrication process will be increased significantly and has not been attempted in this work.

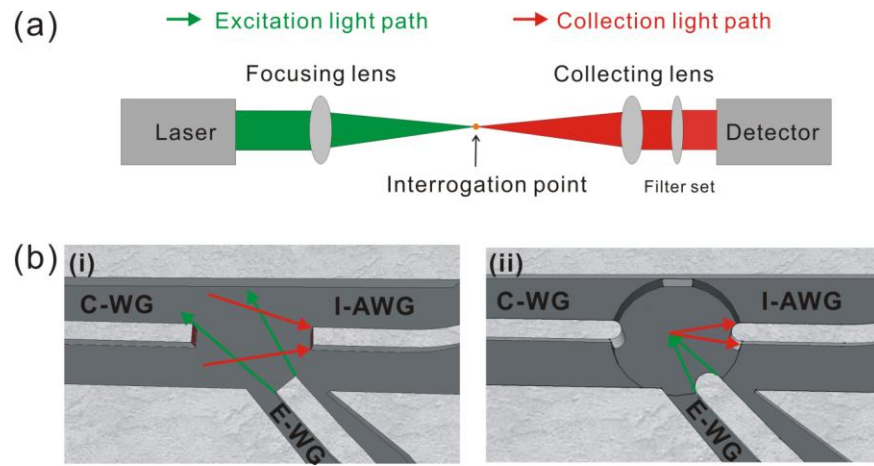


Figure 5.1 Schematic diagrams of optical detection system with conventional free-standing and integrated optics. (a) conventional optical detection system with the aid of lens. A laser excitation beam is focused by a lens onto the interrogation point and another lens is utilised to collect signals such as fluorescence onto the detector. A filter set needs to be employed if fluorescence detection is used. (b) optical detection system from the AWG design consisting of integrated waveguides with (i) flat end, or (ii) lens curvature. C-WG: white light characterisation waveguide; E-WG: excitation waveguide; I-AWG: input waveguide of the AWG device. The lenses at the end of integrated waveguides could enable a focusing excitation and localised collection while flat-end integrated waveguide would experience divergent light paths.

5.2.1.2 Evaluation of the focusing waveguides

Based on the previous AWG design, a 2D lens with radius of 4 μm was designed at the end of the three integrated waveguides which are intercepted by the sampling cuvette. The three identical lenses share the same focal point which is located in the centre of the cuvette with radius of 25 μm . The design of the curvature and spacing apart of the end facets take into account the refractive indexes of the waveguides and the aqueous sample solution that would be used according to the formula, $\frac{1}{f} = (n_{WG} - n_{H_2O}) \frac{1}{R}$, in which f is the focal length, R is the radius of the lens curvature, n_{WG} and n_{H_2O} are the refractive indexes of the waveguide material and water respectively. As shown in Figure 5.2, a PDMS microfluidic chip was bonded with the AWG device and the sampling cuvette was arranged in the middle of the microfluidic channel.

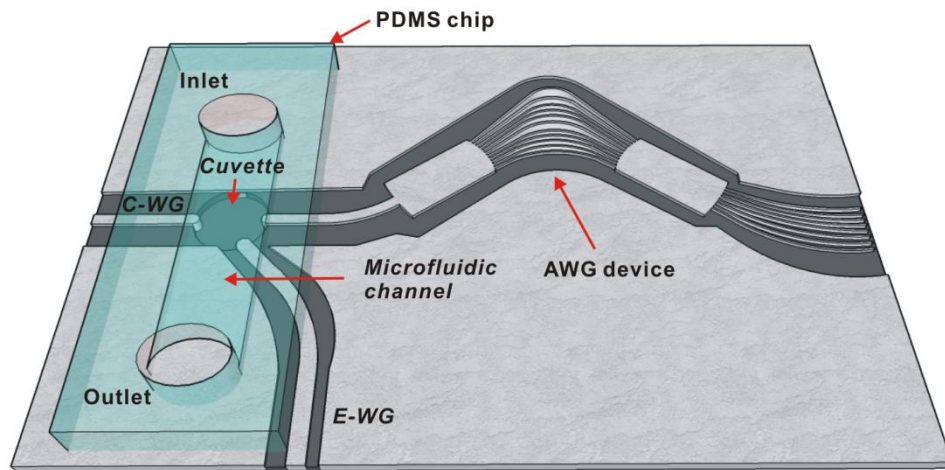


Figure 5.2 Schematic of microfluidic incorporation onto the AWG device with focusing waveguides. The sampling cuvette is located in the middle of the microfluidic channel. And the end faces are designed with lens curvature for the three integrated waveguides which are intercepted by the cuvette. C-WG: white light characterisation waveguide, E-WG: excitation waveguide.

To evaluate focusing capabilities of the waveguides incorporating end facet lenses, a fluorescent dye solution (10 μM Cy5) was delivered into the microfluidic channel at a flow rate of 6.7 mm/s. Laser light (632.8 nm) was introduced into the cuvette area through each of the three intercepting waveguides to illuminate region by each of the waveguide. The field view of the AWG input guide was visualised by injecting the laser light (632.8 nm) into the appropriate output waveguide (i.e. Ch8) so that the laser light traversed the slab regions of the AWG device and exited from the AWG input waveguide. With illumination of the laser light, the fluorescent dye molecules passing by the cuvette area would be excited and produce longer-wavelength emission signals. The focusing properties of the lens-aided waveguides were visually evaluated by acquiring fluorescence images of the cuvette area using an upright fluorescence microscope and a Cy5 filter cube.

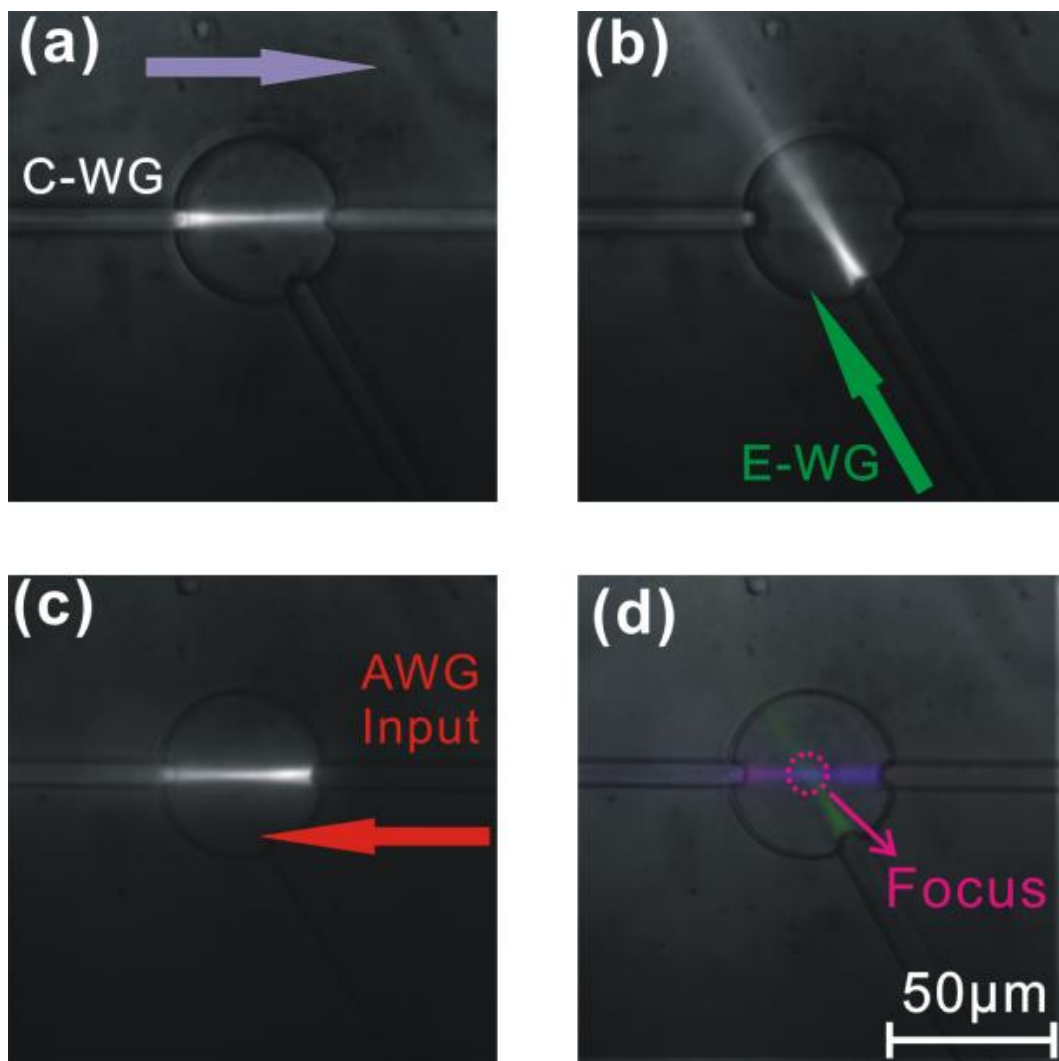


Figure 5.3 Fluorescence microscopic images of the optical detection system with focusing integrated waveguides. A fluorescent dye solution (Cy5) was delivered into the microfluidic channel and a laser excitation light (632.8 nm laser) was introduced into different integrated waveguides: (a) C_WG; (b) E_WG; (c) AWG input waveguide. By filtering the excitation light, the fluorescence microscopic images of the cuvette area were acquired respectively and (d) is their composite image by using different colors for each light path. Differing from inherent divergent property of flat-end integrated waveguides, the lens-aided scheme offered focusing light paths which are consistent with the theoretical design. The arrows in figure (a) to (c) indicate the direction of laser excitation. In figure (d), the intersection area of the three light paths is highlighted with a pink dashed circle.

Figure 5.3a-c shows the respective fluorescence images when the laser excitation light comes from each of the three individual intercepted waveguides. In these pictures, the focusing effect can be seen clearly. Figure 5.3d is a composite image of the initial three by using different colors for labelling each light path. The intersection of the three light paths reveals the practical capability of this device to incorporate focusing waveguides into the optical detection system.

For comparison, an optical detection system without lensing was also designed and fabricated. With the same evaluation method, the resulting fluorescence images can be seen in Figure 5.4. It is quite clear that each of the light paths associated with the waveguides field of view are inherently divergent. These comparative results illustrate the advantage of lens-aided focusing capability for localised collection.

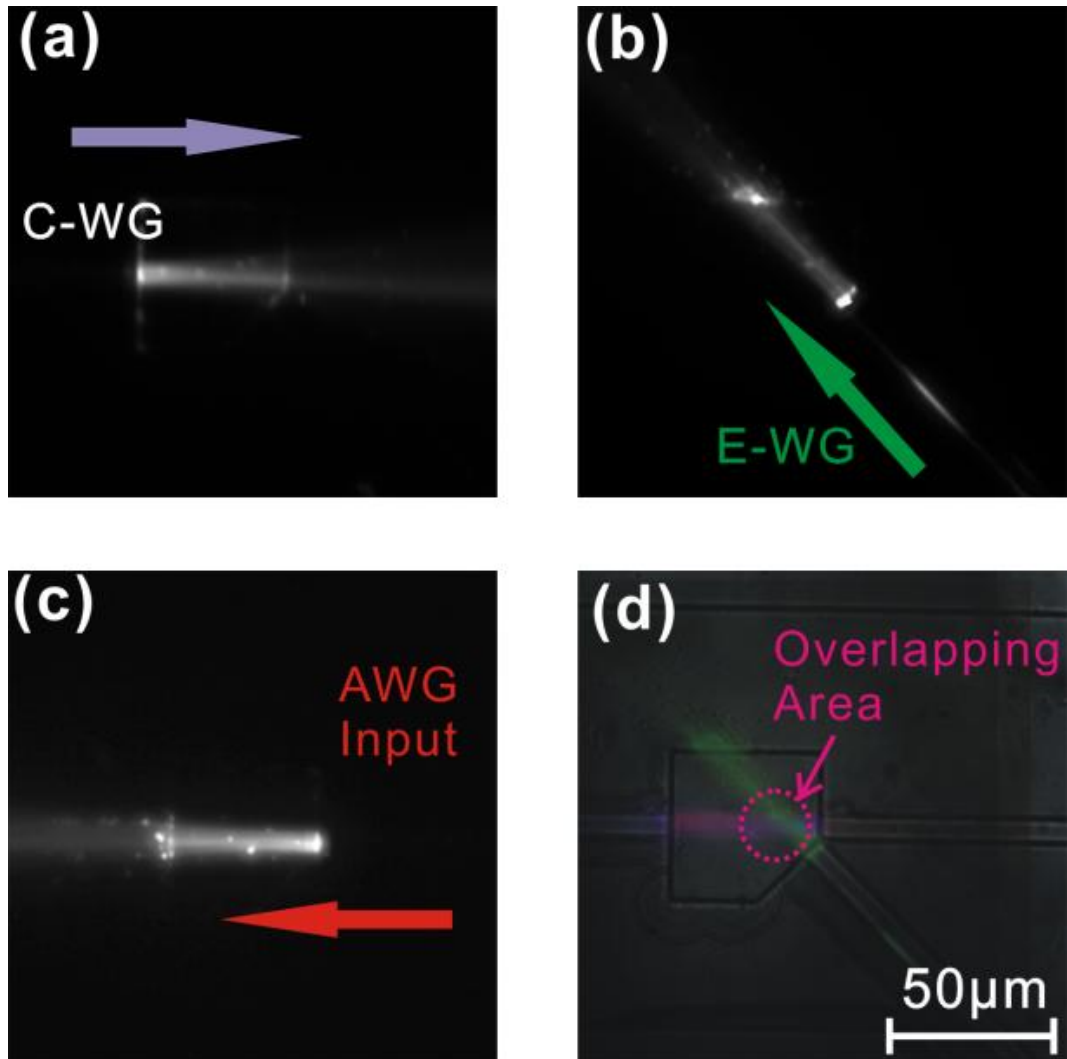


Figure 5.4 Fluorescence images of the optical detection system with flat-end waveguides. Compared to Figure 5.3, flat end faces instead of lens curvature were designed for the three intercepted waveguides. Likewise, three fluorescence images were acquired under the same experimental condition. Using the method, the composite image of the initial three is shown in (d). Without lensing, the inherent divergent light paths were shown clearly. The arrows in figure (a) to (c) indicate the direction of laser excitation. In figure (d), the intersection area of the three light paths is highlighted with a pink dashed circle.

5.2.2 Localised fluorescence detection

5.2.2.1 Detection of immobilised quantum dots

By using lensed integrated waveguides, attempts at demonstrating the localised detection capabilities of the visible AWG device were made using quantum dots that have been immobilised in the cuvette region (see details in the Experimental section). Before introducing the blue-violet laser light through the planar excitation waveguide (E-WG), the localised quantum dots pattern was investigated with a typical upright fluorescence microscopic configuration. A blue light, from a mercury lamp through a blue filter cube, was focused onto the sampling cuvette area with a $\times 50$ objective lens. Then the fluorescence image of the cuvette area was obtained with combination of an emission filter and a CCD camera. Figure 5.5 shows the fluorescence image and the central localised quantum dots pattern inside the cuvette is clearly displayed. The unexpected bright features around the periphery of this image, outside the cuvette are thought to be caused by the non-specific bonded quantum dots. However, more significant is the bright line along the curved lens end of the waveguide, which reveals a problematic accumulation of quantum dots there.

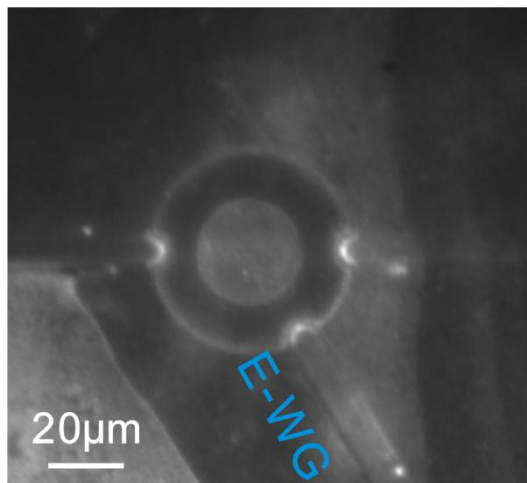


Figure 5.5 Fluorescence image of the localised quantum dot pattern. The sampling cuvette area is illuminated by above excitation light which is from the mercury lamp of the fluorescence microscope. The fluorescence image reveals the localised quantum dot pattern. The unexpected bright image outside the cuvette comes from non-specific bonded quantum dots and there is an accumulation of quantum dots at the end of the three integrated waveguides.

To exploit the potential of the AWG devices for portable applications, a small size blue-violet laser diode (DL-4146-101S from Sanyo, 405 nm, 20 mw maximum power) was utilised for the excitation and its experimental setup is shown in Figure 5.6. The laser diode

was mounted on a printed circuit board (PCB) which is wire connected with a laser driven circuit (bottom right inset image in Figure 5.6). A $\times 20$ objective lens was employed to couple the laser light into a single mode optical fibre of which the other end is connected with the excitation waveguide (E-WG) of the AWG device.

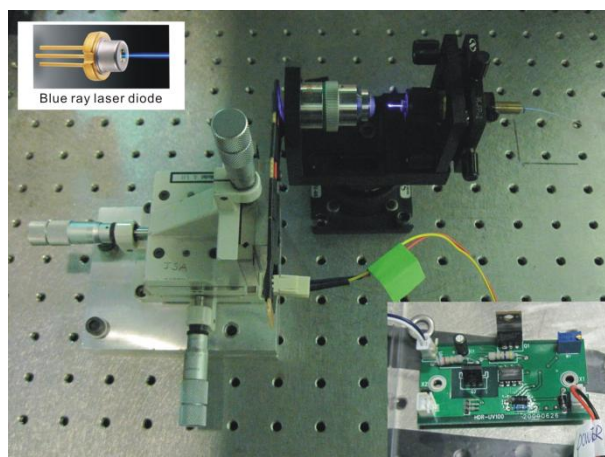


Figure 5.6 Experimental setup for blue-violet laser excitation. A blue-violet laser diode (DL-4146-101S from Sanyo, see top left inset image) is mounted onto a printed circuit board (PCB) which is connected with a driven circuit (bottom right inset image). The laser light is coupled by a $\times 20$ objective lens into a bare single mode optical fibre.

The fluorescent image of the quantum dots using side blue-violet laser excitation is shown in Figure 5.7. Due to the accumulation of quantum dots near the waveguide ends (Figure 5.5), there was a bright fluorescence area at the end of the excitation waveguide (E-WG). The red dashed circle indicates the localised quantum dots pattern while the outside grey dashed circle represents the cuvette border. The fluorescence light path reveals that only the near edge of the circular quantum dots pattern was strongly excited by the light from the integrated E-WG waveguide. The centre of the pattern was much darker (c.f. Figure 5.5). The probable reason for this effect is related to topographic or height differences between the quantum dots pattern and the excitation waveguide which is $2\ \mu\text{m}$ higher than the cuvette area. From this perspective, it is clear that a solid support with a similar height profile as the excitation waveguide would be desirable in order to obtain effective illumination from the planar excitation light. This can be realized by patterning functionalised beads of an appropriate size in the cuvette region, as described below.

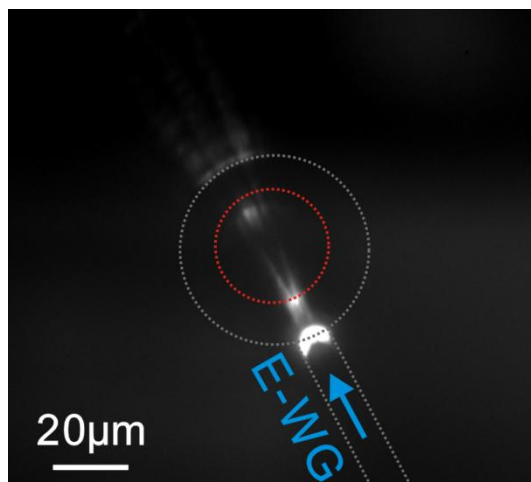


Figure 5.7 Fluorescence image of the localised quantum dot pattern with side blue-violet laser excitation. The blue-violet laser excitation light is introduced into the cuvette through the planar excitation waveguide (E-WG). The bright spot at the end of E-WG reveals an accumulation of quantum dots there. The red dashed circle indicates the localised quantum dots pattern while the outside grey dashed circle represents the cuvette border. Due to lower topography of the cuvette, only the nearby edge of inside quantum dots pattern is strongly illuminated by the excitation light.

5.2.2.2 Localised Micro-beads based fluorescence assay

To obtain effective illumination from the excitation light, 1 μm micro beads were used to provide a solid support for the fluorescent molecules so as to ‘lift’ the fluorescent centres into the field of view of the excitation and AWG-input waveguides. Among the many types of fluorescent microbeads available, those chosen (Flash Red) were available in a form with pre-conjugated streptavidin. This allowed different bio-functionalised quantum dots to be conjugated layer by layer and a multiplexed spectral bio-sensing assay to be performed with the AWG device and a CCD detector. Details of micro-beads immobilisation and the subsequent conjugation reactions are included in the Experimental Sections.

5.2.2.2.1 Fluorescence image of adsorbed micro beads

The fluorescence micro beads were produced by the manufacturer using an internal inorganic based dye loading process, which offered good resistance to photobleaching. As shown in Figure 5.8a, a laser light source (633 nm HeNe laser or 532 nm solid laser) was introduced to excite the fluorescence beads in the sampling cuvette through the planar excitation waveguide (E-WG). The fluorescence signal was collected by an objective lens ($\times 50$) above the sample and then detected by a CCD camera after passing through an emission filter. Figure 5.8b shows the fluorescence image of the sampling cuvette where

the micro beads were excited the laser source. To estimate the light paths, the physical borders of the sampling cuvette and the three integrated waveguides were marked with grey dashed lines. Although the brightest spot was not found in the centre of the sampling cuvette, it is reasonable to believe that the fluorescence signal can be partially collected by the AWG input waveguide.

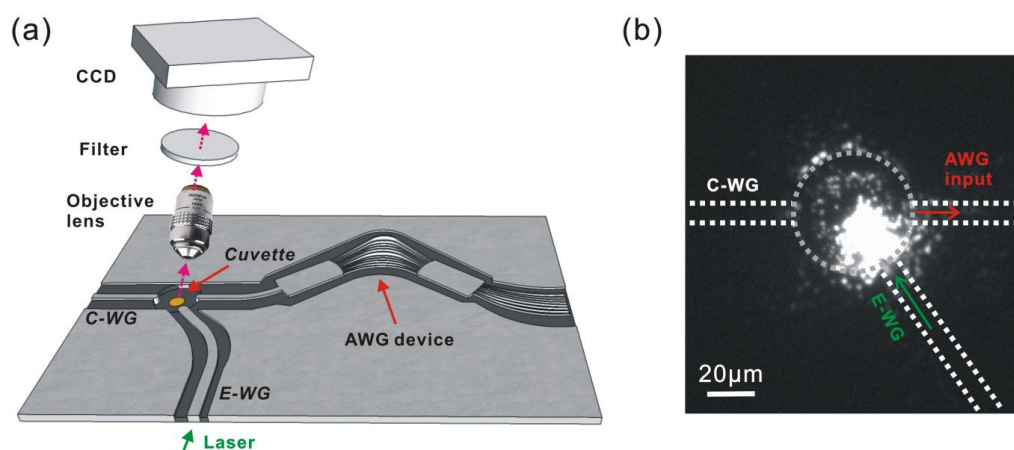


Figure 5.8 Experimental schematic and fluorescence image of the adsorbed micro beads. (a) Experiment setup for fluorescence measurement of the adsorbed micro beads. The laser excitation was introduced through the planar excitation waveguide (E-WG). The fluorescence signal was collected by the above objective lens ($\times 50$) and detected by a CCD camera after an emission filter. (b) the acquired fluorescence image of the adsorbed micro beads. The borders of the sampling cuvette and the three integrated waveguides were marked with grey dashed lines.

5.2.2.2 Fluorescence spectral multiplexing assay

As shown in Figure 5.9, the spectral multiplexing fluorescence measurement could be performed with the AWG platform. A laser light beam was fibre coupled into the planar excitation waveguide (E-WG). A 45° mirror and a $\times 4$ objective lens were used to reflect and project the AWG output signals to a vertically mounted CCD camera or a photon detector. In addition to verify the authenticity of the spectral signals collected from the different AWG output channels, the fluorescence signal from the sample was collected by an $\times 50$ objective lens above the cuvette and focused onto a fibre that was connected to a conventional spectrometer (TRIA320 from JOBIN YVON). The acquired fluorescence spectra were used to verify the results from the CCD camera. The combination of spectrometer and CCD camera measurement was repeated for each introduction of different fluorophores (i.e. fluorescence micro beads or quantum dots).

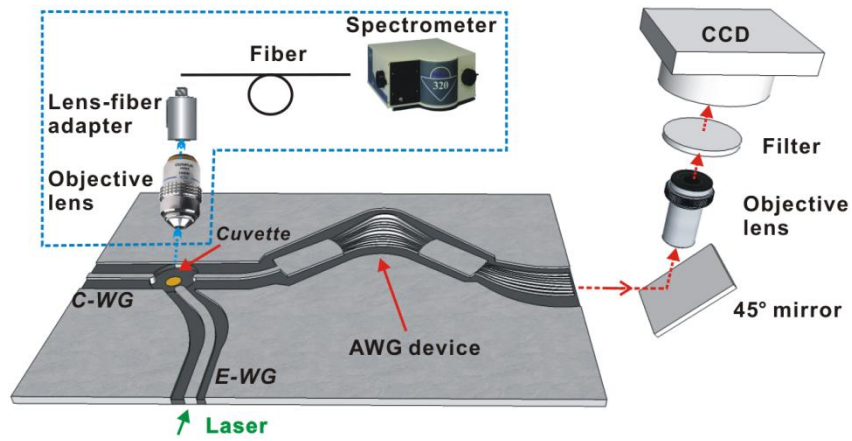


Figure 5.9 Experimental schematic of micro beads-based multiplexing fluorescence assay. A laser light beam was fibre coupled into the planar excitation waveguide (E-WG). A 45 ° mirror and a $\times 4$ objective lens were used to reflect AWG output signals onto a vertically mounted CCD camera or a photon detector. Prior to measurement with the CCD camera, fluorescence signal from the sampling cuvette was collected by an above $\times 50$ objective lens and then fibre connected to a conventional spectrometer (inside the blue dashed area). The acquired fluorescence spectra were used to verify the CCD detection results.

The fluorescence spectral multiplexing measurement results were shown in Figure 5.10. The graphs on the left show the fluorescence spectrum with the TRIAX spectrophotometer and those on the right hand side correspond to quantification of the CCD images of selected output channels (the corresponding CCD images are shown above the histograms of maximum light intensity). Specific AWG output channels, Ch1, Ch4 and Ch5 are shown since the spectral peaks of the three employed fluorophores (i.e. 682 nm for Flash Red fluorescence micro beads, 605 nm biotin conjugated quantum dots and 655 nm streptavidin conjugated quantum dots) were supposed to exit from these channels respectively. It should be noted that signals from other output channels were non-zero as well because of the relatively broad fluorescence spectra. Based on transmission spectral characteristics of the AWG device, however, the above three output channels were chosen to indicate each of the three fluorophores used in this work.

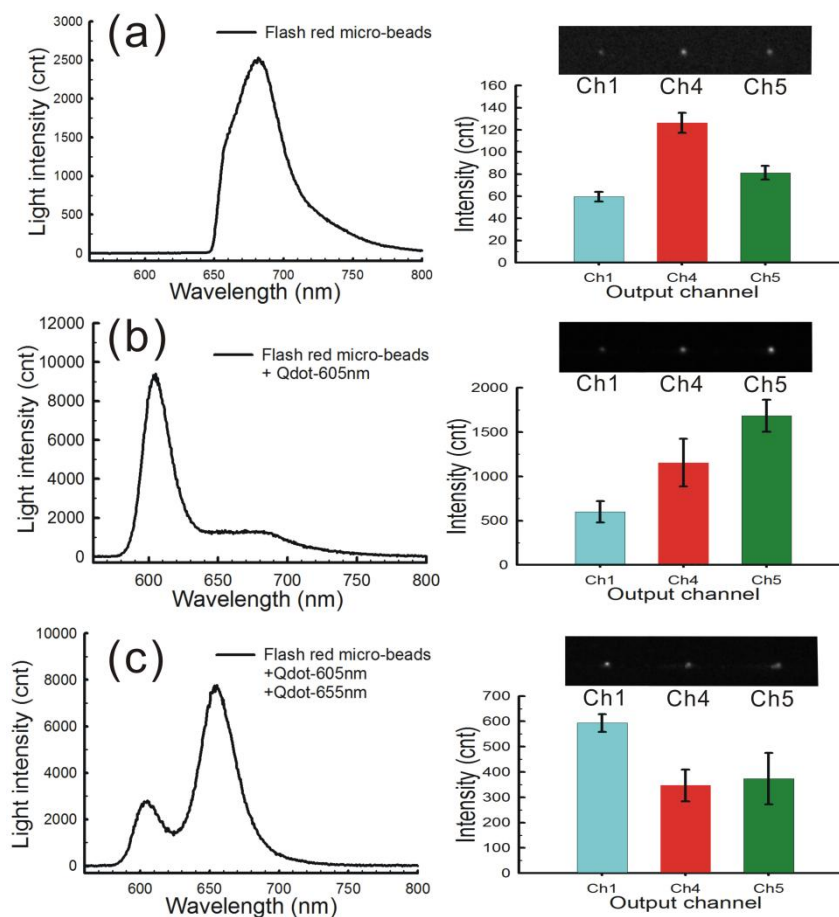


Figure 5.10 Fluorescence spectra and corresponding AWG+CCD detection results of the spectral multiplexing assay. (a) Flash red fluorescence micro beads. (b) After adding biotin conjugated quantum dots (605 nm). (c) After adding streptavidin conjugated quantum dots (655 nm). On the left are the pre-acquired fluorescence spectra while the right provides the CCD images of specific output channels and their histograms of light intensity maximum.

Figure 5.10a shows that after adsorption of the Flash Red fluorescence micro beads, the peak of the fluorescence spectrum was at 682 nm. It should be noted that the asymmetrical shape of the emission spectrum was caused by use of a 650 nm long pass filter in the light path to totally eliminate the 633 nm excitation signal. On the right of Figure 5.10a, the CCD image of Ch1, Ch4 and Ch5 is displayed and Ch4 was found to have the brightest spot as expected. Due to the broad spectrum of the flash red fluorescence emission, light spots were also found from other two channels although these were not as bright as Ch4; the quantitative measurement of their light intensity maximum is shown in the bar chart.

When the biotin conjugated quantum dots (605 nm) were added, another peak (i.e. 605 nm) was observed in the fluorescence spectrum, Figure 5.10b. As expected, now the highest level of light intensity was associated with Ch5 of the CCD image. The high wavelength spectral tail in Figure 5.10b reveals that the CCD image was a combination of fluorescence

emission that from both the quantum dots and the Flash Red fluorescence. In the same way, adding of streptavidin quantum dots (655 nm) unsurprisingly caused the brightest spot to move to Ch1 (see Figure 5.10c).

Finally, to demonstrate that the step-by-step immobilisation process was the consequence of streptavidin-biotin binding, the sampling cuvette was washed with a biotin solution for 4 to 5 times. Following this, all the spectral peaks came down in the intensity, and the fluorescence signal was too weak to be detected either TRIAX spectrophotometer or CCD camera. This shows that most of the emission signals detected in the previous measurements were a consequence of binding events. Thus these results have demonstrated a series of steps that could be introduced in a typical fluorescence spectral multiplexing assay. Importantly, it conceptually proved the potential capabilities of using the AWG device for multiplexed fluorescence detections. It should be pointed out however, that additional studies are needed to quantitatively evaluate the relationship between the pre-acquired fluorescence spectra and the CCD detection results. A control experiment should be conducted to ensure each step is performed effectively. Still, the preliminary qualitative results could provide promising opportunities to apply the AWG spectroscopic sensor for point-of-care multiplexing biosensing.

5.3 Experimental section

5.3.1 Immobilisation of quantum dots in the sample cuvette

5.3.1.1 Materials

(3-Aminopropyl)trimethoxysilane ($C_6H_{17}NO_3Si$, FW=179.29) was purchased from Sigma-Aldrich and Biotin (Long arm) NHS-water soluble (NHSws, cat# SP-1210) was from Vector Laboratories. Streptavidin conjugated quantum dots (655 nm, $2\mu M$) were from Invitrogen (Life Technologies Corporation). 0.1M phosphate buffered saline (PBS) (pH=7.4) was used as washing medium between each process step.

5.3.1.2 Patterning and immobilisation

The process flow diagram to create an immobilised quantum dot pattern is presented in Figure 5.11. Briefly, the top surface of the FHD silica based AWG device was first cleaned with organic solvent and piranha solution. The sample was then coated with aminosilane. A photolithography step was used to define a circular pattern, located at the centre of the sampling cuvette. Outside the pattern area, quantum dot immobilisation would be blocked by undeveloped photoresist. Next, a drop of NHS-Biotin solution was dispensed onto the pattern area (Figure 5.11c) and a chemical link was formed by reaction of amine and NHS group (Figure 5.11d). Subsequently, the undeveloped photoresist was removed by washing with DMSO. Streptavidin conjugated quantum dots immobilisation was performed by adding 2 μL QD655 solution onto the cuvette area and leaving for 30-minute incubation. Following the incubation, the sample was rinsed with PBS to remove the non-specific bonded quantum dots.

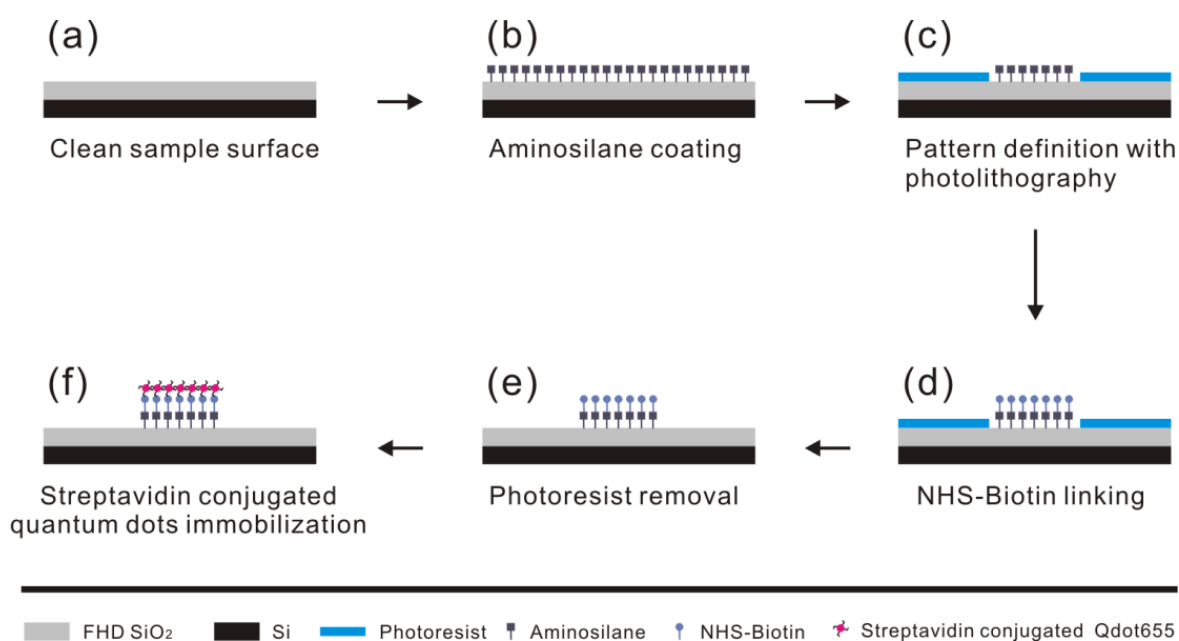


Figure 5.11 Process scheme of localising quantum dots in the centre of the sampling cuvette. (a) The surface of FHD silica based AWG device is cleaned with organic solvent and piranha solution. (b) The front surface is coated with aminosilane. (c) Photolithography is used to define the localised pattern outside which the surface is blocked by the undeveloped photoresist. (d) The exposed amine-reactive layer is linked with NHS-Biotin. (e) The undeveloped photoresist is removed by washing with DMSO. (f) Immobilisation of the streptavidin conjugated quantum dots through specific avidin-biotin binding.

The individual process steps corresponding to Figure 5.1 1a-f are described below.

(a) Cleaning of sample surface

The sample surface was firstly cleaned with organic solvent such as acetone and methanol. Subsequently, the sample was treated for 30 minutes in boiling piranha solution (3:1 concentrated $\text{H}_2\text{SO}_4:\text{H}_2\text{O}_2$). Then the sample was rinsed with ultrapure water and blow dried with a nitrogen gun.

(b) Aminosilane coating

The cleaned AWG sample was immersed in a solution of 5 vol% aminosilane in ethanol. The petri dish with the sample was put in a desiccators and left for 1 hour at room temperature. The sample was then rinsed with ethanol to remove unreacted silane and blow dried with a nitrogen gun.

(c) Pattern definition with photolithography

The aminosilane coated sample was patterned by photolithography. Shipley photoresist S1805 was spun at 4000 rpm for 30 second on the surface, resulting in a 0.5 μm film. Then the sample was prebaked 90 °C on hotplate for 3 minutes. After exposure under UV illumination (7.2 mW/cm^2) for 3 seconds, the sample was developed for 75 seconds with standard Microposit developer. The designed pattern was a round disk with 30 μm diameter in the centre of the sampling cuvette. To completely clean the resist residue in the exposed area, the sample was sent for 30-second oxygen plasma (@100W) before any chemical surface modification.

(d) NHS-Biotin linking

The water soluble NHS-Biotin was prepared in a solution with concentration of about 25 mg/mL. It should be noted that this reagent is very moisture-sensitive and only the required amount of solid powder should be weighed out. To avoid moisture condensation onto the product, the reagent vial must be equilibrated to room temperature before opening. The prepared NHS-Biotin water solution was added on the sampling cuvette area of the AWG device and incubated for 1 hour at room temperature. Following the incubation, phosphate buffered saline (PBS) solution was used to wash the sample surface, thereby remove excess biotin reagent and byproducts.

(e) Photoresist removal

After the step of NHS-Biotin linking, the undeveloped photoresist was removed by washing with an organic solvent named Dimethyl sulfoxide (DMSO). Generally, 10-minute immersion in DMSO should be enough to dissolve all the photoresist and gentle

sonication could be used occasionally to help the cleaning. Then the sample was rinsed with isopropanol alcohol (IPA) and blow dried with a nitrogen gun.

(f) Streptavidin conjugated quantum dots immobilisation

The streptavidin conjugated quantum dots (655 nm) were available in solution with a concentration of 2 μM . A pipette was used to dispense about 2 μL quantum dots solution onto the cuvette area for incubation. After 1 hour incubation, the sample was washed exhaustively with the PBS solution to remove non-specific bonded quantum dots on the surface.

5.3.2 Micro-beads immobilisation and bioconjugation reactions

5.3.2.1 Materials

Cysteamine hydrochloride (cat# 30078) was from Sigma-Aldrich and Biotin (Long arm) NHS-water soluble (NHSws, cat# SP-1210) was from Vector Laboratories, Inc. N-hydroxysuccinimide (NHS, cat# 24500) and 1-ethyl-3-[3-dimethylaminopropyl] carbodiimide hydrochloride (EDC, cat# 22981) were from Pierce Biotechnology (Thermo Scientific). Streptavidin coated microspheres with internal fluorophores (Flash Red, Excitation 660 nm, Emission 690 nm, diameter 0.97 μm) was from Bangs Laboratories, Inc. Biotin conjugated quantum dot (605 nm, 2 μM) and Streptavidin conjugated quantum dots (655 nm, 2 μM) were purchased from Invitrogen (Life Technologies Corporation). PBS buffer (100 mM, pH=8.5) and MES buffer (30 mM, pH=6.0) were prepared as the medium for washing or dilution purposes during the process.

5.3.2.2 Methods

The process flow diagram is presented in Figure 5.12. Following fabrication of the AWG chip, a metal deposition and a photolithography step were used to define a gold pattern in the centre of the sampling cuvette. After an Au wet etch process, a gold disk with diameter of 40 μm was obtained. A thiol functionalization procedure was utilized to selectively bind

recognition agents to the gold pattern for subsequent spectral multiplexing assay (Figure 5.12e).

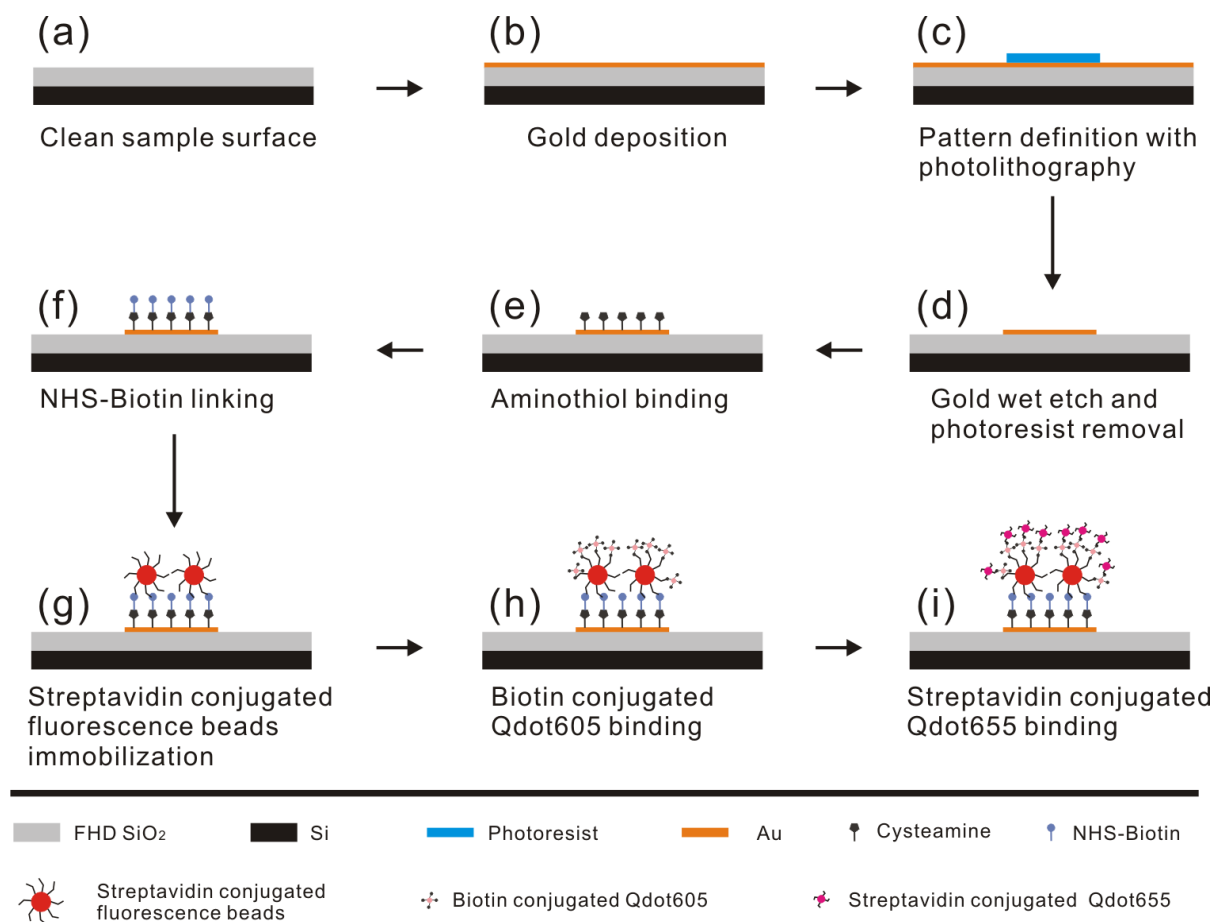


Figure 5.12 Process flow diagram of micro beads-based fluorescence assay. (a) The surface of FHD silica based AWG device is cleaned with organic solvent and piranha solution. (b) Deposition of gold layer. (c) Pattern definition with photolithography. (d) Gold wet etch and photoresist removal. (e) Aminothiol binding on the gold surface. (f) NHS-Biotin linking. (g) Adsorption of streptavidin conjugated micro beads. (h) Immobilisation of biotin conjugated quantum dots (605 nm). (i) Immobilisation of streptavidin conjugated quantum dots (655 nm).

Before surface functionalisation of the gold pattern, the AWG chip was cleaned with organic solvent and piranha solution. NH₂- terminated aminothiol (5 mM Cysteamine hydrochloride in DI water) was used to create a self-assembled monolayer (SAM) on the gold disk overnight (Figure 5.12e). NHS-ester activation was done by adding 2-3 mg Biotin (long arm) NHS to 100 μ L EDC/NHS solution (a mixture of EDC/NHS/MES buffer, EDC: 5 mM; NHS: 6 mM; MES buffer: 30 mM, pH=6.0) and reacting for 15 minutes at room temperature. Then the buffer pH was increased to about 7.7 by adding 100 μ L PBS buffer (100 mM, pH=8.5). Immediately, the solution was added onto surface of the

aminothiol modified gold disk and allowed reaction to proceed for 2 hours at room temperature (Figure 5.12f).

It is worth noting that streptavidin coated fluorescence beads need to be washed 2 or 3 times with a 10× volume of wash buffer through a centrifugation-resuspension process. 10 µL bead solution was used each time and a concentration of 0.1% solids was achieved by suspending the final pellet in wash buffer. Then a drop of the bead solution was placed onto the gold disk, allowing the streptavidin-biotin affinity interactions to occur over 30 minutes before washing. This step can be performed more than once in order to increase the density of immobilized fluorescence beads on the gold disk. It should, however, be noted that the number of non-specific bonded fluorescence beads increases with successive applications of solution as well. After immobilisation of streptavidin coated fluorescence beads, 2 µL solution of the biotin conjugated quantum dots (605 nm) was dispensed onto the gold disk followed by washing with buffer after 30 minutes. Likewise, the streptavidin conjugated quantum dots (655 nm) was added in order to perform a multiplexed Flash Red (682 nm), Qdot605 and Qdot655 spectral measurement.

Detailed surface functionalisation procedures (see Figure 5.12)

(a) Cleaning of sample surface

The sample surface was treated with acetone and methanol respectively. This was followed by treatment with a piranha solution (a mixture of concentrated sulphuric acid and hydrogen peroxide) for 30 minutes. Then the sample was rinsed with Deionised water and blow dried with a nitrogen gun.

(b) Deposition of gold layer

A layer of 20 nm gold was deposited on the top surface of the AWG device by using an electron beam evaporator in the clean room. To improve the adhesion between the gold layer and the FHD silica surface, 10 nm nichrome (NiCr) was first evaporated onto the surface.

(c) Pattern definition with photolithography

The gold coated sample was then patterned with photolithography. Firstly, the sample surface was spin-coated with a positive photoresist (S1805 from Shipley). Conventional

photolithography was used to expose the sample through a bright-field photomask with a $D = 40 \mu\text{m}$ disk. After the development, a size-identical photoresist disk was obtained on the gold layer. The developed sample was then treated with a 30-second oxygen plasma (@100 W) to completely remove any resist residue. Finally, the sample was hard-baked 120°C on hotplate for 5 minutes.

(d) Gold wet etch and photoresist removal

With the hard-baked photoresist as the mask layer, the sample was immersed in the gold etchant solution (a mixture of potassium iodide (KI) and iodine (I_2) solution). 10 seconds was enough to remove the gold layer without any masking. Subsequently, the sample was rinsed with water and blown dried before treating with nichrome etchant solution (a mixture of nitric acid and ceric ammonium nitrate) for about 10 seconds. Then the sample was rinsed, dried and immersed in acetone solution to remove the photoresist, leaving a clear gold disk pattern in the centre of the sampling cuvette which is shown in Figure 5.13.

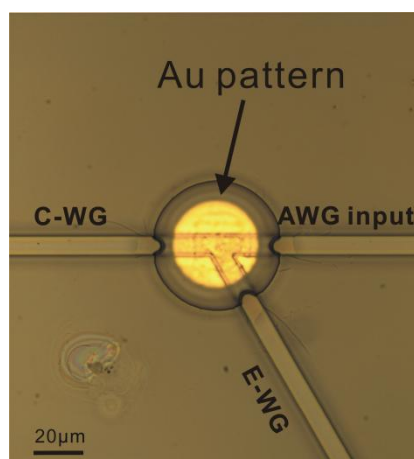


Figure 5.13 Gold disk pattern ($D=40 \mu\text{m}$) in the centre of the sampling cuvette

(e) Amino-thiol binding

The AWG device with gold disk pattern was immersed in a solution of NH_2 - terminated amino-thiol (5mM Cysteamine hydrochloride in deionised water) overnight to allow the reaction between the gold and $-\text{HS}$ group. Then the sample was exhaustively rinsed with PBS buffer to remove the excess reactive chemicals on the surface.

(f) NHS-Biotin linking

After amino-thiol binding, the sample was ready to form a NHS-Biotin linking which could provide reactive biotin groups for the following step. A water soluble biotin (long arm)

NHS reagent was used to link with the amine group (-NH₂) from previous step. The NHS group will hydrolyze rapidly in water solution, therefore a mixture of EDC and NHS was added to regenerate the amine-reactive NHS ester. The activation reaction with EDC and NHS is most efficient at pH 4.5-7.2 [234, 235], so the reactions were performed in a MES buffer (30 mM, pH=6.0). Following this, reaction of NHS-activated molecules with primary amines is most efficient at pH 7-8, therefore a PBS buffer (100 mM, pH=8.5) was added to increase pH value of the solution. Specifically, the NHS-ester activation was performed in MES buffer for 15 minutes at room temperature, then a pre-calculated volume of the PBS buffer was added into the solution which was immediately dispensed onto the aminothiols modified gold disk. After 2 hour incubation at room temperature, the sample was rinsed with the PBS buffer.

(g) Micro beads adsorption

Prior to the adsorption, a preliminary 2-3× wash should be performed to remove various additives including EDTA, anti-microbial, and surfactant. 10 μL of bead solution was placed in appropriate centrifuge tube followed by an addition of 1M PBS buffer. Then the tube was centrifuged at 10000 rpm for 15 minutes to give a clear supernatant which was then removed and discarded. The micro beads were resuspended in PBS buffer and the above steps repeated 2 or 3 times. Finally, a micro bead solution with a concentration of 0.1% solids (1 mg/mL) was obtained for subsequent use.

The prepared bead solution above was added onto the pre-patterned gold disk. The bead adsorption step was very important because excessive non-specific binding effect would adversely affect the validity and accuracy of the fluorescence assay. For this purpose, two other samples with gold pattern and identical surface chemistry were tested using different times for the incubation. After the incubation, the bead solution was pipetted off from the sample surface. Exhaustive rinsing with PBS buffer was used to remove the non-specific bonded beads. Figure 5.14 shows the comparative result with different lengths of incubation time for the beads adsorption. The non-specific bonded beads effect was obviously seen after the 60-minute incubation (5.14 b) while 30 minutes offered a more satisfactory result (5.14 a). Hence, a 30-minute incubation was used for the real AWG sample to allow the streptavidin-biotin affinity interactions and prevent excessive non-specific binding.

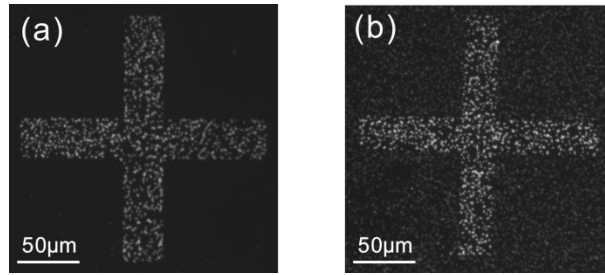


Figure 5.14 Sample test results of bead adsorption after different lengths of time. (a) 30 minutes. (b) 60 minutes.

(h) Immobilisation of biotin conjugated quantum dots

After micro beads adsorption, a fluorescence measurement could be performed with the AWG device and a CCD camera. For a spectral multiplexing assay, quantum dots (605 nm) with biotin conjugate were immobilised by binding with the streptavidin coated micro beads. 2 μ L quantum dots solution was dispensed onto the gold disk. After 30 minute incubation, the sample was washed with PBS buffer to remove excessive non-specific bonded quantum dots.

(i) Immobilisation of streptavidin conjugated quantum dots

With the immobilised quantum dots with biotin conjugate, a spectral multiplexing assay could be performed with the AWG device and a CCD camera. Similar to step (h), another layer of quantum dots with streptavidin conjugate were further bonded by the biotin-avidin affinity.

5.5 Summary

In this chapter, a modified AWG design with focusing properties was described. Firstly, the designed focusing properties of the lens-aided waveguides were visually evaluated by acquiring fluorescence images of the cuvette area using an upright fluorescence microscope. Then specific quantum dots were immobilized in the centre of the cuvette for localised fluorescence detection with a blue ray laser diode. Unfortunately, the directly immobilized quantum dots were not well excited by the laser light from the integrated E-WG because they were too far below the height of the E-WG waveguide to be illuminated. Therefore, streptavidin functionalized micro beads of an appropriate size were immobilized in advance to provide a solid support for quantum dots to be investigated. In addition to the emission from the micro beads, fluorescence from the other two different

quantum dots was detected. The step by step binding was realised by specific avidin-biotin affinity and each step was evaluated with the AWG+CCD platform as well as with a conventional spectrometer. The acquired spectrum from a conventional spectrometer for each step proved the intensity changes of the signals from the CCD camera. Overall, the preliminary results have demonstrated potential capabilities of using the adapted AWG device for localised multiplexing fluorescence detection.

6. Chapter 6

Absorption spectroscopic measurements

Abstract

In this study, the AWG-microfluidic device was investigated in the context of absorption spectroscopy measurements. As a model system, the pH dependence of the absorption spectra of bromophenol blue were measured to illustrate how an AWG device could be used as a colorimetric pH sensor. The results obtained demonstrate that the AWG-microfluidic device could yield a similar absorption detection performance to that of a commercially available spectrophotometer.

6.1 Introduction

As shown in Figure 6.1, bromophenol blue is an acid-base indicator with the color changing from yellow to blue when the pH increases. 0.01 M citric acid and 0.02 M Na_2HPO_4 were used to prepare the buffer solutions with different pH values. The bromophenol blue (B3269 from SIGMA) was dissolved in the buffer solution and the concentration was 1 mg/mL. The pH of the mixed solutions were finely adjusted to specific values by adding tiny volumes of a strong acid such as hydrochloric acid and using a pH meter (Consort C835) for real time monitoring.

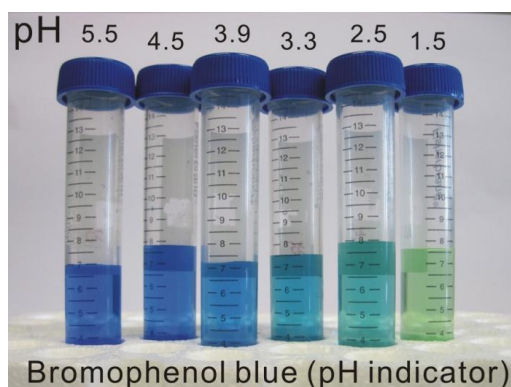


Figure 6.1 Bromophenol blue solutions with different pH. The color changes from yellow to blue when the pH increases.

6.2 Results and discussion

6.2.1 Absorbance measurements with conventional spectrophotometer

For verification purposes, the absorbance of bromophenol blue solutions with different pH was tested on a calibrated Hitachi U-2000 spectrophotometer using 1 mm pathlength cuvettes. A double beam system is implemented in this spectrophotometer and corresponding pH buffer solutions without bromophenol blue were placed into the reference channel to provide the background measurements. The absorption spectra of various bromophenol blue at different pH are shown in Figure 6.2. When the pH of bromophenol blue solution increased, the absorption peak in red region (~600 nm) increased in intensity while the blue peak (~420 nm) decreased. The measured spectra explain the color change from yellow to blue with an increase in the pH.

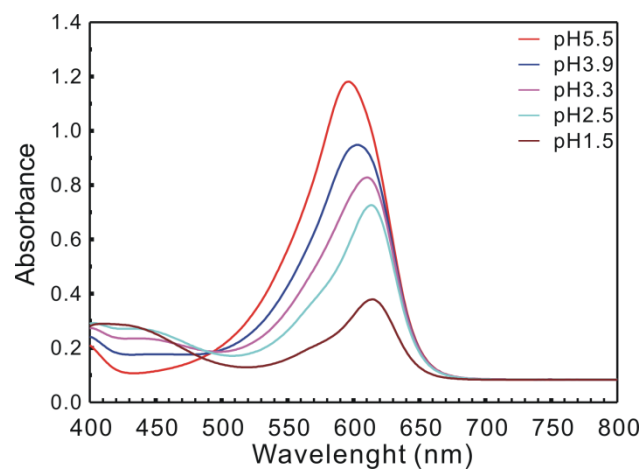


Figure 6.2 Absorption spectra of various bromophenol blue at different pH.

6.2.2 Absorbance measurements with AWG-microfluidic device and CCD

Bromophenol blue solutions from the same batch were also tested with the AWG-microfluidic device and a CCD camera. Compared to fluorescence measurements, absorption detection does not require the perpendicular waveguide designed for

fluorescence excitation. Instead, the characterization waveguide (C-WG) can be used for direct absorption measurement.

Figure 6.3 provides a schematic for absorption measurement with the AWG-microfluidic device and a CCD camera. A PDMS microfluidic chip with a microfluidic channel (10 mm long \times 500 μm wide \times 100 μm high) was plasma bonded with the AWG device. A square sampling cuvette (50 μm wide \times 2 μm deep) is located in the middle of the microfluidic channel. To perform the absorption spectroscopy measurement, a broad band light source was fibre coupled into the characterization waveguide (C-WG) and passed through the sample solution in the filled cuvette. The transmitted light was collected by the AWG input waveguide and sent to the AWG device for wavelength separation. A 45° mirror and a $\times 4$ objective lens were used to reflect the AWG output signals into the vertically mounted CCD camera.

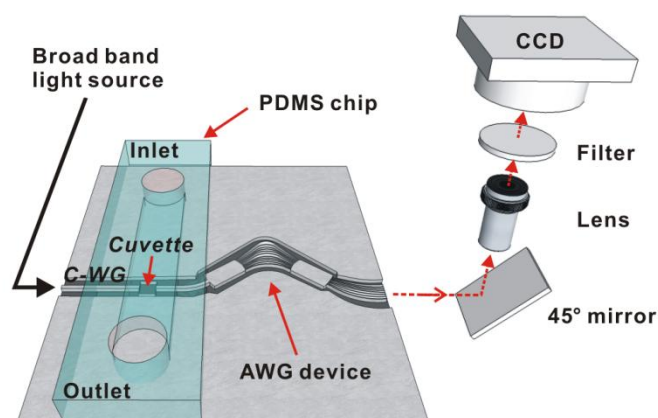


Figure 6.3 Schematic of absorption measurement with AWG-microfluidic device and CCD camera. A PDMS microfluidic chip was bonded with the AWG device and the square sampling cuvette (50 μm wide and 2 μm deep) is located in the middle of the microfluidic channel. A broad band light source was fibre coupled into characterization waveguide (C-WG) and travelled through the sample solution in the cuvette. The transmitted light is then collected by the AWG device for wavelength separation. A 45° mirror and a $\times 4$ objective lens were used to reflect AWG output signals onto a vertically mounted CCD camera. Due to the relatively narrow band periodical property of AWG transmission spectrum in this prototype device, a combination of a long-pass filter (550LP) and a short-pass filter (650SP) was used to restrain the wavelength range to be investigated.

6.2.2.1 Measurement results

The spectral results of the absorption measurement are displayed in Figure 6.4a. Bromophenol blue solutions with five different pH values were tested with the AWG-microfluidic device and CCD camera. To provide reference signals, pure buffer solutions with the same pH but without adding bromophenol blue were also measured. Each type of bromophenol blue solution was tested for at least three times. The absorption spectra from 570 nm to 625 nm are calculated by extracting the data from the CCD imaging results. For comparative analysis, Figure 6.4b shows the conventionally collected absorbance data from Figure 6.2, processed to generate the absorption spectra for a 50 μm light path. In terms of absorbance magnitude and spectral envelope, it can be seen clearly that the on-chip spectroscopic device yields a similar absorption detection performance to that of a commercially available spectrophotometer, but with an integrated micro-cuvette sample platform. It should be noted that the measurement curve at longer wavelengths for pH 5.5 Bromophenol blue solution didn't come down to converge with other curves compared to the result from a conventional spectrophotometer. One possible reason for this error might be bad crosstalk performance of these output channels caused by the stray light during the signal acquiring process. The relatively large variations (i.e. large error bars) between each test were caused by unsteady fiber coupling of the light source and signal collecting fluctuations of the external CCD camera. It is believed that more stable and reliable results can be obtained if all the function units including light source and signal detection are solidly integrated.

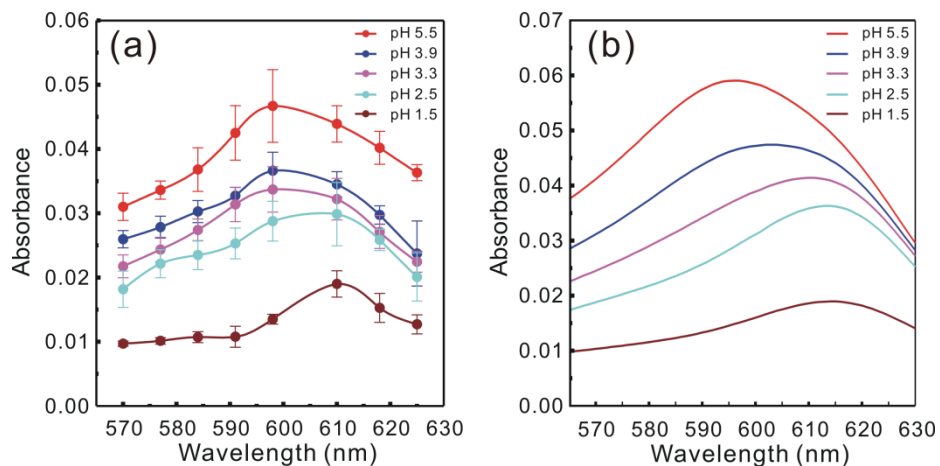


Figure 6.4 Absorption spectra of various bromophenol blue at different pH taken with (a) AWG-microfluidic device and (b) Hitachi U-2000 spectrophotometer. Error bars indicate \pm one standard deviation.

6.2.2.2 Light coupling issues induced by different waveguide

end-facet profiles

An ordinary flat-end profile could be incorporated into the two integrated waveguides facing each other [i.e. characterisation waveguide (C-WG) and AWG input waveguide], therefore performing direct absorbance measurements. Under this condition, the light coming out from the C-WG is divergent, thus the AWG input waveguide can only receive a portion of transmitted light signals which have gone through the investigated sample. The longer the light pathlength, the lower the light coupling efficiency will be. To decrease the diffraction power loss, either the light path needs to be reshaped or the signal collecting waveguide needs to enlarge its detection area.

In chapter 5, a lens profile was incorporated into the end of the integrated waveguides and the focusing properties could increase spatial resolution as well as reduce the background noise. However, these focusing waveguides imposed complications on absorbance measurements since the light coupling efficiency was sensitive to refractive index changes of investigated samples. It is worth noting the lens profiles described in chapter 5 were designed based on refractive index contrast of FHD silica ($n=1.478$) and pure water ($n=1.33$), however, different concentrations of bromophenol-buffer solution would unavoidably pose refractive index offsets and variations, affecting the focusing properties and thus reducing the light coupling efficiency. Absorbance measurements were performed using an AWG device with the focusing waveguides. Preliminary results showed that a more diluted pH buffer would help relieve adverse influences from the refractive index fluctuations.

Rather than using waveguides with focusing properties, a collimating system is considered more beneficial and practical to reduce the diffraction power loss, therefore acquiring reproducible and reliable measurement results. The Collimating system can be realised based on a parabola-shaped design [172] or with a compound microlens [28]. In comparison to conventional configuration, the effective light path length can be increased remarkably with the collimating system. More importantly, the collimator integrated detection cell could significantly increase the detection sensitivity and reduce stray light

noise. However, there was insufficient time to experimentally investigate this strategy in this thesis.

6.3. Experimental section

6.3.1 AWG-microfluidic device and experimental setup

As shown in Figure 6.5, the AWG device was bonded with a PDMS microfluidic chip to obtain a monolithic platform for absorption measurement. The yellow dashed lines indicate the walls of the microfluidic channel which passes through the sampling cuvette. Figure 6.5 (b) shows a microscopic image of the sampling cuvette located in the middle of the microfluidic channel. The bromophenol blue solution was delivered into the microfluidic channel through the inlet connected with a tubing which was driven by a syringe pumping system.

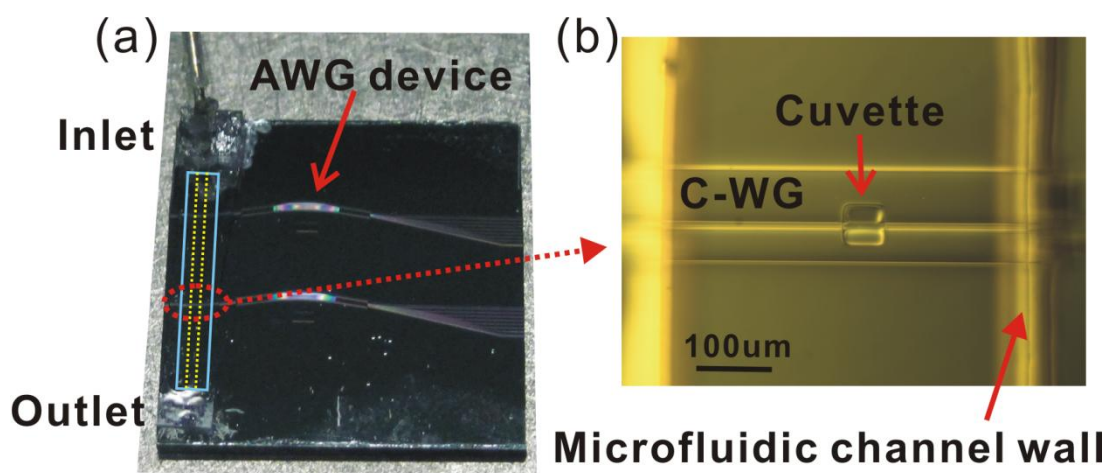


Figure 6.5 AWG-microfluidic device and the sampling cuvette. (a) AWG device bonded with a PDMS microfluidic chip. The microfluidic channel is indicated with yellow dashed lines. (b) microscope image of the sampling cuvette in the middle of the microfluidic channel.

Further images of the experiment setup for absorption measurement are presented in Figure 6.6. As with the fluorescence measurement of Chapter 4, the experiment setup was built on a modified microscope stage. A 3-axis micro-positioner was used to adjust the position of a V-groove holder on which a lensed fibre was utilized to couple the broad band light source into the characterization waveguide (C-WG) of the AWG device. The AWG-microfluidic

device was placed on a sample holder which was fixed in the centre of the modified microscope stage. Figure 6.6 (b) and (c) show the home-made mirror fabricated by depositing 75 nm NiCr on a small strip of silicon wafer; this mirror could be rotated as well as translated in two axes in order to place it in the correct position for reflecting the AWG output signals into the microscope's objective lens and CCD camera. The long-pass filter (550LP) and a short-pass filter (650SP) were inserted into the camera tube, underneath the CCD camera.

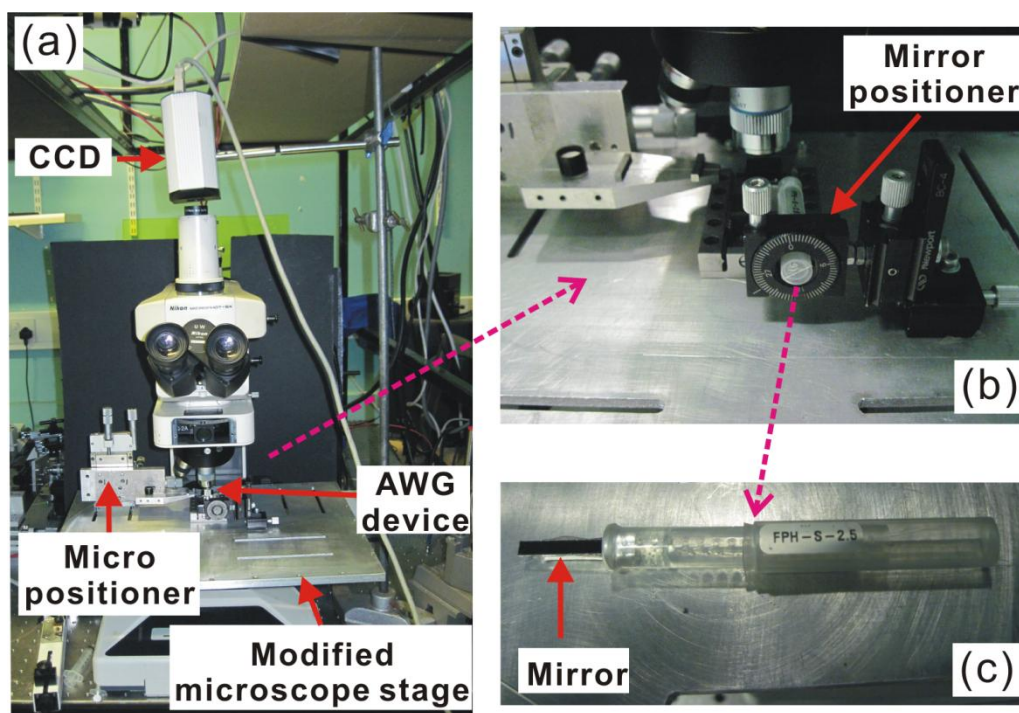


Figure 6.6 Experiment setup for the absorption measurement with AWG-microfluidic device and CCD camera. (a) Full view of the experiment setup. (b) A closer view of sample position stage and the mirror positioner. (c) The home made mirror.

6.4 Summary

On-chip visible absorbance detection of fluidic samples (bromophenol blue) was carried out using the AWG-microfluidic device and in house built experimental setup. With appropriate information processing, such an integrated system yielded accurate absorbance measurement results. Although the evaluation of the chip carried out was not sufficient to determine the detection limit and the linear range, it has demonstrated the successful integration of the individual components and proved the capabilities of on-chip spectroscopic device for absorption measurement.

7. Chapter 7

Conclusions and future work

7.1 Conclusions

This thesis has demonstrated a monolithic integrated Arrayed Waveguide Grating (AWG) microspectrometer-microfluidic platform for biological applications. Planar optoelectronic technologies for telecommunications were transferred and utilised to design AWG devices that operated in the visible wavelength region. Micromachining fabrication processes including lithography and reactive ion etching (RIE) were employed to define the AWG structure based on a FHD silica wafer. A polymer microfluidic chip, manufactured with replica moulding process, was bonded with the AWG device for fluidic sample control and delivery, ending up with an integrated AWG-microfluidic platform. Fluorescence detection as well as absorbance measurements were performed using this compact platform together with an external light source and CCD camera. Both the fluorescence spectroscopy measurements and multiplexing fluorescence assays have conceptually proved the capabilities of the AWG-microfluidic platform for a wide range of applications in biological sensing.

As reviewed in section 2.2, prior to commencing the work reported in this thesis, the efforts towards making visible AWG devices were far from enough to explore their potential applications for performing a range of chemical and biological assays. Thus, the research conducted in this thesis was targeted to contribute to investigations of these promising AWG devices in the visible wavelength range. Based on FHD silica material, an AWG device was designed and fabricated, operating with a centre wavelength of 680 nm, wavelength spacing of 10 nm and 8 output channels. The small dimension of this AWG device (~1cm long) makes it a good technological candidate to realise a microspectrometer. To develop new applications, microfluidic technology was combined with the planar waveguide platform of the AWG. Fluorescence detections involving intensity or spectral changes were conducted by using the AWG-microfluidic platform. Furthermore, waveguides with focusing properties were incorporated into the AWG design and localised,

multiplexing fluorescence detections were performed, opening up potential applications in the field of cell sorting and single cell analysis.

The ultimate goal of this work was to develop an integrated optical biosensor. Therefore, the thesis began with an introductory description of the components that comprise a portable optical sensor: light source, optical transducer, optical signal processing and signal detector. Emphasis in this work has been placed on developing a sub-unit for complex optical signal processing (i.e. a spectrophotometer) since the other three sub-units have been well-developed for applications in other areas. Miniaturization of spectroscopic optical component in particular was considered to be a critical step towards the goal for realizing a comprehensive, integrated optical biosensor. Different possible techniques were briefly discussed and reviewed, and an arrayed waveguide grating (AWG) device was selected for investigation due to its compact size, highly integrated capability, and design versatility.

7.1.1 Design and fabrication of AWG-microfluidic device

Having specified as a target, biological measurements in aqueous environment, AWG devices working in the visible wavelength range were designed by adapting the conventional near-infrared AWG technology. Fortunately, a software utility based on the Beam Propagation Method (BPM) was available for the AWG design. A visible AWG device based around a central wavelength of $\lambda_c=680$ nm, with 8 output channels and 10 nm inter channel resolution was successfully designed and simulated to predict the device's performance. Considering access to high quality waveguide material made from FHD silica and local expertise, the AWG device was fabricated from a system based on a 2 μm FHD core layer and 8 μm silica under-cladding.

To fabricate the AWG device, lithography and reactive ion etching (RIE) processes were utilised to define all the features in the AWG structure. In the course of fabrication process, a number of practical issues were encountered including those associated with different lithography techniques, metal lift-off methods, and dry etch processing. Photolithography provided a fast method to transfer the AWG pattern from the photo mask onto the FHD

silica wafer due to its parallel UV radiation. Due to the high density of narrow features in the AWG structure, a thin film (500 nm) photoresist (S1805) was used for the photolithography. To transfer the AWG pattern into the FHD silica, an RIE process was employed to remove unwanted materials and obtain the desired waveguide height (2 μm). However, because the thin film photoresist was not resistant enough to support the etching of 2 μm silica, a metal mask of 75 nm NiCr was utilised for the etching process. An innovative lift-off process, involving 1 minute soaking of the resist coated sample in the standard developer before exposure, was employed to obtain a clear and clean metal pattern.

Whilst photolithography proved to be extremely suitable to obtain high fabrication throughputs and short processing times, it lacks flexibility when design iterations need to be made (since it relies on pre-patterned mask plates.) As an alternative, e-beam lithography offers a mask-free approach for transferring the pattern onto the wafer. Taking into account relatively large pattern area of AWG structure, two fast (sensitive) electron beam resists namely, SU-8 and UVIII, were investigated. Dose tests were conducted for both materials and although that for SU-8 was lower, it was found to be less suitable for the fine structures in the AWG devices due to the narrowness of doses that gave good exposures and the extreme sensitivity of the curing process to temperature after electron beam writing. This resulted in a non-reproducible process. Compared to SU-8, although a slightly higher dose was required, the improved pattern fidelity and increased yield made UVIII the favoured choice for AWG device fabrication. Moreover, UVIII was already known to have good dry etch resistance, therefore no additional etch mask layers was required.

Since the waveguide sidewall profile and surface roughness have a great impact on the optimal performance of the AWG device, the reactive ion etching (RIE) process that defined the waveguides was carefully investigated. The parameters such as gas selection, gas flow rate, RF power and chamber pressure, were carefully varied to obtain optimised conditions for the FHD silica dry etching. In particular, surface profiles were compared for samples etched when a metal mask layer and different process gases were used. The results obtained suggested that CHF_3/O_2 was more suitable than CHF_3/Ar to achieve a high quality waveguide sidewall profile and a clean substrate surface.

To create an over cladding layer on the FHD core waveguides, a flowable oxide (HSQ) was spun on the FHD wafer. This was followed by deposition of an additional 200 nm PECVD SiO₂ protecting layer. This step completed the fabrication of a basic AWG device. However, to employ the AWG device for on-chip bio-sensing, a sample cuvette needs to be incorporated to provide a physical site for sample loading. Thus, further lithographic steps and RIE processes were employed. Finally, a PDMS chip with microfluidic channels was prepared by replica moulding process (this is a well-known and inexpensive, flexible and easy-to-fabricate method). The AWG device and the PDMS chip were plasma bonded together, leading to a monolithic integrated platform for biological measurements. The AWG device could collect and process the light signals while the PDMS chip could be used for fluidic sample delivery.

7.1.2 Optical characterisation of AWG system

Two methods have been applied to evaluate the AWG-microfluidic system. In one method, a broad band light source and a conventional spectrometer were utilised to test the device. The spectrum of the light from each of the output channels comprised a series of narrow bandwidth peaks (~10 nm FWHM) separated by a free spectral region of ~100 nm. This indicated proper operation of the AWG device and was consistent with the simulation results. In the second method, a monochromatic light source and a CCD camera were used for the device validation. Here, the number of photons, in a wavelength range defined by the monochromator, that came out of the output waveguides were ‘counted’ by the CCD chip. This latter testing scheme was favoured since it shared the same configuration with that employed for the following biological measurements.

7.1.3 Use of AWG-microfluidic device for simultaneous, multiplex fluorescence measurements

To demonstrate the effective capability of the AWG device in the discrimination of wavelengths in an assay context, a solution comprising two different quantum dots namely, QD655 and QD705, was tested. The quantum dots solution was placed in the

micromachined sample cuvette, and illuminated by a blue light (~400 nm). The fluorescence emission was collected by the AWG device and the output light signals were analyzed by a conventional spectrometer. The results obtained demonstrated that the wavelength peaks from the two quantum dots (655 nm and 705 nm) were found from two unique output channels (Ch1 and Ch6) respectively. Solutions including one sort of quantum dot as well as their mixture were all tested, leading to a convincing result for the AWG device validation and also opening up the possibility of assaying a sample containing multiple targets.

7.1.4 Quantitative fluorescence spectroscopic measurements with an AWG device

The suitability of the AWG-microfluidic platform for performing an accurate, quantitative, spectroscopic fluorescence measurement was evaluated by collecting the emission spectrum of Cy5 fluorophore. In addition to the co-axial characterization waveguide (C-WG), an off-axis excitation waveguide (E-WG) was incorporated into the design for these devices. This E-WG intercepts the sample cuvette at an angle of 45° to the AWG input waveguide axis to minimise the amount of excitation light entering the AWG structure. To validate this configuration, various concentrations of Cy5 were delivered into the microfluidic channel at a flow rate of 6.7 mm/s. Firstly, a conventional spectrometer was again employed to detect the light signals and different light spectra were acquired one by one for each output channel. Then a CCD camera was mounted to detect all of the output signals simultaneously. It was found that plotting the intensities of the 8 light spots from the CCD images versus their centre wavelengths clearly replicated the envelope of the Cy5 emission spectrum. Thus, the AWG-microfluidic platform in conjunction with an imaging camera provided a facile way to achieve a spectroscopic measurement. Moreover, the obtained results from various concentrations revealed the potential capability for quantitative fluorescence measurements.

The Cy5 fluorescence spectroscopic measurement opened up possibilities for assays that involve detecting both intensity and shape of spectra by using the AWG-microfluidic platform. Therefore, a propidium iodide (PI)-DNA assay was conducted. Propidium iodide (PI) is a fluorescence dye and intercalating agent, commonly used for quantitative analysis

of DNA. Adding PI to DNA contained solution, the PI fluorescence intensity is significantly enhanced and its emission peak exhibits a blue-shift. For the assay measurement, 15 μM PI solutions with a range of DNA concentrations and without DNA were tested with the AWG-microfluidic platform. The fluorescence intensity enhancement was clearly found from the obtained results. Unfortunately, the peak of the unbound PI fluorescence is not located within the range of the AWG output. However, the peak of the DNA-bound PI fluorescence (614 nm) could be found from output channel 6. When compared to the way that the CCD counts for unbound PI fluorescence monotonically increased with channels number, the peak in the CCD count-channel number plot for DNA-bound PI emission suggested that a peak blue-shift in PI fluorescence had occurred.

7.1.5 Shaping the beam profile in the AWG device cuvette for voxel-like measurements

When considering the capability for multiplexed assay, an AWG device that could possibly be applicable for flow cytometry was proposed. Thus, a lens design was incorporated at the ends of the integrated waveguides (C-WG, E-WG and I-AWG) that intersect with the sample cuvette. This meant that the size of the optical interrogation area could, in theory, be reduced to the focal point of the system. After fabricating waveguides with focusing profiles, evaluation was performed by fluorescence detection. For comparison, parallel measurements using AWG devices without lens design were also tested, confirming the focusing functionality of the lens curvature. As a test, fluorescence source, quantum dots were directly immobilised in the centre of the sample cuvette. Unfortunately, the emission detection was not successful because the layer of immobilised quantum dots were too low (close to the bottom surface of the micro-machined cuvette) to be illuminated by the light from the excitation waveguide (E-WG). To resolve the problem, 1 μm silica beads were used to provide a solid support that positioned the quantum dots above the base of the cuvette and in the E-WG optical path. In addition, this voxel-like configuration was explored using commercially available fluorescence silica beads source, to which other fluorophores could be subsequently bonded. In this work, a thiol functionalization procedure was employed to immobilise the fluorescence micro beads in the centre of the sample cuvette where a gold disk pattern had been pre-defined. These streptavidin conjugated fluorescence beads had an emission peak at 682 nm leading to the brightest

spot appearing from Ch4, as expected. After bead immobilisation, biotin conjugate quantum dots (QD605) were added to the cuvette and bound to the immobilised silica spheres through biotin-avidin affinity. The peak of the composite fluorescence emission then shifted to 605 nm and Ch5 was found to be the most intense light spot. Likewise, when a second set of quantum dots (QD655) with streptavidin conjugate were adsorbed onto the 605 nm biotin quantum dots, Ch1 became the brightest channel. It should be noted that spectroscopic measurements with a conventional spectrometer were performed after adsorption of each fluorophore, used to verify the AWG-CCD based results. The obtained results successfully demonstrated the potential capabilities to perform multiplexed fluorescence assays with the lens-design aided AWG device. In the future, instead of using micro silica beads, specific biological cells could be localised at the focus of the AWG input waveguide and subjected various fluorescence labelling protocols. This detection format could also be expanded using hydrodynamic or dielectrophoretic focusing, to multiplexed flow cytometry in a compact format.

7.1.6 Absorbance measurements with an AWG device

Although possibly less exciting; conventional absorbance measurements were tested with the AWG-microfluidic platform. The absorption spectra of bromophenol blue solutions with different pH were acquired by using both a conventional spectrophotometer and AWG-microfluidic system. It was found from the obtained result that the on-chip spectroscopic device could offer similar absorption detection performance to commercially available spectrophotometer.

7.2 Future work

7.2.1 AWG device loss characterization and reduction

The obtained results in this work successfully demonstrated the capability of the AWG-microfluidic platform for spectroscopic biological measurements; however, the ultimate capabilities/detection limits could not be determined without carefully performing the AWG device loss characterization. One important reason why the system loss evaluation was not conducted is that the current AWG devices were operating with relatively high

losses where the light sources were coupled into the chip; hence this needs to be further developed to obtain optimised conditions before a full loss characterisation study is warranted.

For an AWG device, the main intrinsic loss contribution comes from (1) propagation in the waveguides, and (2) coupling between free slab regions and arrayed waveguides. The wavelength range used, physical size of the waveguides, bending radius, sidewall roughness and cladding uniformity, all contribute to the induced propagation loss. Generally, the wavelength range to be investigated is decided by the target application, like 680 nm used for the visible AWG devices in this work. As described in Chapter 2, the height and width of the high index contrast ($\Delta=1.5\%$) arrayed waveguides were designed with 2 μm according to the single mode operation mechanism [i.e. height (width) < 2.2 μm]. For future work, the size of the waveguides can be increased slightly, leading to a better light coupling while still being able to retain single mode propagation attributed to mode perturbation by the bending curvatures. As discussed in Chapter 3, the sidewall roughness was mainly determined by the dry etching process and an acceptable result has been achieved using current optimised parameters. Although the HSQ material shows superior properties in gap-filling and self-planarization, some drawbacks also exist due to its simple coating method of spinning followed by hard baking. In this work, the spun HSQ underwent 1 hour baking in a 180 $^{\circ}\text{C}$ oven and microcracks as shown in Figure 7.1 occasionally appeared due to high intrinsic tensile stress of the material. Moreover, higher temperature is possible to change the refractive index of HSQ, and this may result in material reliability issues. Two possible approaches could be employed to overcome this problem. The first is to introduce a more optimized curing process for the HSQ [201] and the other is to find an alternative material for the over-cladding. (Note: although PECVD SiO_2 and SiN were available in the university clean room, the deposition tools were not equipped with the facilities for control of the refractive indexes.)

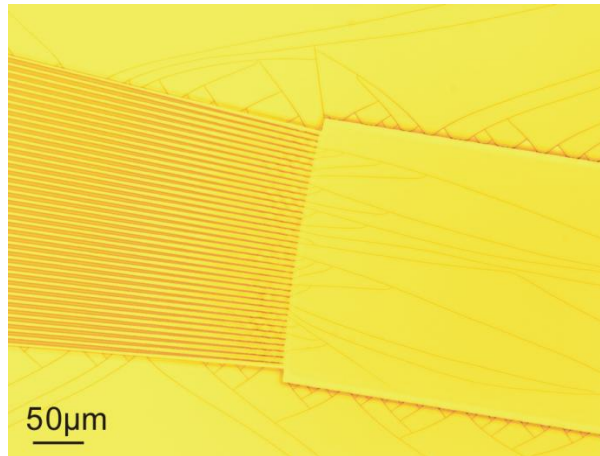


Figure 7.1 Microscope image showing the microcracks of HSQ after the hard baking

The important loss contribution that comes from the mode transition between the free slab regions and arrayed waveguides could be eliminated if the gaps between the arrayed waveguides near the free slab region can be made infinitely sharp. However, this can not be achieved in practice due to the finite resolution of the lithography and the etching process as shown in Chapter 3 Figure 3.2. Therefore, other practical approaches need to be considered. Adiabatic transition between the array and the slab region is desirable to reduce the junction loss. Different mode converters have already been proposed, including segmented waveguides [236], vertical tapered structures [237-239], and Y-branches [240]. For the same purpose, UV-written tapers [241] and interference fringes [242] were also proposed to reduce the transition loss. However, it should be noted that all these approaches require additional complexity for either design or fabrication process.

7.2.2 Increasing light collecting efficiency of AWG input waveguide

In addition to the AWG device loss, the signal collecting efficiency of the input waveguide also plays an important role in determining the limit of detection. The current AWG device has already reached the maximum of its potential capability since the collecting waveguide was located with effectively zero distance from the signal source [243]. However, some innovative approaches are still greatly desirable to allow the AWG device to collect more light signals from sample being investigated. Although not directly applicable for on-chip configuration, some recent work provided useful clues for assisting to find some practical

solutions in the future. N.Ismail et al proposed an AWG sensor by collecting sample light based on integrated waveguide array [244-246]. Although the collecting efficiency could be increased by more than 1 order of magnitude compared to a standard AWG device, the capabilities for spectroscopic measurements need to be further proved. Another interesting work tried to increase light collecting efficiency by using photonic lanterns which could convert multimode light to single-mode propagation with low loss [247-249]. Unfortunately, this method relied on a photonic crystal fibre technique which is currently off-chip. Above all, the use of AWG devices for ambient/diffused light detection is always troublesome because of power considerations. The small device size is a result of the fact that only the fundamental mode is allowed. Therefore, more creative research needs to be conducted to tackle this challenge. For inspiration, the problem could possibly be attacked from another perspective, shaping the light signal from the sample according to the input waveguide.

7.2.3 Polymer AWG device

As discussed in Chapter 3, polymer microfluidic chips are widely used for chemical analysis and biological sensing due to its unique polymer characteristic such as biocompatibility, low cost, and rapid prototyping capability by soft lithography. If a polymer based AWG device can be made, its easy integration with microfluidics will lead to monolithic lab-on-chip for spectroscopic measurements. A simple four-channel PDMS AWG device has been demonstrated for operation in the visible light wavelength range [250]. It is believed that more interesting work in this regard can be performed in the future.

7.2.4 Applications

7.2.4.1 On-chip Raman spectroscopy measurements

Raman spectroscopy is a label-free technique to identify specific molecules or structures and most well-established laboratories have been equipped with Raman instruments. However, a low-cost, and compact apparatus for Raman spectroscopy is desirable for field applications. An AWG device has been recently applied to Raman spectroscopy based on an off-chip configuration [251]. In the future, an on-chip approach with AWG device for Raman spectroscopy should be worthy of investigation.

7.2.4.2 Flow cell cytometry

Implementing the AWG-microfluidic platform in more sophisticated biological application is expected for the future work. As described in Chapter 5, the AWG-microfluidic platform has demonstrated its capabilities for multiplexing and localised fluorescence assay, and this could be employed for cell analysis with micro flow cytometry. Progress made toward this goal throughout the course of the PhD research period is shown by immobilising a single cell in the centre of the sample cuvette (see Figure 7.2). Further measurements on this system should be performed in the future.

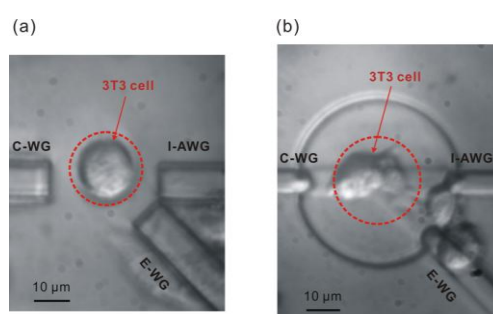


Figure 7.2 3T3 cell immobilisation in the centre of the sample cuvette using different AWG devices: (a) conventional design; (b) with focusing waveguides. C-WG: waveguide for characterization; E-WG: excitation waveguide; I-AWG: input of the AWG device.

References

1. Clark Jr, L.C. and C. Lyons, *Electrode systems for continuous monitoring in cardiovascular surgery*. Annals of the New York Academy of Sciences, 1962. 102(1): p. 29-45.
2. Borisov, S. and O. Wolfbeis, *Optical biosensors*. Chem. Rev, 2008. 108(2): p. 423-461.
3. McDonagh, C., C.S. Burke, and B.D. MacCraith, *Optical chemical sensors*. Chemical reviews, 2008. 108(2): p. 400-422.
4. Velasco-Garcia, M. *Optical biosensors for probing at the cellular level: A review of recent progress and future prospects*. Seminars in Cell & Development Biology, 2009: p.27-33.
5. Gauglitz, G., *Direct optical detection in bioanalysis: an update*. Analytical and bioanalytical chemistry, 2010. 398(6): p. 2363-2372.
6. Scully, P., et al., *Optical Sensors and Biosensors for Environmental Monitoring. Biomonitoring and Biomarkers as Indicators of Environmental Change 2*, 2001: p. 175-199.
7. Bourgeois, W., et al., *The use of sensor arrays for environmental monitoring: interests and limitations*. J. Environ. Monit., 2003. 5(6): p. 852-860.
8. Narayanaswamy, R., *Optical chemical sensors and biosensors for food safety and security applications*. Acta Biologica Szegediensis, 2006. 50(3-4): p. 105-108.
9. Gatzoulis, L. and I. Iakovidis, *Wearable and portable eHealth systems*. Engineering in Medicine and Biology Magazine, IEEE, 2007. 26(5): p. 51-56.
10. Myers, F.B. and L.P. Lee, *Innovations in optical microfluidic technologies for point-of-care diagnostics*. Lab on a Chip, 2008. 8(12): p. 2015-2031.
11. Brettell, T.A., J.M. Butler, and J.R. Almirall, *Applications Review: FORENSIC SCIENCE*. Analytical Chemistry, 2011. 83(12): p. 4539-4556.
12. Roda, A., et al., *Portable device based on chemiluminescence lensless imaging for personalized diagnostics through multiplex bioanalysis*. Analytical Chemistry, 2011. 83(8): p. 3178-3185.
13. Marazuela, M. and M. Moreno-Bondi, *Fiber-optic biosensors-an overview*. Analytical and bioanalytical chemistry, 2002. 372(5): p. 664-682.
14. Leung, A., P.M. Shankar, and R. Mutharasan, *A review of fiber-optic biosensors*. Sensors and actuators B: Chemical, 2007. 125(2): p. 688-703.
15. Krawczyk, S., *Discussion on optical integration in Lab-on-a-Chip microsystems for medical diagnostics*. physica status solidi (c), 2003(3): p. 998-1012.
16. Verpoorte, E., *Chip vision-optics for microchips*. Lab on a Chip, 2003. 3(3): p. 42N-52N.

17. Mogensen, K.B., H. Klank, and J.P. Kutter, *Recent developments in detection for microfluidic systems*. Electrophoresis, 2004. 25(21-22): p. 3498-3512.
18. Balslev, S., et al., *Lab-on-a-chip with integrated optical transducers*. Lab Chip, 2005. 6(2): p. 213-217.
19. Kuswandi, B., J. Huskens, and W. Verboom, *Optical sensing systems for microfluidic devices: A review*. Analytica chimica acta, 2007. 601(2): p. 141-155.
20. Mukundan, H., et al., *Waveguide-based biosensors for pathogen detection*. Sensors, 2009. 9(7): p. 5783-5809.
21. Salimi-Moosavi, H., et al., *A multireflection cell for enhanced absorbance detection in microchip-based capillary electrophoresis devices*. Electrophoresis, 2000. 21(7): p. 1291-1299.
22. Lee, K.S., H.L.T. Lee, and R.J. Ram, *Polymer waveguide backplanes for optical sensor interfaces in microfluidics*. Lab Chip, 2007. 7(11): p. 1539-1545.
23. Ibarlucea, B., et al., *Cell screening using disposable photonic lab on a chip systems*. Analytical Chemistry, 2010. 82(10): p. 4246-4251.
24. Roulet, J.C., et al., *Microlens systems for fluorescence detection in chemical microsystems*. Optical Engineering, 2001. 40: p. 814-821.
25. Roulet, J.C., et al., *Performance of an integrated microoptical system for fluorescence detection in microfluidic systems*. Analytical Chemistry, 2002. 74(14): p. 3400-3407.
26. Kwon, S. and L.P. Lee, *Micromachined transmissive scanning confocal microscope*. Optics letters, 2004. 29(7): p. 706-708.
27. Seo, J. and L.P. Lee, *Disposable integrated microfluidics with self-aligned planar microlenses*. Sensors and actuators B: Chemical, 2004. 99(2): p. 615-622.
28. Ro, K.W., et al., *Integrated light collimating system for extended optical-path-length absorbance detection in microchip-based capillary electrophoresis*. Analytical Chemistry, 2005. 77(16): p. 5160-5166.
29. Song, C., et al., *Modelling and optimization of micro optofluidic lenses*. Lab Chip, 2009. 9(9): p. 1178-1184.
30. Dandin, M., P. Abshire, and E. Smela, *Optical filtering technologies for integrated fluorescence sensors*. Lab Chip, 2007. 7(8): p. 955-977.
31. Richard, C., et al., *An integrated hybrid interference and absorption filter for fluorescence detection in lab-on-a-chip devices*. Lab Chip, 2009. 9(10): p. 1371-1376.
32. Ryu, G., et al., *Highly sensitive fluorescence detection system for microfluidic lab-on-a-chip*. Lab Chip, 2011. 11(9): p. 1664-1670.
33. Zeller, P.N., G. Voirin, and R.E. Kunz, *Single-pad scheme for integrated optical fluorescence sensing*. Biosensors and Bioelectronics, 2000. 15(11): p. 591-595.

34. Hofmann, O., et al., *Three-dimensional microfluidic confinement for efficient sample delivery to biosensor surfaces. Application to immunoassays on planar optical waveguides*. Analytical Chemistry, 2002. 74(20): p. 5243-5250.
35. Adrian, J., et al., *Waveguide interrogated optical immunosensor (WIOS) for detection of sulfonamide antibiotics in milk*. Biosensors and Bioelectronics, 2009. 24(11): p. 3340-3346.
36. Piliarik, M., et al., *Compact and low-cost biosensor based on novel approach to spectroscopy of surface plasmons*. Biosensors and Bioelectronics, 2009. 24(12): p. 3430-3435.
37. Kou, Q., et al., *On-chip optical components and microfluidic systems*. Microelectronic engineering, 2004. 73: p. 876-880.
38. Llobera, A., R. Wilke, and S. Buttgenbach, *Poly (dimethylsiloxane) hollow Abbe prism with microlenses for detection based on absorption and refractive index shift*. Lab Chip, 2004. 4(1): p. 24-27.
39. Huang, S.H. and F.G. Tseng, *Development of a monolithic total internal reflection-based biochip utilizing a micropillar array for fluorescence sensing*. Journal of Micromechanics and Microengineering, 2005. 15: p. 2235-2242.
40. Llobera, A., R. Wilke, and S. Buttgenbach, *Optimization of poly (dimethylsiloxane) hollow prisms for optical sensing*. Lab Chip, 2005. 5(5): p. 506-511.
41. Ibarlucea, B., et al., *Selective functionalisation of PDMS-based photonic lab on a chip for biosensing*. Analyst, 2011. 136(17): p. 3496-3502.
42. Thrush, E., et al., *Integrated bio-fluorescence sensor*. Journal of Chromatography A, 2003. 1013(1): p. 103-110.
43. Edel, J.B., et al., *Thin-film polymer light emitting diodes as integrated excitation sources for microscale capillary electrophoresis*. Lab Chip, 2004. 4(2): p. 136-140.
44. Thrush, E., et al., *Integrated semiconductor vertical-cavity surface-emitting lasers and PIN photodetectors for biomedical fluorescence sensing*. Quantum Electronics, IEEE Journal of, 2004. 40(5): p. 491-498.
45. Burns, M.A., et al., *An integrated nanoliter DNA analysis device*. Science, 1998. 282(5388): p. 484-487.
46. Adams, M.L., et al., *Microfluidic integration on detector arrays for absorption and fluorescence micro-spectrometers*. Sensors and Actuators A: Physical, 2003. 104(1): p. 25-31.
47. Yotter, R.A. and D.M. Wilson, *A review of photodetectors for sensing light-emitting reporters in biological systems*. Sensors Journal, IEEE, 2003. 3(3): p. 288-303.
48. Balslev, S., et al. *Fully integrated optical system for lab-on-a-chip applications*. 17th IEEE international Conference on MEMS, 2004: p.89-92.

49. Pais, A., et al., *High-sensitivity, disposable lab-on-a-chip with thin-film organic electronics for fluorescence detection*. Lab Chip, 2008. 8(5): p. 794-800.
50. Luff, B.J., et al., *Integrated optical Mach-Zehnder biosensor*. Journal of lightwave technology, 1998. 16(4): p. 583-592.
51. Shew, B.Y., et al., *UV-LIGA interferometer biosensor based on the SU-8 optical waveguide*. Sensors and Actuators A: Physical, 2005. 120(2): p. 383-389.
52. Ymeti, A., et al., *Fast, ultrasensitive virus detection using a young interferometer sensor*. Nano letters, 2007. 7(2): p. 394-397.
53. Homola, J., S.S. Yee, and G. Gauglitz, *Surface plasmon resonance sensors: review*. Sensors and actuators B: Chemical, 1999. 54(1-2): p. 3-15.
54. Dostalek, J., et al., *Surface plasmon resonance biosensor based on integrated optical waveguide*. Sensors and actuators B: Chemical, 2001. 76(1-3): p. 8-12.
55. Hoa, X.D., A.G. Kirk, and M. Tabrizian, *Towards integrated and sensitive surface plasmon resonance biosensors: a review of recent progress*. Biosensors and Bioelectronics, 2007. 23(2): p. 151-160.
56. Voros, J., et al., *Optical grating coupler biosensors*. Biomaterials, 2002. 23(17): p. 3699-3710.
57. Horvath, R., et al., *Optical waveguide sensor for on-line monitoring of bacteria*. Optics letters, 2003. 28(14): p. 1233-1235.
58. Fang, Y., et al., *Resonant waveguide grating biosensor for living cell sensing*. Biophysical journal, 2006. 91(5): p. 1925-1940.
59. Yalcin, A., et al., *Optical sensing of biomolecules using microring resonators*. Selected Topics in Quantum Electronics, IEEE Journal of, 2006. 12(1): p. 148-155.
60. Vollmer, F. and S. Arnold, *Whispering-gallery-mode biosensing: label-free detection down to single molecules*. Nature Methods, 2008. 5(7): p. 591-596.
61. Carlborg, C.F., et al., *A packaged optical slot-waveguide ring resonator sensor array for multiplex label-free assays in labs-on-chips*. Lab Chip, 2010. 10(3): p. 281-290.
62. Chow, E., et al., *Ultracompact biochemical sensor built with two-dimensional photonic crystal microcavity*. Optics letters, 2004. 29(10): p. 1093-1095.
63. Choi, C.J. and B.T. Cunningham, *Single-step fabrication and characterization of photonic crystal biosensors with polymer microfluidic channels*. Lab Chip, 2006. 6(10): p. 1373-1380.
64. Choi, C.J. and B.T. Cunningham, *A 96-well microplate incorporating a replica molded microfluidic network integrated with photonic crystal biosensors for high throughput kinetic biomolecular interaction analysis*. Lab Chip, 2007. 7(5): p. 550-556.

65. Scullion, M.G., A. Di Falco, and T.F. Krauss, *Slotted photonic crystal cavities with integrated microfluidics for biosensing applications*. Biosensors and Bioelectronics, 2011. 27(1): p. 101-105.
66. Thrush, E., et al. *Integrated semiconductor fluorescent detection system for biochip and biomedical applications*. Microtechnologies in Medicine & Biology, 2nd Annual International IEEE-EMB Special Topic Conference, 2002: p.374-379.
67. Namasivayam, V., et al., *Advances in on-chip photodetection for applications in miniaturized genetic analysis systems*. Journal of Micromechanics and Microengineering, 2004. 14: p. 81-90.
68. Chabinyk, M.L., et al., *An integrated fluorescence detection system in poly (dimethylsiloxane) for microfluidic applications*. Analytical Chemistry, 2001. 73(18): p. 4491-4498.
69. Chediak, J.A., et al., *Heterogeneous integration of CdS filters with GaN LEDs for fluorescence detection microsystems*. Sensors and Actuators A: Physical, 2004. 111(1): p. 1-7.
70. Iordanov, V.P., et al., *Filter-protected photodiodes for high-throughput enzymatic analysis*. Sensors Journal, IEEE, 2004. 4(5): p. 584-588.
71. Hofmann, O., et al., *Monolithically integrated dye-doped PDMS long-pass filters for disposable on-chip fluorescence detection*. Lab Chip, 2006. 6(8): p. 981-987.
72. Lammel, G. and P. Renaud, *Free-standing, mobile 3D porous silicon microstructures*. Sensors and Actuators A: Physical, 2000. 85(1-3): p. 356-360.
73. Lorenzo, E., et al., *Porous silicon-based rugate filters*. Applied optics, 2005. 44(26): p. 5415-5421.
74. Ilyas, S., et al., *Porous silicon based narrow line-width rugate filters*. Optical Materials, 2007. 29(6): p. 619-622.
75. Jane, A., et al., *Porous silicon biosensors on the advance*. Trends in biotechnology, 2009. 27(4): p. 230-239.
76. Shen, L., et al., *A CMOS optical detection system for point-of-use luminescent oxygen sensing*. Sensors and actuators B: Chemical, 2011. 155(1): p. 430-435.
77. O'Sullivan, T., et al., *Implantable semiconductor biosensor for continuous in vivo sensing of far-red fluorescent molecules*. Opt Express, 2010. 18(12): p. 12513-12525.
78. Kwa, T.A. and R.F. Wolffenbittel, *Integrated grating/detector array fabricated in silicon using micromachining techniques*. Sensors and Actuators A: Physical, 1992. 31(1): p. 259-266.
79. Kong, S.H., D.D.L. Wijngaards, and R.F. Wolffenbittel, *Infrared micro-spectrometer based on a diffraction grating*. Sensors and Actuators A: Physical, 2001. 92(1-3): p. 88-95.

80. Raley, N.F., et al. *A Fabry-Perot microinterferometer for visible wavelengths*. Solid-State Sensor and Actuator Workshop, 1992, IEEE: p.170-173.
81. Correia, J.H., M. Bartek, and R.F. Wolffenbuttel, *Bulk-micromachined tunable Fabry-Perot microinterferometer for the visible spectral range*. Sensors and Actuators A: Physical, 1999. 76(1-3): p. 191-196.
82. Manzardo, O., et al., *Miniaturized time-scanning Fourier transform spectrometer based on silicon technology*. Optics letters, 1999. 24(23): p. 1705-1707.
83. Kraft, M., et al. *MEMS-based compact FT-spectrometers-a platform for spectroscopic mid-infrared sensors*. in Sensors, 2008 IEEE: p.130-133.
84. Jovanov, V., J. Ivanchev, and D. Knipp, *Standing wave Spectrometer*. Optics Express, 2010. 18(2): p. 426-438.
85. Russin, T., et al. *Development of a MEMS-based Raman spectrometer*. in *IEEE SENSORS 2010 Conference*. 2010: p.56-60.
86. Delage, A., et al. *Recent developments in integrated spectrometers*. 2004: IEEE.
87. Wolffenbuttel, R.F., *State-of-the-art in integrated optical microspectrometers*. Instrumentation and Measurement, IEEE Transactions on, 2004. 53(1): p. 197-202.
88. Wolffenbuttel, R.F., *MEMS-based optical mini-and microspectrometers for the visible and infrared spectral range*. Journal of Micromechanics and Microengineering, 2005. 15: p. S145-152.
89. Bland-Hawthorn, J. and A. Horton, *Instruments without optics: an integrated photonic spectrograph*. Arxiv preprint astro-ph/0606290, 2006.
90. Savage, N., *Spectrometers*. Nature Photonics, 2009. 3(10): p. 601-602.
91. Schuler, L.P., et al., *MEMS-based microspectrometer technologies for NIR and MIR wavelengths*. Journal of Physics D: Applied Physics, 2009. 42: p. 133001.
92. Xia, Z., et al. *Demonstration of high resolution SOI spectrometer with miniaturized disks*. in *Group IV Photonics (GFP), 2010 7th IEEE International Conference on*. 2010: p.252-254.
93. Xia, Z., et al., *High resolution on-chip spectroscopy based on miniaturized microdonut resonators*. Optics Express, 2011. 19(13): p. 12356-12364.
94. Momeni, B., E.S. Hosseini, and A. Adibi, *Planar photonic crystal microspectrometers in silicon-nitride for the visible range*. Optics Express, 2009. 17(19): p. 17060-17069.
95. Momeni, B., et al., *Integrated photonic crystal spectrometers for sensing applications*. Optics communications, 2009. 282(15): p. 3168-3171.
96. Momeni, B., et al., *An on-chip silicon grating spectrometer using a photonic crystal reflector*. Journal of Optics, 2010. 12: p. 035501.

97. Pervez, N.K., et al., *Photonic crystal spectrometer*. Arxiv preprint arXiv:1001.0580, 2010.
98. Babin, S., et al., *Digital optical spectrometer-on-chip*. Applied Physics Letters, 2009. 95: p. 041105-1-041105-3.
99. Babin, S., et al., *Fabrication of novel digital optical spectrometer on chip*. Journal of Vacuum Science & Technology B: Microelectronics and Nanometer Structures, 2009. 27(6): p. 3187-3191.
100. Peroz, C., et al., *Digital spectrometer-on-chip fabricated by step and repeat nanoimprint lithography on pre-spin coated films*. Microelectronic engineering, 2011. 88(8): p. 2092-2095.
101. Peroz, C., et al., *High-resolution spectrometer-on-chip based on digital planar holography*. Photonics Journal, IEEE, 2011. 3(5): p. 888-896.
102. Lammel, G., S. Schweizer, and P. Renaud, *Microspectrometer based on a tunable optical filter of porous silicon*. Sensors and Actuators A: Physical, 2001. 92(1): p. 52-59.
103. Goldman, D.S., P.L. White, and N.C. Anheier, *Miniaturized spectrometer employing planar waveguides and grating couplers for chemical analysis*. Applied optics, 1990. 29(31): p. 4583-4589.
104. Mohr, J., B. Anderer, and W. Ehrfeld, *Fabrication of a planar grating spectrograph by deep-etch lithography with synchrotron radiation*. Sensors and Actuators A: Physical, 1991. 27(1-3): p. 571-575.
105. Sander, D. and J. Muller, *Selffocussing phase transmission grating for an integrated optical microspectrometer*. Sensors and Actuators A: Physical, 2001. 88(1): p. 1-9.
106. Smit, M.K., *New focusing and dispersive planar component based on an optical phased array*. Electronics Letters, 1988. 24(7): p. 385-386.
107. Okamoto, K. *Tutorial: Fundamentals, technology and applications of AWGs*. 24th European Conference on Optical Communication, 1998. 2: p.7-47.
108. Manz, A., et al., *Design of an open-tubular column liquid chromatograph using silicon chip technology*. Sensors and actuators B: Chemical, 1990. 1(1-6): p. 249-255.
109. Auroux, P.A., et al., *Micro total analysis systems. 2. Analytical standard operations and applications*. ANALYTICAL CHEMISTRY-WASHINGTON DC-, 2002. 74(12): p. 2637-2652.
110. Reyes, D.R., et al., *Micro total analysis systems. 1. Introduction, theory, and technology*. ANALYTICAL CHEMISTRY-WASHINGTON DC-, 2002. 74(12): p. 2623-2636.
111. van den Berg, A. and T. Lammerink, *Micro total analysis systems: microfluidic aspects, integration concept and applications*. Microsystem technology in chemistry and life science, 1998: p. 21-49.

112. Vilkner, T., D. Janasek, and A. Manz, *Micro total analysis systems. Recent developments*. Analytical Chemistry, 2004. 76(12): p. 3373-3385.
113. Dittrich, P.S., K. Tachikawa, and A. Manz, *Micro total analysis systems. Latest advancements and trends*. Analytical Chemistry, 2006. 78(12): p. 3887-1908.
114. Zhang, J., et al., *Creating new fluorescent probes for cell biology*. Nature Reviews Molecular Cell Biology, 2002. 3(12): p. 906-918.
115. Shaner, N.C., P.A. Steinbach, and R.Y. Tsien, *A guide to choosing fluorescent proteins*. Nature Methods, 2005. 2(12): p. 905-909.
116. Shaner, N.C., G.H. Patterson, and M.W. Davidson, *Advances in fluorescent protein technology*. Journal of cell science, 2007. 120(24): p. 4247-4260.
117. Weiss, S., *Fluorescence spectroscopy of single biomolecules*. Science, 1999. 283(5408): p. 1676-1683.
118. Jablonski, A., *Über den mechanismus der Photolumineszenz von Farbstoffphosphoren*. Zeitschrift für Physik A Hadrons and Nuclei, 1935. 94(1): p. 38-46.
119. Resch-Genger, U., et al., *Quantum dots versus organic dyes as fluorescent labels*. Nature Methods, 2008. 5(9): p. 763-775.
120. Lopez, M.F., et al., *High-content proteomics: Fluorescence multiplexing using an integrated, high-sensitivity, multiwavelength charge-coupled device imaging system*. Proteomics, 2003. 3(7): p. 1109-1116.
121. Sapsford, K.E., L. Berti, and I.L. Medintz, *Materials for fluorescence resonance energy transfer analysis: beyond traditional donor-acceptor combinations*. Angewandte Chemie International Edition, 2006. 45(28): p. 4562-4589.
122. Roy, R., S. Hohng, and T. Ha, *A practical guide to single-molecule FRET*. Nature Methods, 2008. 5(6): p. 507-516.
123. Hohng, S., C. Joo, and T. Ha, *Single-molecule three-color FRET*. Biophysical journal, 2004. 87(2): p. 1328-1337.
124. Clamme, J.P. and A.A. Deniz, *Three-color Single-Molecule Fluorescence Resonance Energy Transfer*. ChemPhysChem, 2005. 6(1): p. 74-77.
125. Lewis, E.K., et al., *Color-blind fluorescence detection for four-color DNA sequencing*. Proceedings of the National Academy of Sciences of the United States of America, 2005. 102(15): p. 5346-5351.
126. Mishra, A., et al., *Cyanines during the 1990s: a review*. Chemical Reviews-Columbus, 2000. 100(6): p. 1973-2012.
127. Panigrahi, M., et al., *Syntheses of cyanines: a review*. Tetrahedron, 2012. 68(3): p. 781-805.

128. Karp, N.A. and K.S. Lilley, *Maximising sensitivity for detecting changes in protein expression: experimental design using minimal CyDyes*. *Proteomics*, 2005. 5(12): p. 3105-3115.
129. Anaya, C., N. Church, and J.P. Lewis, *Detection and identification of bacterial cell surface proteins by fluorescent labeling*. *Proteomics*, 2007. 7(2): p. 215-219.
130. Armitage, B.A., *Cyanine dye-DNA interactions: intercalation, groove binding, and aggregation*. *DNA Binders and Related Subjects*, 2005. 253: p. 55-76.
131. Armitage, B., *Cyanine Dye-Nucleic Acid Interactions*. *Heterocyclic Polymethine Dyes*, 2008. 14: p. 11-29.
132. Fegan, A., P.S. Shirude, and S. Balasubramanian, *Rigid cyanine dye nucleic acid labels*. *Chemical Communications*, 2008(17): p. 2004-2006.
133. Carreon, J.R., et al., *Cyanine dye conjugates as probes for live cell imaging*. *Bioorganic & medicinal chemistry letters*, 2007. 17(18): p. 5182-5185.
134. Toutchkine, A., D.V. Nguyen, and K.M. Hahn, *Simple one-pot preparation of water-soluble, cysteine-reactive cyanine and merocyanine dyes for biological imaging*. *Bioconjugate chemistry*, 2007. 18(4): p. 1344-1348.
135. Ernst, L.A., et al., *Cyanine dye labeling reagents for sulfhydryl groups*. *Cytometry*, 1989. 10(1): p. 3-10.
136. Mujumdar, R.B., et al., *Cyanine dye labeling reagents containing isothiocyanate groups*. *Cytometry*, 1989. 10(1): p. 11-19.
137. Wilson, W.D., et al., *Mechanism of intercalation: ion effects on the equilibrium and kinetic constants for the interaction of propidium and ethidium with DNA*. *Biopolymers*, 1985. 24(10): p. 1941-1961.
138. Nicoletti, I., et al., *A rapid and simple method for measuring thymocyte apoptosis by propidium iodide staining and flow cytometry*. *Journal of immunological methods*, 1991. 139(2): p. 271-279.
139. Streckowski, L. and B. Wilson, *Noncovalent interactions with DNA: an overview*. *Mutation Research/Fundamental and Molecular Mechanisms of Mutagenesis*, 2007. 623(1-2): p. 3-13.
140. Alivisatos, A.P., *Semiconductor clusters, nanocrystals, and quantum dots*. *Science*, 1996. 271(5251): p. 933-937.
141. Chan, W.C.W., et al., *Luminescent quantum dots for multiplexed biological detection and imaging*. *Current Opinion in Biotechnology*, 2002. 13(1): p. 40-46.
142. Bruchez Jr, M., et al., *Semiconductor nanocrystals as fluorescent biological labels*. *Science*, 1998. 281(5385): p. 2013-2016.
143. Chan, W.C.W. and S. Nie, *Quantum dot bioconjugates for ultrasensitive nonisotopic detection*. *Science*, 1998. 281(5385): p. 2016-2018.

144. Germain, M.E. and M.J. Knapp, *Optical explosives detection: from color changes to fluorescence turn-on*. Chem. Soc. Rev., 2009. 38(9): p. 2543-2555.
145. Lodeiro, C., et al., *Light and colour as analytical detection tools: A journey into the periodic table using polyamines to bio-inspired systems as chemosensors*. Chem. Soc. Rev., 2010. 39(8): p. 2948-2976.
146. Gruden, C., S. Skerlos, and P. Adriaens, *Flow cytometry for microbial sensing in environmental sustainability applications: current status and future prospects*. FEMS microbiology ecology, 2004. 49(1): p. 37-49.
147. Hoffman, R.A., *Flow Cytometry: Instrumentation, applications, future trends and limitations*. Standardization and Quality Assurance in Fluorescence Measurements II, 2008: p. 307-342.
148. Picot, J., et al., *Flow cytometry: retrospective, fundamentals and recent instrumentation*. Cytotechnology, 2012. 64(2): p. 109-130.
149. Van Dilla, M.A., et al., *Cell microfluorometry: a method for rapid fluorescence measurement*. Science, 1969. 163(3872): p. 1213-1214.
150. Hulett, H.R., et al., *Cell sorting: automated separation of mammalian cells as a function of intracellular fluorescence*. Science, 1969. 166(3906): p. 747-749.
151. Bonner, W.A., et al., *Fluorescence activated cell sorting*. Review of Scientific Instruments, 1972. 43(3): p. 404-409.
152. Ateya, D.A., et al., *The good, the bad, and the tiny: a review of microflow cytometry*. Analytical and bioanalytical chemistry, 2008. 391(5): p. 1485-1498.
153. Godin, J., et al., *Microfluidics and photonics for Bio-System-on-a-Chip: A review of advancements in technology towards a microfluidic flow cytometry chip*. Journal of biophotonics, 2008. 1(5): p. 355-376.
154. Chung, T.D. and H.C. Kim, *Recent advances in miniaturized microfluidic flow cytometry for clinical use*. Electrophoresis, 2007. 28(24): p. 4511-4520.
155. Fu, A.Y., et al., *A microfabricated fluorescence-activated cell sorter*. Nature biotechnology, 1999. 17(11): p. 1109-1111.
156. Simonnet, C. and A. Groisman, *High-throughput and high-resolution flow cytometry in molded microfluidic devices*. Analytical Chemistry, 2006. 78(16): p. 5653-5663.
157. Tung, Y.C., et al., *PDMS-based opto-fluidic micro flow cytometer with two-color, multi-angle fluorescence detection capability using PIN photodiodes*. Sensors and actuators B: Chemical, 2004. 98(2): p. 356-367.
158. Wolff, A., et al., *Integrating advanced functionality in a microfabricated high-throughput fluorescent-activated cell sorter*. Lab Chip, 2003. 3(1): p. 22-27.
159. Wang, Z., et al., *Measurements of scattered light on a microchip flow cytometer with integrated polymer based optical elements*. Lab Chip, 2004. 4(4): p. 372-377.

160. Roederer, M., et al., *8 color, 10-parameter flow cytometry to elucidate complex leukocyte heterogeneity*. Cytometry, 1997. 29(4): p. 328-339.
161. De Rosa, S.C., J.M. Brenchley, and M. Roederer, *Beyond six colors: a new era in flow cytometry*. Nature medicine, 2003. 9(1): p. 112-117.
162. Perfetto, S.P., P.K. Chattopadhyay, and M. Roederer, *Seventeen-colour flow cytometry: unravelling the immune system*. Nature Reviews Immunology, 2004. 4(8): p. 648-655.
163. Waggoner, A.S., *Fluorescent probes for cytometry*. Flow cytometry and sorting, 1990: p. 209-225.
164. Chattopadhyay, P.K., et al., *Quantum dot semiconductor nanocrystals for immunophenotyping by polychromatic flow cytometry*. Nature medicine, 2006. 12(8): p. 972-977.
165. Chattopadhyay, P.K., et al., *The use of quantum dot nanocrystals in multicolor flow cytometry*. Wiley Interdisciplinary Reviews: Nanomedicine and Nanobiotechnology, 2010. 2(4): p. 334-348.
166. Goddard, G., et al., *Single particle high resolution spectral analysis flow cytometry*. Cytometry Part A, 2006. 69(8): p. 842-851.
167. Watson, D.A., et al., *Spectral measurements of large particles by flow cytometry*. Cytometry Part A, 2009. 75(5): p. 460-464.
168. Duggan, M.P., T. McCreedy, and J.W. Aylott, *A non-invasive analysis method for on-chip spectrophotometric detection using liquid-core waveguiding within a 3D architecture*. Analyst, 2003. 128(11): p. 1336-1340.
169. Jindal, R. and S.M. Cramer, *On-chip electrochromatography using sol-gel immobilized stationary phase with UV absorbance detection*. Journal of Chromatography A, 2004. 1044(1): p. 277-285.
170. Minas, G., R.F. Wolffenbittel, and J.H. Correia, *A lab-on-a-chip for spectrophotometric analysis of biological fluids*. Lab Chip, 2005. 5(11): p. 1303-1309.
171. Minas, G., R.F. Wolffenbittel, and J.H. Correia, *An array of highly selective Fabry-Perot optical channels for biological fluid analysis by optical absorption using a white light source for illumination*. Journal of Optics A: pure and applied optics, 2006. 8: p. 272-278.
172. Kodate, K. and Y. Komai, *Compact spectroscopic sensor using an arrayed waveguide grating*. Journal of Optics a-Pure and Applied Optics, 2008. 10(4).
173. Vellekoop, A.R. and M.K. Smit, *Low-loss planar optical polarisation splitter with small dimensions*. Electronics Letters, 1989. 25(15): p. 946-947.
174. Smit, M.K. *Progress in AWG design and technology*. Proceedings of IEEE/LEOS workshop, 2005: p.26-31.

175. Hale, G.M. and M.R. Querry, *Optical constants of water in the 200-nm to 200-um wavelength region*. Applied Optics, 1973. 12(3): p. 555-563.
176. Jalali, B., et al., *Advances in silicon-on-insulator optoelectronics*. IEEE Journal of Selected Topics in Quantum Electronics, 1998. 4(6): p. 938-947.
177. Fukazawa, T., F. Ohno, and T. Baba, *Very compact arrayed-waveguide-grating demultiplexer using Si photonic wire waveguides*. Jpn. J. Appl. Phys, 2004. 43(5B): p. 673-675.
178. Przyrembel, G., et al., *Design and fabrication of arrayed waveguide grating multiplexers on silicon-on-insulator platforms*. Optical Engineering, 2007. 46: p. 094602.
179. Zirngibl, M., C. Dragone, and C. Joyner, *Demonstration of a 15 x 15 arrayed waveguide multiplexer on InP*. IEEE Photonics Technology Letters, 1992. 4(11): p. 1250-1253.
180. Kohtoku, M., et al., *InP-based 64-channel arrayed waveguide grating with 50 GHz channelspacing and up to-20 dB crosstalk*. Electronics Letters, 1997. 33(21): p. 1786-1787.
181. Yoshikuni, Y., *Semiconductor arrayed waveguide gratings for photonic integrated devices*. IEEE Journal of Selected Topics in Quantum Electronics, 2002. 8(6): p. 1102-1114.
182. Kawachi, M., *Silica waveguides on silicon and their application to integrated-optic components*. Optical and Quantum Electronics, 1990. 22(5): p. 391-416.
183. Himeno, A., K. Kato, and T. Miya, *Silica-based planar lightwave circuits*. IEEE Journal of Selected Topics in Quantum Electronics, 1998. 4(6): p. 913-924.
184. Kaneko, A., et al., *Design and applications of silica-based planar lightwave circuits*. IEEE Journal of Selected Topics in Quantum Electronics, 1999. 5(5): p. 1227-1236.
185. Schauwecker, B., et al., *Optical waveguide components with high refractive index difference in silicon-oxynitride for application in integrated optoelectronics*. Optical Engineering, 2002. 41: p. 237.
186. Lee, M., et al., *Polymer-based devices for optical communications*. ETRI journal, 2002. 24(4): p. 259-269.
187. Becker, H. and L.E. Locascio, *Polymer microfluidic devices*. Talanta, 2002. 56(2): p. 267-287.
188. Shadpour, H., et al., *Physiochemical properties of various polymer substrates and their effects on microchip electrophoresis performance*. Journal of Chromatography A, 2006. 1111(2): p. 238-251.
189. Bass, M., et al., *Handbook of optics. Vol. 2, Devices, measurements, and properties*. 1995: McGraw-Hill New York, USA.

190. Waynant, R. and M. Ediger, *Electro-Optics Handbook*. 2000: McGraw-Hill Professional.
191. Worhoff, K., P. Lambeck, and A. Driessen, *Design, tolerance analysis, and fabrication of silicon oxynitride based planar optical waveguides for communication devices*. Journal of Lightwave Technology, 1999. 17(8): p. 1401-1407.
192. Wörhoff, K., et al., *Plasma enhanced chemical vapor deposition silicon oxynitride optimized for application in integrated optics*. Sensors & Actuators: A. Physical, 1999. 74(1-3): p. 9-12.
193. Woerhoff, K., et al. *Optimization of LPCVD Silicon Oxynitride growth to large refractive index homogeneity and layer thickness uniformity*. Proceedings of SPIE. 1997. 3099: p. 257.
194. Schauwecker, B., et al., *Small-size silicon-oxynitride AWG demultiplexer operating around 725 nm*. IEEE Photonics Technology Letters, 2000. 12(12): p. 1645-1646.
195. Hyde, J.F., *US Patent number 2,272,342*. 1942, Google Patents.
196. Przyrembel, G. and B. Kuhlów, *Design of Silica Based AWG for Visible Light (= 670 nm) Applications*. 10th Micro-optics Conference. MOC, 2004. 4: p. 23-25.
197. Komai, Y., et al. *Spectroscopic sensing using a visible arrayed-waveguide grating*. Proceedings of SPIE. 2005. 5867: 58670D1-12.
198. Rowland, H.A., *LXI. Preliminary notice of the results accomplished in the manufacture and theory of gratings for optical purposes*. Philosophical Magazine Series 5, 1882. 13(84): p. 469-474.
199. Palmer, C.A. and E.G. Loewen, *Diffraction grating handbook*. 2005: Newport Corporation.
200. Van Zyl, H.G., *Modelling of integrated optic components for lightwave communications systems using the beam propagation method*. Thesis. University of Johannesburg, 2009.
201. Holzwarth, C., T. Barwicz, and H. Smith, *Optimization of hydrogen silsesquioxane for photonic applications*. Journal of Vacuum Science & Technology B: Microelectronics and Nanometer Structures, 2007. 25: p. 2658-2661.
202. Xia, Y. and G.M. Whitesides, *Soft lithography*. Annual review of materials science, 1998. 28(1): p. 153-184.
203. Bhattacharya, S., et al., *Studies on surface wettability of poly (dimethyl) siloxane (PDMS) and glass under oxygen-plasma treatment and correlation with bond strength*. Microelectromechanical Systems, Journal of, 2005. 14(3): p. 590-597.
204. Bogaerts, W., et al., *Fabrication of photonic crystals in silicon-on-insulator using 248-nm deep UV lithography*. Selected Topics in Quantum Electronics, IEEE Journal of, 2002. 8(4): p. 928-934.

205. Settle, M., et al., *Low loss silicon on insulator photonic crystal waveguides made by 193nm optical lithography*. Opt. Express, 2006. 14(6): p. 2440-2445.
206. Hatzakis, M., B.J. Canavello, and J.M. Shaw, *Single-step optical lift-off process*. IBM Journal of Research and Development, 1980. 24(4): p. 452-460.
207. Halverson, R.M., M.W. MacIntyre, and W.T. Motsiff, *The mechanism of single-step liftoff with chlorobenzene in a diazo-type resist*. IBM Journal of Research and Development, 1982. 26(5): p. 590-595.
208. Redd, R., et al. *Lithographic process for high-resolution metal lift-off*. Proceedings of SPIE. 1999. 3678: p.1341-1351.
209. Lorenz, H., et al., *SU-8: a low-cost negative resist for MEMS*. Journal of Micromechanics and Microengineering, 1997. 7: p. 121.
210. Glezos, N., et al., *Aqueous base development and acid diffusion length optimization in negative epoxy resist for electron beam lithography*. Journal of Vacuum Science & Technology B: Microelectronics and Nanometer Structures, 2000. 18: p. 3431.
211. Aktary, M., et al., *High-resolution pattern generation using the epoxy novolak SU-8 2000 resist by electron beam lithography*. Journal of Vacuum Science & Technology B: Microelectronics and Nanometer Structures, 2003. 21: p. L5.
212. Macintyre, D. and S. Thoms, *High resolution electron beam lithography studies on Shipley chemically amplified DUV resists*. Microelectronic engineering, 1997. 35(1): p. 213-216.
213. McLaughlin, A.J., *Hybrid Silicon Optoelectronic Technologies*. PhD thesis, University of Glasgow. 1998.
214. Williams, K.R. and R.S. Muller, *Etch rates for micromachining processing*. Microelectromechanical Systems, Journal of, 1996. 5(4): p. 256-269.
215. Mathieson, K., et al., *Fabricating high-density microarrays for retinal recording*. Microelectronic engineering, 2003. 67: p. 520-527.
216. Ruano, J.M., et al., *Fabrication of integrated microanalytical chambers and channels for biological assays using flame hydrolysis deposition glass*. Microelectronic engineering, 1999. 46(1): p. 419-422.
217. Li, W.T., D.A.P. Bulla, and R. Boswell, *Surface oxidation of Al masks for deep dry-etch of silica optical waveguides*. Surface and Coatings Technology, 2007. 201(9-11): p. 4979-4983.
218. Williams, K.R., K. Gupta, and M. Wasilik, *Etch rates for micromachining processing - Part II*. Journal of Microelectromechanical Systems, 2003. 12(6): p. 761-778.
219. Bhardwaj, J.K., et al. *ADVANCES IN DEEP OXIDE ETCH PROCESSING FOR MEMS-MASK SELECTION*. 2000: World Scientific Pub Co Inc.
220. Siew, Y.K., et al., *Thermal curing of hydrogen silsesquioxane*. Journal of the Electrochemical Society, 2000. 147: p. 335.

221. Whitesides, G.M., *The origins and the future of microfluidics*. Nature, 2006. 442(7101): p. 368-373.
222. Abgrall, P. and A.M. Gue, *Lab-on-chip technologies: making a microfluidic network and coupling it into a complete microsystem-a review*. Journal of Micromechanics and Microengineering, 2007. 17: p. R15.
223. Haeberle, S. and R. Zengerle, *Microfluidic platforms for lab-on-a-chip applications*. Lab Chip, 2007. 7(9): p. 1094-1110.
224. Mark, D., et al., *Microfluidic lab-on-a-chip platforms: requirements, characteristics and applications*. Chem. Soc. Rev., 2010. 39(3): p. 1153-1182.
225. Becker, H. and C. Gartner, *Polymer microfabrication technologies for microfluidic systems*. Analytical and bioanalytical chemistry, 2008. 390(1): p. 89-111.
226. Duffy, D.C., et al., *Rapid prototyping of microfluidic systems in poly (dimethylsiloxane)*. Analytical Chemistry, 1998. 70(23): p. 4974-4984.
227. McDonald, J.C., et al., *Fabrication of microfluidic systems in poly (dimethylsiloxane)*. Electrophoresis, 2000. 21(1): p. 27-40.
228. Sia, S.K. and G.M. Whitesides, *Microfluidic devices fabricated in poly (dimethylsiloxane) for biological studies*. Electrophoresis, 2003. 24(21): p. 3563-3576.
229. Whitesides, G.M., et al., *Soft lithography in biology and biochemistry*. Annual review of biomedical engineering, 2001. 3(1): p. 335-373.
230. Chang-Yen, D.A., R.K. Eich, and B.K. Gale, *A monolithic PDMS waveguide system fabricated using soft-lithography techniques*. Journal of lightwave technology, 2005. 23(6): p. 2088.
231. Kim, J.Y., et al., *Automatic aligning and bonding system of PDMS layer for the fabrication of 3D microfluidic channels*. Sensors and Actuators A: Physical, 2005. 119(2): p. 593-598.
232. Rauf, S., A. Glidle, and J.M. Cooper, *Application of quantum dot barcodes prepared using biological self-assembly to multiplexed immunoassays*. Chemical Communications, 2010. 46(16): p. 2814-2816.
233. Committee, A.M., *Recommendations for the definition, estimation and use of the detection limit*. The Analyst, 1987. 112(2): p. 199-204.
234. *Instructions of NHS and Sulfo-NHS*. www.thermoscientific.com/pierce.
235. *Instructions of EDC*. www.thermoscientific.com/pierce.
236. Li, Y.P., *Optical device having low insertion loss*. 1998, United States Patent.
237. Sugita, A., et al., *Very low insertion loss arrayed-waveguide grating with vertically tapered waveguides*. Photonics Technology Letters, IEEE, 2000. 12(9): p. 1180-1182.

238. So, D.W. and C.H. Yoo, *Vertical taper waveguide*. 2005, United States Patent.
239. Fong, J., et al., *Controlled selectivity etch for use with optical component fabrication*. 2006, United States Patent.
240. Dragone, C., et al., *Low-loss NxN wavelength router*. Electronics Letters, 2005. 41(13): p. 763-764.
241. Park, J., et al., *New design for low-loss star couplers and arrayed waveguide grating devices*. Photonics Technology Letters, IEEE, 2002. 14(5): p. 651-653.
242. Suzuki, K., et al., *Reduction in the diffraction loss of an arrayed-waveguide grating by use of an interference fringe between slab and arrayed waveguides*. Optics letters, 2005. 30(18): p. 2400-2402.
243. Chen, K.L. and D. Kerps, *Coupling efficiency of surface-emitting LED's to single-mode fibers*. Lightwave Technology, Journal of, 1987. 5(11): p. 1600-1604.
244. Ismail, N., et al., *Integrated approach to laser delivery and confocal signal detection*. Optics letters, 2010. 35(16): p. 2741-2743.
245. Ismail, N., et al., *Efficiency of integrated waveguide probes for the detection of light backscattered from weakly scattering media*. Applied optics, 2011. 50(6): p. 935-942.
246. Ismail, N., et al., *Excitation and light collection from highly scattering media with integrated waveguides*. Photonics Technology Letters, IEEE, 2011. 23(5): p. 278-280.
247. Leon-Saval, S.G., et al., *Multimode fiber devices with single-mode performance*. Optics letters, 2005. 30(19): p. 2545-2547.
248. Noordegraaf, D., et al., *Efficient multi-mode to single-mode coupling in a photonic lantern*. Optics Express, 2009. 17(3): p. 1988-1994.
249. Bland-Hawthorn, J., et al. *PIMMS: photonic integrated multimode microspectrograph*. Proceedings of SPIE 7735, 77350N, 2010.
250. Kee, J.S., et al., *Design and fabrication of Poly (dimethylsiloxane) arrayed waveguide grating*. Optics Express, 2010. 18(21): p. 21732-21742.
251. Ismail, N., et al., *Raman spectroscopy with an integrated arrayed-waveguide grating*. Optics letters, 2011. 36(23): p. 4629-4631.